UNIVERSITY OF NAPLES "FEDERICO II"

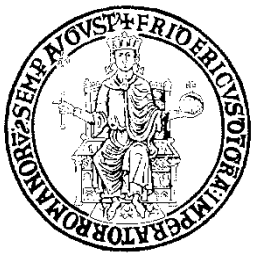

Ph.D THESIS IN ENGINEERING OF MATERIALS AND STRUCTURES

XXVIII CYCLE

"EFFECT OF PEPTIDE FUNCTIONALIZATION ON NANOPARTICLE TRANSPORT ACROSS BRAIN ENDOTHELIUM IN A MICROFLUIDIC CHIP"

Tutor:

Prof. Paolo A. Netti
Dr. Daniela Guarnieri

Candidate:

Andrea Patrizia Falanga

Coordinator:

Prof. Giuseppe Mensitieri

2013-2016

Table of Contents

ABSTRACT

Despite the effort of medicine, many potential drugs, during the development for clinical use, prove not to be able in achieving the central nervous system (CNS), due to the low permeability of the blood-brain barrier (BBB). In consequence, most CNS diseases are untreated. For that reason, there is an increasing interest towards nanotechnology applied to medicine in order to improve the treatments of brain diseases. An important field of nanotechnology applications to CNS is the development of nano-tools for drugs delivering, such as nanoparticles (NPs). In recent years, researchers have been working on several strategies to deliver drugs into the brain. They take advantage of the chance to modulate the chemical-physical surface properties of NPs, improving cell-NP interaction in order to adsorb, to carry compounds and to enhance drug delivery across the BBB. Nevertheless, current drug delivery systems are still associated with the low efficiency of targeting and crossing of the BBB. In this work, peptide functionalized NPs have been synthesized and characterized in order to target and cross the cerebral endothelium. The iron-mimicry moiety CRTIGPSVC (CRT) has been chosen as BBB targeting peptide, exploiting its ability to recognize the transferrin receptor overexpressed on the brain endothelium. Staquicini et al. reported the advanced specific transport ability of CRT through the BBB. Therefore in this work, biocompatible NPs made up of poly (D,L-lactic-co-glycolic acid) (PLGA)-block-polyethylene glycol (PEG) copolymer (namely PELGA) and functionalized with CRT has been synthesized and characterized. The behavior in targeting and transport ability of the NPs in mouse brain endothelial cells has been investigated, under flow conditions. In order to improve the translocation across the BBB, decreasing the lysosomal storage of CRT-NPs, gH625 peptide has been chosen as cell-penetrating peptide (CPP). gH625 is a membranotropic peptide, well known for its ability to penetrate cell membranes and transport a large variety of cargo molecules/materials inside the cells. We speculated that the conjugation of CRT and gH625 to nanoparticle, may improves its translocation efficiency across the BBB. To test this hypothesis, PELGA NPs functionalized with CRT targeting peptide and with the CPP gH625 has been designed. NP efficiency to target the BBB under static and flow conditions and to penetrate across the *in vitro* BBB has been evaluated. Results demonstrated the cooperative effect of NP functionalization with gH625

and CRT 1:2 in static and flow conditions with a relevant impact on NP transport across the cerebral endothelium.

In order to investigate the effect of functionalized NP on transport across the cerebral endothelium, a flow-based *in vitro* BBB on chip has been engineered. The system more closely mimics *in vivo* environment and represents a valid BBB *in vitro* model since exerts the barrier function. Therefore, a study platform for drug delivery systems has been developed. The BBB model system is able to investigate the effects of dynamic conditions on specific targeting and transport across the brain endothelium of active molecules conjugated to nanocarriers.

1 CHAPTER 1

1.1 INTRODUCTION

1.1.1 Nanomedicine: the application of Nanotechnology to cross biological barriers

Nanotechnology is the science which allows the study and possible applications of small materials from 1 to 100 nm. The basic concept is that materials behave in different and often useful ways at the nanoscale. Applications of these molecules are emerging in several scientific fields: chemistry, medicine, biology, physics, engineering [1]. Some of them are: advanced drug delivery systems, medical diagnostic tools, such as "lab-on-a-chip", real time diagnostics for physicians, cooling chips or wafers to replace compressors in cars, refrigerators, air conditioners and multiple other devices, utilizing no chemicals or moving parts, sensors for airborne chemicals or other toxins, photovoltaics (solar cells), fuel cells and portable power to provide inexpensive, clean energy, new high-performance materials; and much more [2]. Interest of most researchers is to exploit nanotechnology in the field of medicine, in particular diagnostic and therapeutic branches. Application of nanotechnology to medicine is also called ‘nanomedicine’ and appears to be a relatively recent trend. Basic nanotechnology approaches for medical application date back several decades [3]. The main goal of nanomedicine is to improve the diagnosis and treatment of medical conditions including aging and ultimately for the improvement and extension of natural human biological structure and function. For this purpose, nanomedicine employs innovative ways to develop new approaches and therapies for treatment of diseases, including drug delivery [4–8]. This approach consists in the administration of drugs associated with carriers. Drug is located in the cavity enclosed by the polymer membrane and is physically or uniformly dispersed in a polymer matrix capable to carry the drug in the target site and influence drug release by modulation of physical-chemical properties of the carriers. Other methods more innovative are based on nanoparticles (NPs), dendrimers, nanogel and nanoemulsions [9,10] (Fig. 1). In general the use of a soluble macromolecular carrier for drug delivery allows to modify the pharmacokinetic properties (absorption-distribution-metabolism). The carrier used in drug delivery is generally a system having order of magnitude of micro and nano-meter. The advantage of nanosystems, compared to microsystems, relies on the reduced

dimensions which allow the crossing of biological barriers, such as the blood-brain barrier (BBB).

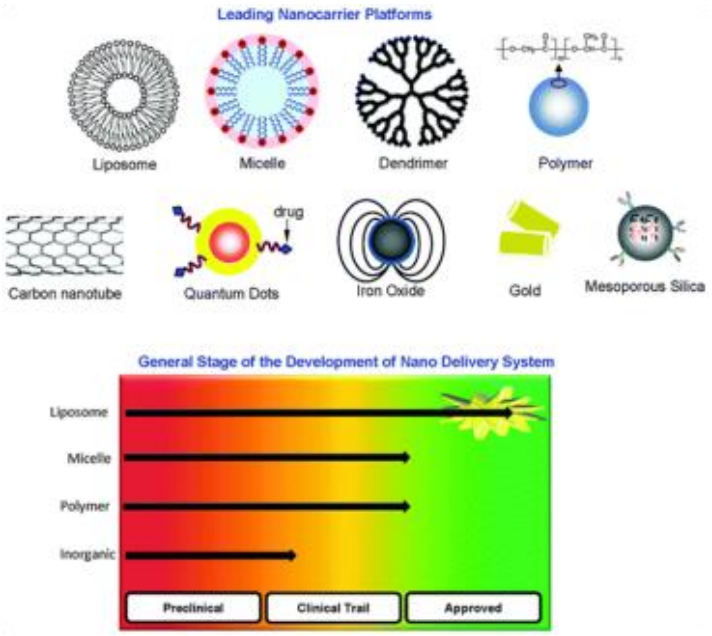

Wilson X. Mai et al. *Integr. Biol., 2013, 5, 19-28* The Royal Society of Chemistry 2013

Figure 1. Nanocarriers for drug delivery across the BBB.

1.1.2 Blood-Brain barrier

In most cases endothelial cells in systemic vessels do not express continuous tight junctions. In fact, fenestrations are present between adjacent cells, so that molecules can pass through tissues. In the BBB only small (< 500 Da) or lipophilic molecules can cross the barrier. BBB separates the circulating blood side from the brain side. It is formed by cerebrovascular endothelial cells, surrounded by basal lamina and astrocytic perivascular end-feet linking to the neurons (Fig. 3). The main role of BBB is to preserve brain homeostasis and to prevent toxic substances from entering the brain. An important feature of this barrier is the low and selective permeability to molecules, which is due to its peculiar biological characteristics. These characteristics include: the lack of fenestrations, low number of pinocytic vesicles, the presence of cell-cell junctions which are composed of smaller subunits, frequently biochemical dimers that are transmembrane proteins such as occludin, claudin, junctional adhesion molecule (JAM). Each of these transmembrane

proteins is anchored into the endothelial cells by another protein complex that includes ZO-1 and associated proteins occluding junction between cells of vascular walls, the presence of an high number of tight junctions between adjacent endothelial cells, formed by an intricate complex of transmembrane proteins with cytoplasmic accessory proteins. The barrier properties of the BBB are determined also by specific transport mechanisms [11]. Therefore, BBB structure reflects its function which severely regulates the transport of molecules to the brain. Nutrients exploit specialized transcellular mechanisms in order to enter into the CNS. Diffusion of substances into the brain can be divided into paracellular (between cells) and transcellular (across cells) diffusion, both of which are non-saturable and non-competitive. Paracellular diffusion does not occur to any great extent at the BBB, due to the tight junctions. In the case of transcellular diffusion, the higher is the lipophilicity of a substance the greater is the diffusion into the brain [12]. They are crucial for the regulation of permeability.

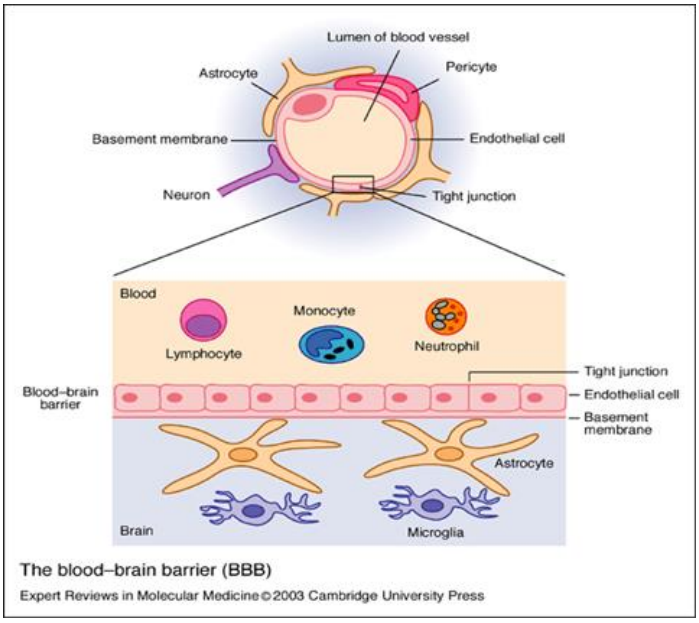

Figure 3: Schematic representation of the BBB.

1.1.3 Transport mechanisms through the BBB

The most simple way to cross the cell membrane is the passive diffusion. Non-polar solutes and lipid soluble, such as O_2 and CO_2, dissolve in the cell membrane and passively proceeds from high to low concentrations through the barrier, without any input of energy. This mechanism is called osmosis. Water-soluble substances such as penicillin are hampered in

getting through. Specific transporters, carrier-mediated efflux, can transport essential polar molecules, such as amino acids, glucose and nucleosides into the brain. Active efflux carriers can intercept some of passively penetrating solutes (for example lipid soluble drugs) and pump them out of the endothelial cells via efflux transporters such as P-glycoprotein. Carrier-mediated influx (passive or secondarily active) can transport essential polar molecules, such as amino acids, glucose, small peptides, into the CNS. Furthermore, TJ modulation may occur, which relaxes the junctions and entirely or partially opens the para-cellular aqueous diffusional pathway (polar solutes). Receptor-Mediated Transcytosis (RMT) can transport macromolecules: receptor on the apical plasma membrane recognizes and binds a RMT ligand (for example Insulin, Transferrin, Leptin, cytokines), peptide ligand mimetic or an anti-receptor antibody, with subsequent transcytosis across the BBB. Adsorptive-Mediated Transcytosis (AMT) is induced by non-specifically negatively charged molecules such as avidin, cationised albumin and it is also transported across BBB. RMT and AMT are time- and concentration-dependent processes, which require energy. They are independent from their gradient concentration (Fig. 4).

Transcytosis at the BBB starts with uptake either through clathrin-coated pits or caveolae, named endocytosis. These vesicles repel anionic molecules and require the interaction of a ligand with moieties expressed on the luminal side of endothelial cells. After interaction, endocytosis involves the invagination of the plasma membrane, in order to form vesicles able to transport molecules from outside to inside the cells. There are 2 kinds of cellular transcytosis: clathrin- and caveolin mediated. The first one allows the cells to introduce nutrients and regulatory molecules inside the cell. This mechanism requires a selective recognition of molecules from specific receptors which are express on the plasma membrane. This process is followed by the formation of the complex "Receptor-Ligand" in specific points of the membrane called clathrin-coated. Afterwards vesicles lose their clathrin coat and blend with an endosome. Apical (or basolateral) endosome transfers material to recycling- basolateral (or apical) endosome. This vesicle is shuttled to the (brain side) plasma membrane and exocytosis occurs, releasing the vesicle's content into the brain parenchyma. Alternatively, vesicle can also be sent to the lysosome for degradation of its content. Caveolae-coated vesicles, instead, are involved in the internalization of ligand and messengers. It is coated by caveolin which links cholesterol on the plasma membrane, introducing itself inside the cell. After caveolae formation and its detachment from the plasma membrane as endocytic vesicles, caveolae is transported through the intracellular space and fuses with the basal endothelial surface, releasing its content into the interstitial space. The new general strategies for delivering biologics into the brain employ the RMT

via. Such strategies involve the conjugation of a receptor-targeting moiety with the drug of interest.

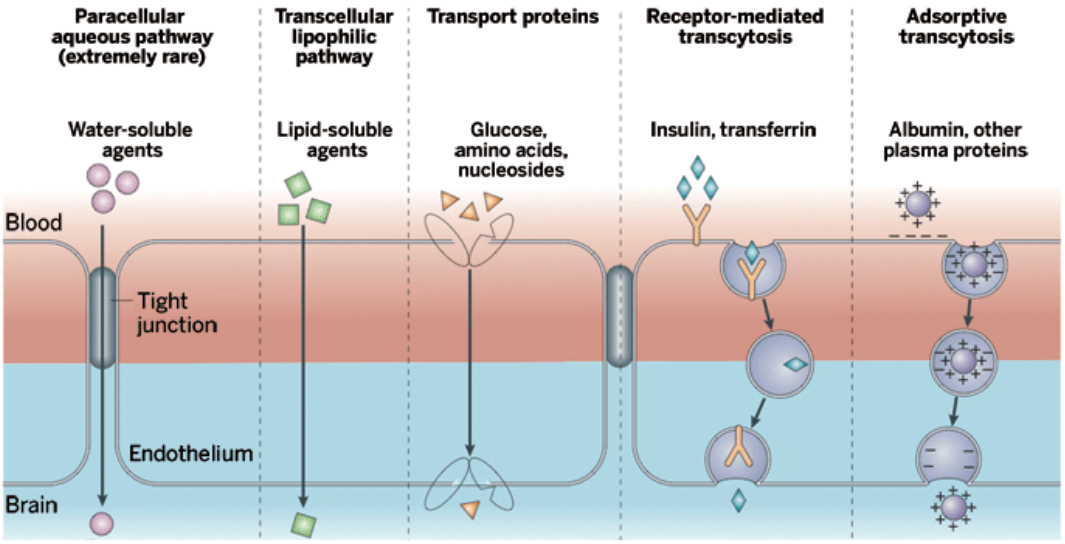

Nature Reviews Neuroscience © 2005 and *Elsevier* © 1996

Figure 4. Potential routes for transport across the BBB.

1.1.4 Strategies to overcome the BBB

Conventional drug therapies for CNS related pathology, such as brain tumors, HIV encephalopathy, epilepsy, cerebrovascular diseases and neurodegenerative disorders, involve the use of strategies as the temporary and local breakage of the endothelium, intracerebral injections, to administer the active drug directly into the brain or introduction of a slow-release implant into the brain [13]. Despite the efforts of medicine, the effectiveness of conventional drug treatments is limited. These treatments are often invasive, low effective for the patient and might cause several side effects: destroying the BBB temporarily leaves the brain vulnerable to infection and the insertion of solid implant can damage brain tissue. Therefore many potential drugs have failed and have been discarded during their development for clinical use due to the limitation in delivering them in sufficient quantity to the brain. Furthermore a lot of molecules which show promising therapeutic results *in vitro*, are larger than 500 Da and water soluble, so they are unable to enter brain tissue in significant amounts. Charged molecules and compounds that contain rotatable bonds have also a lower ability of penetration across the BBB [14]. In addition, lipid solubility improves the crossing of BBB but reduces its solubility. To achieve efficient

treatments of the CNS, it is necessary to transport drug across the BBB [15]. Nanomedicine applied to the treatment of the CNS diseases provides a valid alternative therapeutic approach to conventional treatments. The challenge to win is achievement of CNS, reaching the threshold of a sufficient drug concentration, in order for it to be effective, avoiding side effects to healthy tissues (Fig. 5).

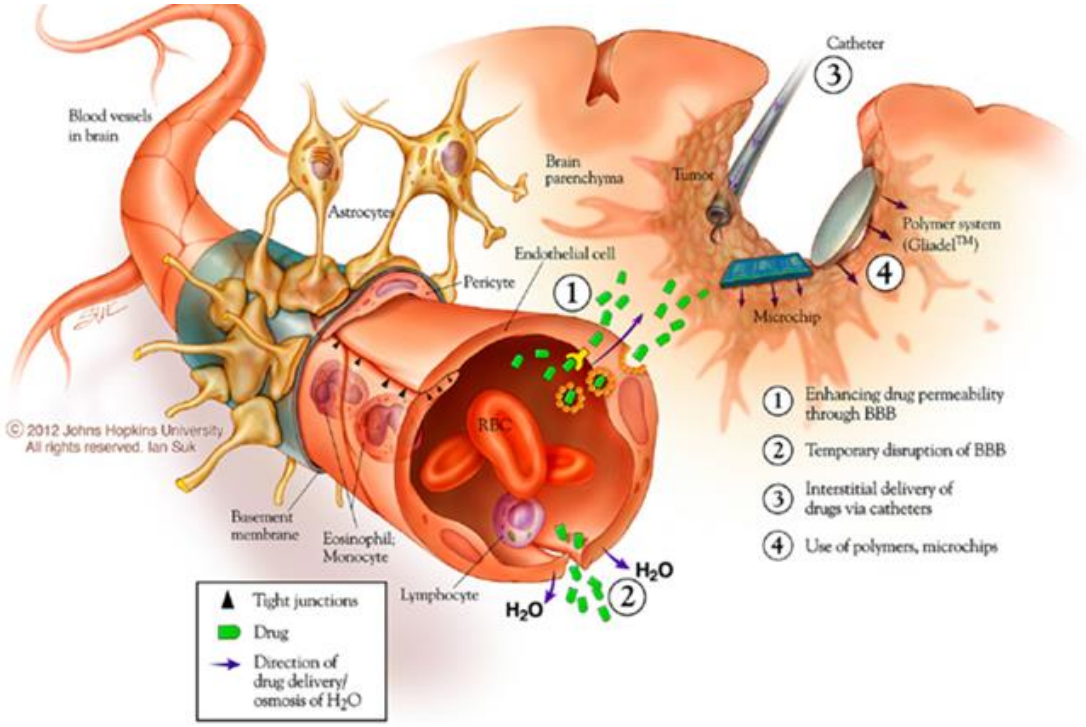

Figure 5: Targeted therapy across the blood-brain barrier.

1.1.5 Engineered-NPs for BBB crossing

A promising strategy to control the delivery of drugs to their action site is represented by the use of nanocarriers, such as nanoparticles (NPs), dendrimers, nanogel and nanoemulsions. The surface functionalization of nanocarriers, by using chemical or biological moieties, offers the possibility to recognize and cross the endothelium through the binding of specific receptors and exploiting the mechanism of transcytosis [16]**.** Among the various methods used by researchers, RMT is considered the most common strategy for the active transport and has been widely exploited for brain targeting [17,18]. The targeting moiety could be an endogenous RMT ligand, a peptide ligand mimetic, or an anti-receptor antibody. Upon intravenous administration, at least a portion of the RMT-targeted nanocarriers enters the brain by RMT. Many brain drug delivery strategies have focused on

RMT pathway for the delivery of many different biologics, following vesicular trafficking and avoiding endo-lysosomal storage. Brain capillary endothelial cells overexpress different receptors such as transferrin (Tf), insulin and low-density lipoprotein [19–26]. The transferrin receptor (TfR) was one of the first RMT systems studied for BBB drug delivery. In particular, TfR mediates iron delivery to the brain parenchyma via binding and intracellular trafficking of the iron-binding protein Tf [27]. Internalization of the Tf-TfR complex leads to the endosomal compartments in which the acidification (pH < 5.5) allows the release of iron from the ligand. Iron is transported into the cytoplasm for utilization or storage, whereas the apo-transferrin (apo-Tf) remains tightly bound to its receptor until it reaches the plasma membrane. Here, the apo-Tf rapidly dissociates from the receptor at neutral pH [28]. The free receptor, on the cell surface, is available for another cycle of RMT. The insulin receptor (IR) is responsible for the import of blood insulin into the brain via RMT. Use of insulin as an RMT-targeting vector has not been exploited, given both a short serum half-life of 10 min and the potential for exogenously administered insulin to cause hypoglycemia. The low density lipoprotein receptors, (LDLR) mediate the transport of lipoproteins and other ligands, such as ApoE, Apo B, Angiopep-2, across the BBB via RMT. Ligands, such as Tf, insulin and LDL, have high affinity for specific receptor but usually are not efficient to enhance endocytosis of NP. In fact, to date, only a few studies have clearly demonstrated the therapeutic effect of targeted nanocarriers in the treatment of cerebral diseases [29,30]. To further penetrate the brain endothelium, avoiding lysosomal accumulation of NPs, a possible strategy is the surface functionalization with bioactive peptides, such as cell penetrating peptides (CPPs). CPPs are short peptides of 5-40 amino-acids with net positive charge, helical moment, amphipatic nature. CPPs enter cells presumably by means of their cationic groups initially interacting with negative charged residues of cell membrane. Several studies demonstrate the effectiveness of CPPs such as TAT, in promoting NP transport across the BBB [31]. Great attention has been also directed towards CPP peptides, which take advantage of the non-toxic components of neurotoxins to overcome the BBB and reach the CNS. Neurotoxins as potential shuttles can be classified by origin: viral (for example *Herpes simplex virus, Rabies virus*), bacterial (*Vibrio Cholerae, Clostridium botulinum*) and animal (*Bungarus candidus snake, Ophiophagus Hannah*) [32]. As reported, NPs functionalized with gH625, a viral fusion peptide derived from the glycoprotein gH of Herpes simplex type 1 facilitated the delivery of NPs across the BBB, leading to significant higher cell uptake and crossing, bypassing the lysosomal entrapment [33]. Despite the lack of site specificity, non-toxic moiety of neurotoxins could act on all cell membranes, leading to peripheral and unwanted side effects. Therefore, in order

to overcome the BBB, avoiding unwanted side effects to healthy tissues, it's crucial to develop nanocarriers which are able to specific target and penetrate the BBB.

1.1.6 Experimental models to study the BBB

Understanding the BBB physiology is crucial to analyze its capabilities. Hereafter we describe the methods to investigate the effect of NP functionalization on the interaction with the BBB in order to improve therapeutic treatments to the CNS. Experimental systems available to study the BBB are: *in vivo, ex vivo, in vitro, in silico*.

***In vivo* studies**

The most consolidated method to study transport across the BBB is to perform *in vivo* experiments because it allows to study whole brain microenvironment and biological processes in live animals and the results are clearly more reliable. In vivo studies might be carried out to assess brain transport, metabolism, and BBB disruption. On the other hand main disadvantages are: ethical issues on the human brain, high costs and not allowing real-time studies. Besides *in vivo* studies of the BBB are very difficult and only can be performed in animal experiments, such as in mice, and remains the need to translate the results in humans [34].

***Ex vivo* studies**

Allowing experiment on living tissue in an artificial microenvironment outside the organism. The most used method for brain studies are slices. In slice, the cytoarchitecture of the tissue is maintained. Advantages of *ex vivo* studies are: controlled environment and provide the opportunity to study whole organs (impossible in living subjects). Disadvantages of this approach: post-mortem delay, allows short-term studies and the microenvironment is artificial [35]. Main ex vivo studies on brain are: tight junctions, evaluation of brain capillary permeability.

***In silico* studies**

In silico (computational) studies are performed by development of computational models using sophisticated algorithms. BBB *In silico* study tries to predict brain permeability to drugs and transporter properties. This approach is cheaper and is able to screen rapidly a large number of compounds and allows a reduction in the use of animals and reagents.

However, the major defect is that it does not consider other key factors such as the permeability, also appearing in the complex nature of BBB. Besides, conformation of molecules could provide false results [36].

***In vitro* studies**

A valid alternative is provided by using *in vitro* models which offers the advantage of mimicking what happens at the biological level, ensuring the opportunity to have a highly controlled environment and to eliminate a large number of *in vivo* physiological variables in brain [37]**.** They allow investigations that appear difficult to be performed *in vivo,* for example drug delivery to the CNS. *In vitro* model systems are able to reproduce the key physiological and biological characteristics of BBB *in vivo* archetype. To mimic such key characteristics, various systems have been developed to date [38–43]. In particular, *in vitro* BBB models provide two compartments separated by the BBB, grown on a microporous membrane, which allows the exchange of molecules between the apical compartments and the basal compartments. Pore sizes of membranes available are: 0.4, 1, 3, 5, 8 μm, depending on the solute to be investigated. Research has been very much enhanced by the availability of Transwell, a commercial BBB *in vitro* system. Upper chamber of Transwell insert, generally functions as the vascular side while the bottom one acts as the parenchymal side. *In vitro* BBB systems include the use of endothelial monocultures of different origin: murine, rat, porcine, bovine, monkey, human cerebral endothelial cells. Cell lines or primary monocultures can be used. Cell lines are generated by immortalization, they reach the confluence in a few days, allowing an high number of experiments in a short time. Primary cell cultures are isolated from tissue explants and maintained in culture. They closely mimic the *in vivo* state but it's difficult to remove surrounding cells from endothelial fraction [44]**.** Besides, they lose their features in culture after few passages, going to senescence. Costs of monocolture model are moderate, but the major disadvantage of this model is the absence of stimulating factors of the neurovascular unit. In order to maintain brain endothelial phenotype and functionality, the presence of brain microenvironment is needed. In addition to brain endothelial layer, also astrocytes and pericytes can be co-cultured, improving barrier properties. In a double co-culture system, endothelial cells are cultured on an insert of the Transwell and astrocytes at the bottom site of the plate. In triple co-culture system endothelial cells and pericytes are cultured respectively on the top and bottom of the insert and astrocytes grow on the bottom of the plate [39]**.** However, as reported in literature, the brain endothelial cells retain the microvascular barrier properties even without astrocytes and pericytes assistance [45].

1.1.7 Static versus dynamic *in vitro* BBB model

Static *in vitro* systems, such as Transwell, still exclude the importance of *in vivo* physiological conditions, such as the shear stress exerted on the wall of the vessel, to which BBB endothelial cells are exposed (Fig. 6). Shear stress of blood flow may enhance the tightness of endothelial cells. Cells are stimulated, resulting a functional and phenotype alteration. Therefore, in recent years flow-based microfluidic *in vitro* BBB systems are developed in order to more closely mimic *in vivo* condition. Chip can be designed so that the channel dimension and the flow rate exerted on the cells, realistically simulate the physiological microenvironment [46]**.** Besides, they also allow to carry out permeability studies in dynamic condition. To validate the BBB model, 3 methods can be employed: TEER measurement to evaluate the tightness of the layer, cell imaging and permeability assay to evaluate selectivity of the barrier to compounds [47]. TEER is used to monitor cell growth and development of the tight junctions. To calculate TEER value in Ωcm^2, resistance of the blank filter (R_i) is subtracted from cell layer resistance (R_f) at each time point and normalized for area (A).

$$\boldsymbol{TEER = (Rf - Ri)\, A}$$

However, the measured permeability could be wrongly estimated due to multiple layers grown on filter or due to holes and leakages. Others methods to validate the tightness is the evaluation of expression of tight junctions marker proteins by indirect immunofluorescence through confocal fluorescence analysis. In this case, barrier imperfections can be easily detected. Moreover, another approach to study the permeability is to quantify the crossing of detectable tracers. Permeability of the monolayer to compounds, for example Bovine serum albumin (BSA) or dextran at several molecular weights: 4-20-70 kDa, can be assessed by measuring the rate of diffusion across the membrane in flow condition from the donor chamber of the system to the acceptor chamber. The medium is collected at each scheduled time. Therefore the fluorescence is measured by fluorescence spectrophotometer and is converted to concentration. The solute permeability P of the monolayer is calculated according to the following equation.

$$\boldsymbol{P = \left(\frac{\Delta C_A}{\Delta t}\right) \times V_A / (C_D \times S)}$$

Where $\frac{\Delta C_A}{\Delta t}$ is the increase in fluorescence concentration in the acceptor chamber during the time interval Δt, C_D is fluorescence concentration in the donor chamber (assumed to be constant during the experiment), V_A is the volume of the acceptor chamber, and S is the surface area of the filter [34].

A) 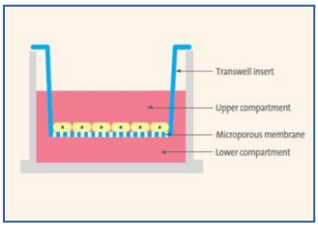

B) 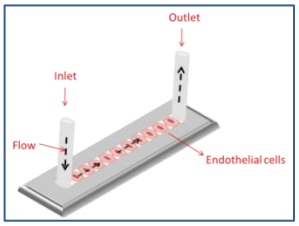

Figure 6 . Static (A) and dynamic (B) *in vitro* models of the blood-brain barrier.

1.2 REFERENCES

1. Roco, M. C. Nanotechnology: convergence with modern biology and medicine. Curr. Opin. Biotechnol. 14, 337–346 (2003).

2. Duncan, T. V. Applications of nanotechnology in food packaging and food safety: Barrier materials, antimicrobials and sensors. J. Colloid Interface Sci. 363, 1–24 (2011).

3. FAROKHZAD, O. & LANGER, R. Nanomedicine: Developing smarter therapeutic and diagnostic modalities☆. Adv. Drug Deliv. Rev. 58, 1456–1459 (2006).

4. Wong, C. et al. Multistage nanoparticle delivery system for deep penetration into tumor tissue. Proc. Natl. Acad. Sci. U. S. A. 108, 2426–2431 (2011).

5. Fawell, S. et al. Tat-mediated delivery of heterologous proteins into cells. Proc. Natl. Acad. Sci. U. S. A. 91, 664–668 (1994).

6. G. Panyutin, I., I. Onyshchenko, M., A. Englund, E., H. Appella, D. & D. Neumann, R. Targeting DNA G-Quadruplex Structures with Peptide Nucleic Acids. Curr. Pharm. Des. 18, 1984–1991 (2012).

7. Santra, S. et al. Rapid and effective labeling of brain tissue using TAT-conjugated CdS:Mn/ZnS quantum dots. Chem. Commun. (Camb). 3144–3146 (2005). doi:10.1039/b503234b

8. Rothbard, J. B. et al. Conjugation of arginine oligomers to cyclosporin A facilitates topical delivery and inhibition of inflammation. Nat. Med. 6, 1253–1257 (2000).

9. Xu, L., Zhang, H. & Wu, Y. Dendrimer advances for the central nervous system delivery of therapeutics. ACS Chem. Neurosci. 5, 2–13 (2014).

10. Yao, L. et al. Facilitated brain delivery of poly (ethylene glycol)–poly (lactic acid) nanoparticles by microbubble-enhanced unfocused ultrasound. Biomaterials 35, 3384–3395 (2014).

11. Abbott, N. J., Patabendige, A. A. K., Dolman, D. E. M., Yusof, S. R. & Begley, D. J. Structure and function of the blood–brain barrier. Neurobiol. Dis. 37, 13–25 (2010).

12. Pardridge, W. CNS drug design based on principles of blood-brain barrier transport. J. Neurochem. 70, 1781–1792 (1998).

13. Veszelka, S., Bocsik, A., Walter, F. R., Hantosi, D. & Deli, M. A. Blood-brain-barrier co-culture models to study nanoparticle penetration : focus on co-culture systems. 59, 1–12 (2015).

14. Mahar Doan, K. M. et al. Passive permeability and P-glycoprotein-mediated efflux differentiate central nervous system (CNS) and non-CNS marketed drugs. J. Pharmacol. Exp. Ther. 303, 1029–1037 (2002).

15. Begley, D. J. Delivery of therapeutic agents to the central nervous system: the problems and the possibilities. Pharmacol. Ther. 104, 29–45 (2004).

16. Silva, G. a. Nanotechnology approaches to crossing the blood-brain barrier and drug delivery to the CNS. BMC Neurosci. 9 Suppl 3, S4 (2008).

17. Lu, W. et al. Receptor-mediated transcytosis: A mechanism for active extravascular transport of nanoparticles in solid tumors. J. Control. Release 161, 959–966 (2012).

18. Gao, H. et al. Glioma-homing peptide with a cell-penetrating effect for targeting delivery with enhanced glioma localization, penetration and suppression of glioma growth. J. Control. Release 172, 921–8 (2013).

19. Hirose, M. The structural mechanism for iron uptake and release by transferrins. Bioscience, biotechnology, and biochemistry 64, 1328–36 (2000).

20. He, Q., Mason, A. B., Nguyen, V., Macgillivray, R. T. A. & Woodworth, R. C. The chloride effect is related to anion binding in determining the rate of iron release from the human transferrin N-lobe. Biochem. J. 915, 909–915 (2000).

21. Kasvosve, I. et al. Effect of transferrin polymorphism on the metabolism of vitamin C in Zimbabwean adults. Am. J. Clin. Nutr. 75, 321–5 (2002).

22. Beutler, E. et al. Molecular characterization of a case of atransferrinemia. Blood 96, 4071–4 (2000).

23. Lécureuil, C. et al. Transgenic mice as a model to study the regulation of human transferrin expression in Sertoli cells. Hum. Reprod. 19, 1300–7 (2004).

24. Bloch, B., Popovici, T., Levin, M. J., Tuil, D. & Kahn, a. Transferrin gene expression visualized in oligodendrocytes of the rat brain by using in situ hybridization and immunohistochemistry. Proc. Natl. Acad. Sci. U. S. A. 82, 6706–10 (1985).

25. Nicolson, G. L., Inouã, T., Pelt, C. S. Van & Cavanaugh, P. G. Differential Expression of a Mr ~ 90 , 000 Cell Surface Transferrin Receptor-related Glycoprotein on Murine B16 Metastatic Melanoma Sublines Selected for Enhanced Brain or Ovary Colonization1. (1990).

26. Qian, Z. M., Li, H., Sun, H. & Ho, K. Targeted drug delivery via the transferrin receptor-mediated endocytosis pathway. Pharmacol. Rev. 54, 561–587 (2002).

27. Moos, T. & Morgan, E. H. Transferrin and transferrin receptor function in brain barrier systems. Cell. Mol. Neurobiol. 20, 77–95 (2000).

28. Sade, H. et al. A human blood-brain barrier transcytosis assay reveals antibody transcytosis influenced by pH-dependent receptor binding. PLoS One 9, e96340 (2014).

29. Béduneau, A., Saulnier, P. & Benoit, J. P. Active targeting of brain tumors using nanocarriers. Biomaterials 28, 4947–4967 (2007).

30. Huile, G. et al. A cascade targeting strategy for brain neuroglial cells employing nanoparticles modified with angiopep-2 peptide and EGFP-EGF1 protein. Biomaterials 32, 8669–8675 (2011).

31. Liu, L. et al. Polymeric micelles anchored with TAT for delivery of antibiotics across the blood-brain barrier. Biopolymers 90, 617–623 (2008).

32. Falanga, A., Galdiero, M. & Galdiero, S. Membranotropic Cell Penetrating Peptides: The Outstanding Journey. Int. J. Mol. Sci. 16, 25323–25337 (2015).

33. Guarnieri, D. et al. Shuttle-Mediated Nanoparticle Delivery to the Blood-Brain Barrier. Small 9, 853–862 (2013).

34. Booth, R. & Kim, H. Characterization of a microfluidic in vitro model of the blood-brain barrier (μBBB). Lab Chip 12, 1784 (2012).

1.3 AIM OF THE THESIS

Most conventional treatments are severely hindered from entering the brain parenchyma. Ability of nano-sized systems to specifically target and penetrate across the blood-brain barrier (BBB) can be exploited to an effective brain therapy. Physico-chemical properties of nanoparticles (NPs) such as, small size, possibility to being functionalized with ligands, ability to transport cargo and the potential capacity to access isolated parts of the body, including brain, create a lot of interest to develop NPs for the treatment of CNS diseases. In this contest the aim of this work is to design a new NP able to recognize and translocate across the cerebral endothelium and investigate the effects of physico-chemical parameters on targeting and crossing of the BBB, under dynamic conditions. It is widely reported that NPs enter the cells using a cell-mediated mechanism called endocytosis. After endocytosis, endosomes can fuse with lysosomes, determining the NP degradation or can transport their cargo by transcytosis process. Specific endogenous ligands, such as transferrin (Tf), insulin and low density lipoprotein are able to take advantage of the Receptor-Mediated-Transcytosis (RMT) mechanism to cross the BBB. Surface functionalization of NPs with ligand-mimicking peptides allows to penetrate through the BBB and to achieve the CNS. Recent studies demonstrate *in vitro* and *in vivo* that CRTIGPSVC (CRT) peptide targets the complex Tf/TfR, improving the effectiveness in transporting cargo across the BBB, in a specific manner. CRT is an iron-mimicking peptide which can be exploited as RMT-targeting ligand. The identification of overexpressed TfRs on the BBB is needful in order to target the cerebral endothelium exploiting RMT mechanism. To this aim for the first time a rapid, simple and quantitative methodology based on Isothermal Titration Calorimetry (ITC) coupled with bEnd.3 confluent cell layers cultured around biocompatible templating microparticles has been used in order to demonstrate the number of TfRs onto the cell membrane and study the energetics of their interaction with the transferrin. Data demonstrated that the value of TfRs/cell reveals a 100-fold increase in the number of TfRs per bEnd.3 cells compared to endothelial cells not of brain (HUVECs).

In order to improve the NP transport across the cerebral endothelium, avoiding lysosomal entrapment, NP has been functionalized with CRT coupled with a cell-penetrating-peptide (CPP). It is reported that *in vitro* brain delivery of model NPs conjugated with the CPP gH625 (gH) is efficiently enhanced. gH is a membranotropic peptide, derived from Herpes simplex virus type 1. Nevertheless, because of their non-specific affinity to different cells, gH625-mediated brain delivery systems could show a non-specific distribution in the

human body, after systemic administration. Therefore, in this work, to overcome the CPP lack of specificity, we hypothesized that the synergic effect of CRT and gH conjugated to NPs should improve the targeting and crossing through the BBB. In order to demonstrate this hypothesis, *in vitro* biological characterization of dual-functionalized NPs has been performed. In the first step, sub-100 nm CRT-NPs, made up of a biodegradable poly (D,L-lactic-co-glycolic acid) (PLGA)-block-polyethylene glycol (PEG) copolymer (namely PELGA), have been synthetized. Both PEG and PLGA meet FDA approval criteria for clinical use as drug adjuvants. Cellular uptake in static and flow conditions and ability of peptide to enhance NP crossing of a murine endothelial monolayer have been investigated. In the second step, we synthesized CRT and gH625 dual-functionalized PELGA NPs with three different ratios of peptides: gH/CRT: 33%-66% ; gH/CRT: 50%-50%; gH/CRT: 66%-33%. Results of *in vitro* BBB crossing, in static condition, demonstrated that decoration with CRT peptide promotes NP overcoming of BBB. Moreover, NP transport of dual-functionalized NPs is highest for gH/CRT_33/66. We also investigated how this NP functionalization can affects the targeting of NPs to BBB endothelium in a parallel plate flow chamber named Glycotech system. According to the NP crossing results, gH/CRT_33/66 NPs display the higher targeting ability. Because Transwell systems used for NP transport assays still exclude the importance of *in vivo* physiological conditions, flow-based microfluidic *in vitro* BBB system has been developed in order to more closely mimic *in vivo* environment. Firstly a new method to fabricate circular microchannels has been reported. The advantage of cell adhesion and growth in the circular shape compared to square microchannel has been also demonstrated. Cells are able to form an homogeneous monolayer that resembled the endothelial tissue of capillary. Hence, a new microfluidic *in vitro* BBB model system has been engineered. A protocol of cell seeding and culturing in the new microfluidic system has been developed. Data demonstrated the capability of the microfluidic device to allow the growth and the correct formation of the murine brain endothelial layer (bEnd.3) and to quantify the transport ability of functionalized NPs.

These findings manifest a cooperative effect of gH and CRT peptides in enhancing transport across the BBB when exposed on NP in percentage 33%/66%, respectively. Therefore the novel NP could be regarded as a promising carrier to deliver drugs across the BBB for the treatment of brain diseases.

2 CHAPTER 2

Active targeting and transport across the blood-brain barrier of CRTIGPSVC-functionalized nanoparticles.

2.1 ABSTRACT

Brain drug delivery systems have been developed to bypass the blood-brain barrier (BBB) in order to therapeutically target central-nervous system (CNS) diseases. The most common strategy used from many nanocarriers to reach the brain is to exploit the BBB physiology. Both receptors and mimic-physiological ligands can be used to transport nanoparticles (NPs) into the CNS. Here, we present a new theranostic platform based on biodegradable nanoparticles functionalized with CRTIGPSVC (CRT) peptide, which functionally mimics the endogenous iron, recognizes selectively the brain endothelium and promotes the BBB crossing. *In vitro* experimental data indicate that NP functionalization with CRT peptide is a promising brain delivery system due to its high efficacy to translocate across the murine BBB, both in static and dynamic conditions.

2.2 INTRODUCTION

Drug transport to the brain for the treatment of CNS diseases is limited by the presence of the BBB. To overcome this barrier many delivery strategies have been attempted, such as local injection, induction of enhanced permeability [1]. Among others, nanotechnologies play an important role in developing strategies for brain drug delivery. In the last decades, several methods have been designed to overcome or exploit the transport systems of the BBB. These strategies are based upon nanocarriers usage. The targeted delivery of nanocarriers represents the alternative strategy to conventional invasive and low effective brain treatments. A promising strategy to control the delivery of drugs in their action site is represented by the use of nanoparticles (NP). NPs are defined as particulate dispersions or solid particles with a size in the range of 1-100 nm. Depending on the method of preparation of NPs, it is possible to obtain "nanocapsules", where the drug is encapsulated

within a cavity formed by a single polymer membrane, or "nanospheres", where the drug is linked physically to the surface. By using of NPs, the drug can be transported to the place of action, encapsulating drug and enhances drug concentration in target tissues, in this way, lower doses of drug are required, minimizing undesirable side effects to healthy tissues. Some examples of NPs widely studied for drug delivery are liposomes, dendrimers and metal containing NP. Different types of NPs are getting closer to clinical use such as liposomes, solid lipid NPs, polymeric NPs, metal NPs, Quantum dots. An ideal NP should: 1) recognize selectively the targeting tissue 2) promote brain drug delivery 3) have long circulation time 4) protect the cargo from enzymatic degradation 5) have low immunogenicity 6) have good biocompatibility [3]. Usually, NPs enter the cell by endocytic pathway. After endocytosis, endosomes fuse with lysosomes, in which the acidification (pH < 5.5) allows the degradation of the content or can deliver the cargo across the BBB. In order to escape endo-lysosomal pathway and deliver the cargo across the BBB, the chemico-physical modulation of the NP surface plays major role in determining the fate of the particles. For example, when endogenous ligands bind to specific receptors, they are taken up into the brain endothelial cells by endocytosis. NPs functionalized with these ligands can be also taken up, enabling BBB-impermeable drugs to enter the BBB. Therefore, the surface functionalization of nanocarriers with specific ligands such as Tf, insulin and low density lipoprotein offers the possibility to recognize and cross the BBB endothelium via recognition of specific receptors, overexpressed by the cells, and through mechanism of transcytosis. Receptor-mediated transcytosis (RMT) is considered the most used strategy, among all the methods. The exploitation of RMT has already been proposed for the transport of biologics into the brain [4–6]. Usually specific ligands only have high affinity for specific receptors, however often are inefficient to promote endocytosis [7]. Therefore the main limitation of RMT is associated with the low efficiency of BBB crossing and the achievement into the CNS. One significant drawback of the RMT systems is their fairly ubiquitous expression, which leads to peripheral organ uptake. When this level of expression is combined with the fairly modest crossing capacity, relatively low levels of brain uptake result [8]. Researchers have been focusing substantial effort on identifying new BBB RMT targets. Many of them were identified through the screening of combinatorial peptide libraries. Recently, Staquicini et al [9] have identified a new sequence CRTIGPSVC (CRT), able to recognize selectively brain endothelium and to enhance brain crossing of viral particles. TfR is highly expressed on immature erythroid cells, placental tissue, and rapidly dividing cells, both normal and malignant. Furthermore it is expressed on hepatocytes and endothelial cells of the BBB [10]. TfR mediates iron delivery to the brain

parenchyma via binding and intracellular trafficking of the iron-binding protein Tf [11]. Internalization of the Tf-TfR complex leads to the endosomal compartments in which the acidification allows the release of iron from the ligand. Iron is transported into the cytoplasm and is trancytosed, whereas the apo-transferrin (apo-Tf) remains tightly bound to its receptor until it reaches the plasma membrane. Here, the apo-Tf rapidly dissociates from the receptor at neutral pH [12]. The free receptor, on the cell surface, is available for another cycle of RMT. Staquicini et al. demonstrated *in vitro* that the BBB targeting peptide CRT selectively interacts with apo-transferrin (apo-Tf) to induce allosteric conformational changes that functionally mimic iron through a non-canonical ligand-directed mechanism (Fig. 1)

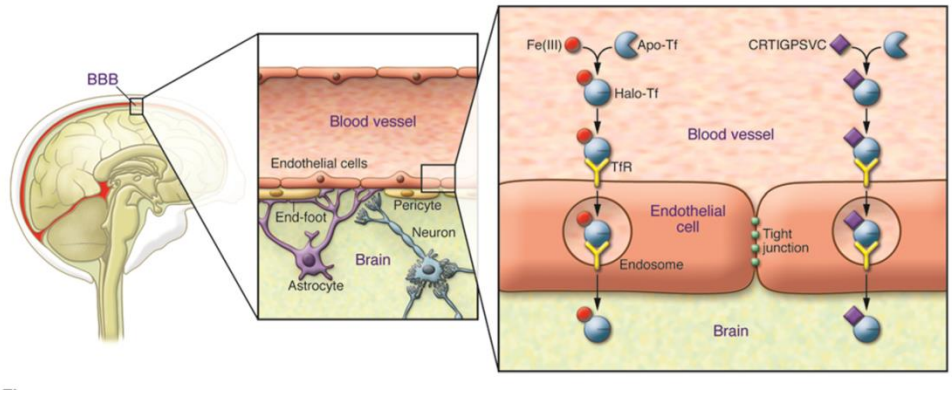

Figure 1: Transcytosis of the iron-mimicking CRT peptide. *D. Nathanson and P. S. Mischel, "Charting the course across the blood-brain barrier," J. Clin. Invest., vol. 121, no. 1, pp. 31–33, 2014.*

Besides, *in vivo* it was demonstrated the internalization and transcytosis of targeted phage particles into the normal mouse brain. In order to develop a nanocarrier system able to target and cross the BBB, here we report the ability of CRT functionalized PLGA-PEG (PELGA) nanoparticles to target and cross the cerebral endothelium. PELGA NPs can provide better biocompatibility, higher reproducibility, higher pay-load properties, easiness in functionalization and excellent stability both *in vitro* and *in vivo* [13]. In particular, it was recently reported on the versatility of PELGA nanoparticles as efficient drug delivery systems [14–17]. In this work, we developed CRT-functionalized PELGA NPs by using the nanoprecipitation method, in order to evaluate the capability of this peptide to transport the

NP across the BBB. To address this issue, first, *in vitro* synthesis and characterization of peptide alone are performed. Second, CRT-NPs are validated in terms of cell type specificity, uptake and permeability to the BBB. Our results clearly demonstrate the ability of CRT peptide to target and cross the brain endothelium when conjugated to polymeric nanoparticles thus paving the way to the design of novel multifunctional nanocarriers for delivery of therapeutic agents to the central nervous systems (CNS).

2.3 RESULTS AND DISCUSSION

2.3.1 Expression analysis of Transferrin Receptor

The delivery of iron into cells in general begins with diferric-Tf binding to the cell surface receptor [18]. The TfR is an integral membrane glycoprotein consisting of two identical 95.000-Da subunits linked by a disulfide bridge. Each subunit can bind one Tf molecule. TfR is a member of a class of cell surface receptors characterized by a rapid, constitutive internalization [19]. In order to demonstrate that brain endothelium overexpresses the transferrin receptors, these ones were stained with TfR antibody in two different endothelial cell types: immortalized mouse brain endothelial cell line (bEnd.3) used as model of brain endothelium and primary human umbilical vein endothelial cells (HUVECs) used as model of endothelium not of brain. Confocal images for each cell type were acquired and the fluorescence intensity of TfR was analyzed by imageJ software. Results in Fig. 2A show that in BBB endothelium TfR signal is higher than endothelium not of brain (HUVECs). In particular the fluorescence intensity is about 3-fold higher for bEnd.3 compared to the control, demonstrating that bEnd.3 overexpress TfR. Data were confirmed by confocal images of TfR immunostaining in bEnd.3 (Fig. 2B) and in HUVECs (Fig. 2C).

We also investigated the Tf binding to its receptors in near-physiological conditions when cells were grown on dextran microbeads ranging from 67 to 80 µm named Cytodex [20]. We obtained the energetics of ligand/receptor interactions and simultaneously the number of receptors on the cells by using Isothermal Titration Calorimetry (ITC). ITC is an important methodology to determine the ligand specificity to its receptor and is able to distinguish between specific and nonspecific interactions. The binding curve shown in Fig.1 provided the complete thermodynamic profile (i.e., binding constant (K_b), enthalpy change ($\Delta H°$),

entropy change ($\Delta S°$), Gibbs energy change ($\Delta G°$) of the interaction between Tf/TfR. The revealed affinity between transferrin (Tf) and transferrin receptors (TfRs) in both systems is very high, Kd values are in the order of nM. The value of TfRs/cell reveals a 100-fold increase in the number of TfRs per bEnd.3 (Fig. 2D) compared to endothelial cells not of brain (HUVECs) (Fig. 2E).

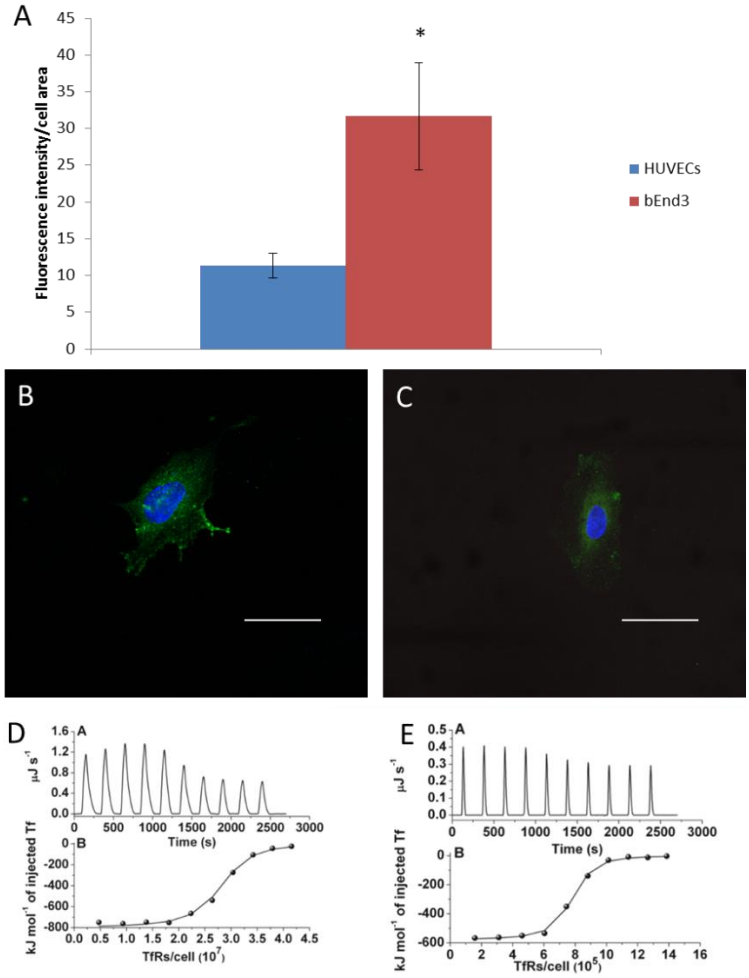

Figure 2: (A) Expression analysis of TfR in bEnd.3 and HUVEC cells. Data are presented as the mean ± SD (n = 30), (*) P < 0.001. Confocal images of Transferrin receptor expression in bEnd.3 (B) and HUVECs (C). Green: Transferrin receptor; blue: nuclei. Bar 50 µm. (D) ITC raw data for titration of Tf solution (1µM) into the solution of bEnd.3 cells (1800000 cells/mL) cultured on Cytodex microbeads (A) The solid circles are the experimental data obtained by integrating the raw data and subtracting the heat of Tf dilution into the buffer. The solid line represents the best fit obtained with the independent-binding site model (B). (E) ITC raw data for titration of Tf solution (0.1µM) into the

solution of HUVEC cells (5600000 cells/mL) cultured on Cytodex microbeads (A). The solid circles are the experimental data obtained by integrating the raw data and subtracting the heat of Tf dilution into the buffer. The solid line represents the best fit obtained with the independent binding site model (B).

After cell seeding, the surface of Cytodex beads appears rough compared to original beads indicating the presence of the cells on it. Moreover, confocal microscopy images further confirm the presence of a confluent layer of cells on the Cytodex surface (Figs. 3 A, B). In particular, phalloidin staining of the actin cytoskeleton demonstrates the correct spreading of the cells (Fig. 3 C).

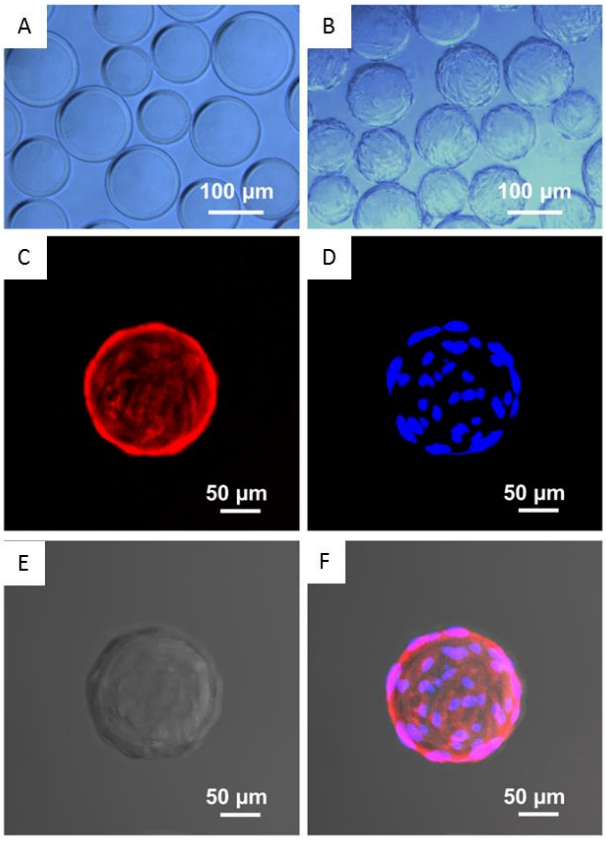

Figure 3: Phase contrast microscopy micrographs of Cytodex microsphere suspension before (A) and after (B) cell seeding. Maximum projection of z-sectioning images obtained by confocal microscopy with 10 × objective of a Cytodex microsphere after bEnd3 cell seeding (C-F). Actin microfilaments are stained in red by Phalloidin-TRITC (C), cell nuclei are represented in blue by DAPI (D) and the Cytodex is acquired in transmitted light (E). Merge of the three channels is reported in F.

2.3.2 Peptide synthesis and characterization

The CRT peptide (seq. CRTIGPSVC) was synthesized using the standard solid-phase-method (SSPM). Fig. 3 shows the structure (A) and mass spectrum (B) of peptide. In order to investigate the intracellular distribution, CRT peptide was conjugated with the Rhodamine B dye. The rhodaminated peptide was obtained with good yields (30–40%) after RP-HPLC purification. In Fig. 4 the structure (C) and mass (D) spectrum of rhodaminated-peptide are reported.

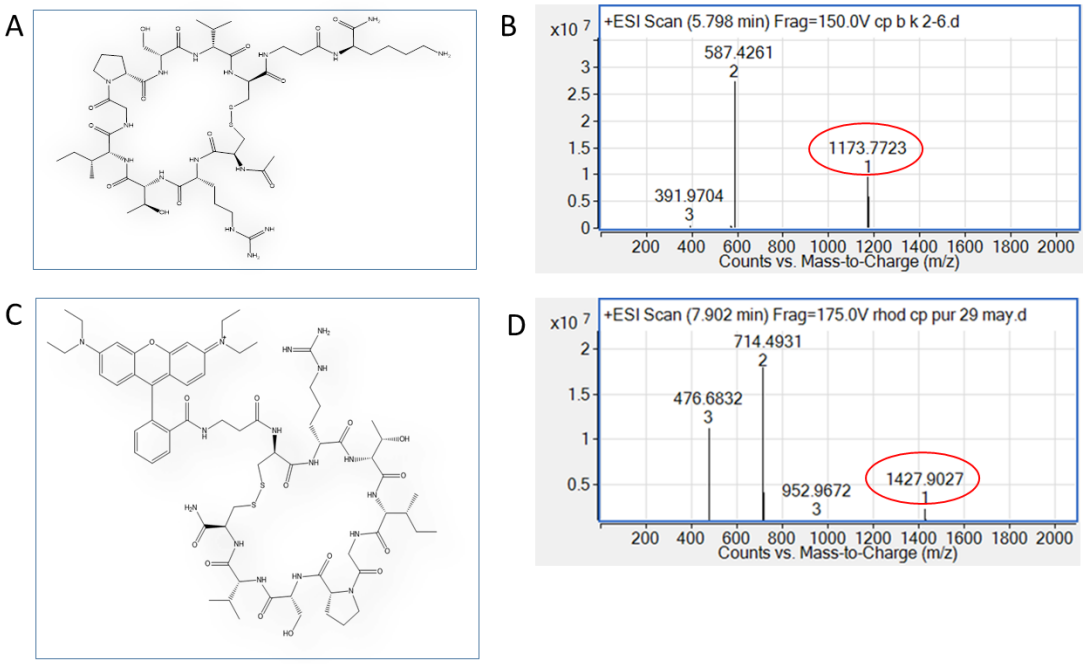

Figure 4. A, C structures and B, D mass spectra of CRT and rhodaminated-CRT, respectively.

2.3.3 Peptide cytotoxicity and uptake.

In order to choose the optimal peptide concentration for cellular uptake assays, we tested the effect of peptide on cytotoxicity. Results (Fig. 5 a) show that for bEnd.3 cells, after 1

and 4 hours of incubation for each concentration of peptide (1-5-10-20 µM), viability is almost 100%. HUVECs viability, decrease below 80%, for 20 uM of peptide after 4 hours of exposure. Thus, 10 uM CRT-Rhod was chosen as the optimal concentration for peptide uptake. To verify the cellular uptake of peptide, bEnd.3 and HUVECs were observed by confocal microscope after 1h and 4h of incubation with CRT-Rhod, at 37°C. As shown in Fig. 5 b) an higher spotted fluorescence was noticed within the cytoplasm of bEnd.3 at 4h than 1h of incubation. A slight fluorescence signal was observed in HUVECs cells only after 4h of exposure. No significant fluorescence signal was observed within the cytoplasm of HUVECs cells after 1h of incubation with peptide. Thus, CRT-Rhod peptide showed a significantly higher binding to brain endothelial cells compared to endothelial cells not of brain, according with cellular TfR expression.

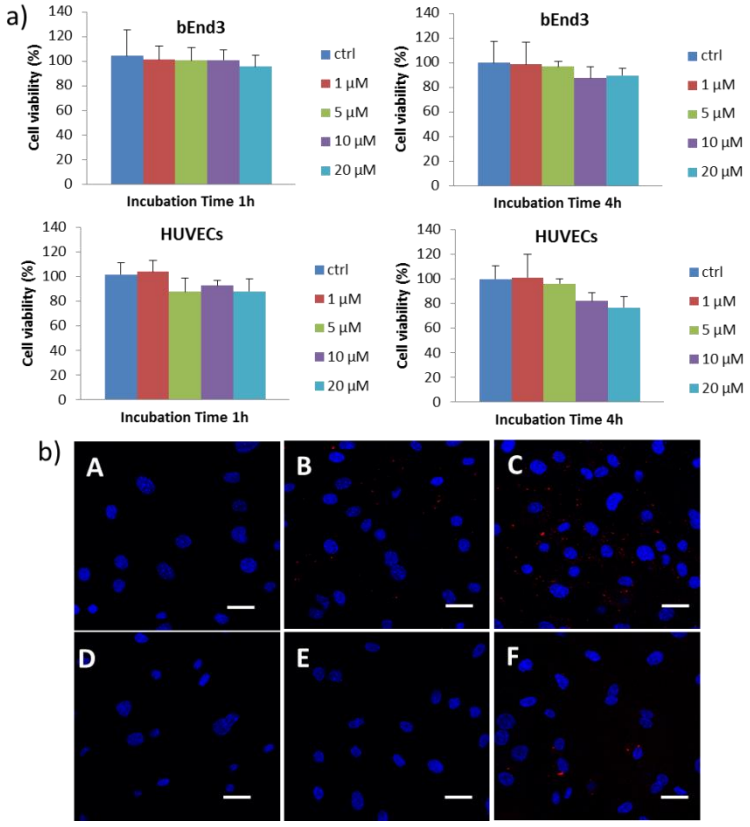

Figure 5: a) Alamar blue assay of CRT peptide in HUVECs and bEnd.3 after 1 and 4 h of incubation. Cell viability was expressed as percentage respect to the non-treated control cells and b) confocal images of untreated (A) or pretreated bEnd.3 with CRT peptide 10 µM for 1h (B) and 4h (C). Untreated HUVECs (D) and uptake after 1h (E) and 4h (F) of incubation with CRT peptide. Red: CRT peptide; blue: nuclei. Bar 50 µm.

2.3.4 NP synthesis and characterization

Blank and CRT functionalized NPs were synthesized by nanoprecipitation method. To investigate the effect of the peptide functionalization on the size of nanoparticles, we performed dynamic light scattering (DLS) measurements. After functionalization, the hydrodynamic size of nanoparticles with CRT in aqueous medium at pH 7 was found to be respectively 92.06 ± 1.53 nm, with polydispersity of 0.15 and size of blank nanoparticles was 88.24 ± 1.62 nm, with polydispersity values of 0.15 (Table 1).

To elucidate the colloidal stability of functionalized nanoparticles, which is a crucial parameter correlated to their functionalization, measurements of the zeta potential were carried out. For NPs alone z potential was -27.40 ± 0.66 mV and for peptide functionalized NP was -26.10 ± 1.17 mV. The size difference and the more positive charge of CRT-NP compared to blank NPs are probably due to the peptide exposure on NP surface. It is widely accepted that at high values of z-potential (over 30 mV, positive or negative) the electrostatic interactions between particles are strong enough for electrostatic stability, while at intermediate values of z-potential, near their isoelectric point, particles can flocculate.

NP	**Size [nm]**[a)] **± SD**	**PDI**	**ζ Potential** [a)] **[mV] ± SD**
Blank	88.24 ± 1.62	0.15	-27.40 ± 0.66
CRT	92.06 ± 1.53	0.15	-26.10 ± 1.17

Table 1: Size measurements and z potential of blank and CRT-NPs. [a)] Mean value ± SD, n=3.

2.3.5 NP cytotoxicity and uptake

The cytotoxic effect of blank and CRT-NPs was evaluated by Alamar Blue Assay on bEnd.3 cells. Results in Fig. 6 do not indicate a reduction of viability of cells treated for 24h with both blank (A) and functionalized NPs (B) at several NP concentrations in bEnd.3. In order to investigate the cell specificity of CRT-NPs, bEnd.3 and HUVECs were incubated for 24h at 37°C with blank and CRT NPs [0.05 mg/mL]. After incubation, to verify cellular uptake of NPs, cells were fixed and stained with DAPI. Samples were observed by confocal microscope. As shown in Figs. 6 (B-G) both blank (Fig. 6C) and CRT-NPs (Fig. 6D) are internalized by bEnd.3 cells. NPs are distributed as spots, mainly localized in the perinuclear region of the cell. An higher spotted fluorescence was detected within bEnd.3 incubated with CRT-NPs compared with blank NPs. No significant fluorescent signal was noticed for blank NPs (Fig. 6 F) and for CRT-NPs (Fig. 6 G) internalized by HUVECs. A perinuclear distribution of both blank and CRT-NPs was observed within bEnd.3.

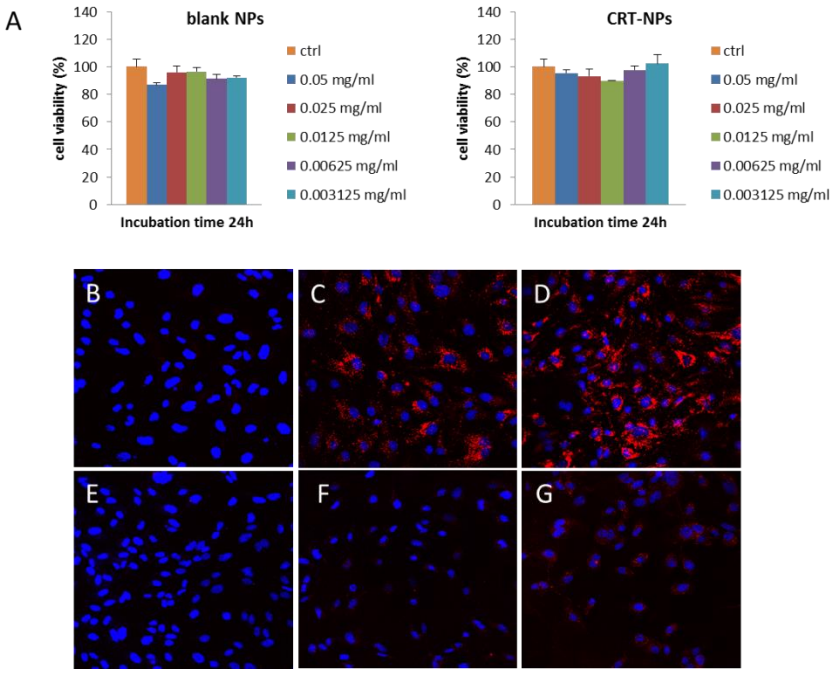

Figure 6: Cytotoxicity assay of blank and CRT-NPs in bEnd.3 after 1 day of incubation (A). Cell viability was expressed as percentage compared to the non-treated control cells. Confocal images of untreated bEnd.3 (B) or pre-treated with blank NPs (C) or CRT-NPs

(D) after 24h. Untreated HUVECs (E) and uptake of blank (F) and CRT-NPs (G) after 24 h. Red: CRT peptide; blue: nuclei. Bar 50 µm.

NP adhesion assay under flow condition by using Glycotech system.

Therefore we investigated how the surface functionalization could affects the targeting of NPs to the cerebral endothelium in a parallel plate flow chamber Glycotech system, a commercial device mimicking hydrodynamic conditions in the microcirculation. The volumetric flow rate Q (10 µl/min) was fixed to be equal for all the experiments. Based on these data, the mean velocity $U = \frac{Q}{wh}$ within the chamber was of about 0.066 mm/sec the shear rate $S = \frac{6Q}{h^2 w}$ was 1.55 sec^{-1} and the shear stress at the wall $\tau_w = \mu S$ was 1.86 × 10^{-3} Pa. The mean velocity used for the experiments is comparable with the blood velocity in the human capillary vessel that was calculated between 0.01 and 0.1 mm/sec (Ganong et al 2003) and the shear rate and the shear stress at the wall were sufficiently small to allow adhesion of nanoparticles to endothelial cells [21]. Fluorescent images analysis demonstrated that CRT NPs have the higher adhesion ability to bEnd.3 monolayer compared to blank NPs (Fig. 7). Data are reported as the percentage of mean gray value normalized for the 100 % of NP fluorescence intensity. As shown, the mean gray value percentage of CRT-NPs was found 0.79 % against blank NPs 0.44 %.

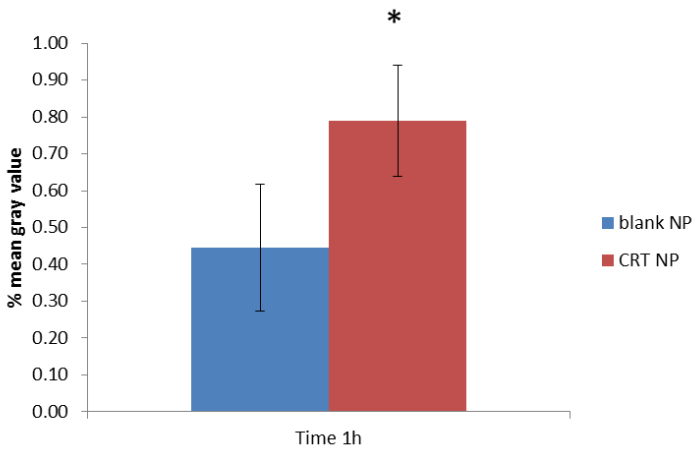

Figure 7: Adhesion assay of blank and CRT NPs to bEnd.3 monolayer under flow rate 10 µl/min by using Glycotech system. (*) P < 0.005.

2.3.6 NP transport across the BBB

bEnd.3 cells are able to form a confluent cell layer. The monolayer mimics permeability properties of the BBB [22]. The ability of CRT-NP to promote NP crossing of the bEnd.3 confluent monolayer was investigated in Transwell system (Corning). Data reported in Fig. 8 show that CRT-NPs cross more efficiently the endothelial layer than blank NPs. More precisely the permeability values of the BBB to functionalized NPs was 4.64×10^{-6} cm/sec and for blank NPs was 3.16×10^{-6} cm/sec.

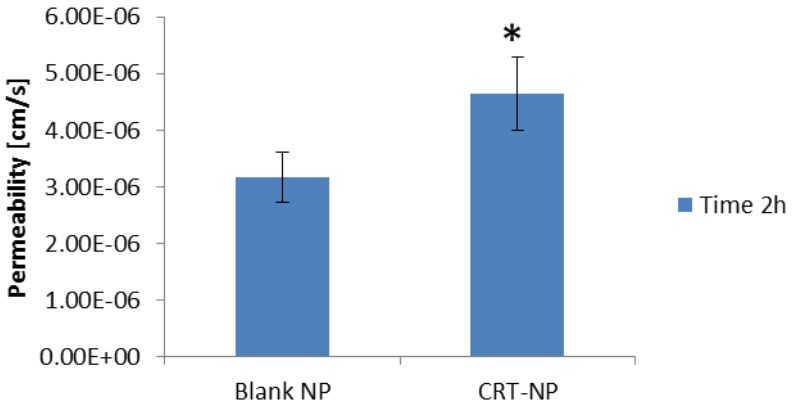

Figure 8: Effect of peptide functionalization in NP crossing of a confluent bEnd.3 cell monolayer. (*) $P < 0.005$.

2.4 MATERIALS AND METHODS

2.4.1 Cell culture

Immortalized mouse cerebral endothelial cells, (bEnd.3; American Type Culture Collection, Manassas, VA) were grown at 37°C and 5% CO_2 in DMEM with 4.5 g/L w/o phenol red (Gibco), supplemented with 10% FBS, 3.7 g/L sodium bicarbonate and 4 mM glutamine, 100U/mL penicillin and 0.1 mg/mL streptomycin, 1% non essential aminoacids. bEnd.3 used in all experiments were at passage 21-30.

Primary human umbilical vein endothelial cells (HUVECs; Lonza), used from passage 3 to 8, were cultured in Medium-200 (Cascade Biologics) supplemented with LSGS kit (Life Technologies).

2.4.2 Cell staining

The expression of TfR in bEnd.3 and HUVECs cells was investigated by immune-staining with anti-Transferrin Receptor antibody (Abcam). 1×10^4 bEnd.3 and HUVECs cells were seeded on round glass coverslips placed in 24 well plates. 24h after seeding, cells were fixed with 4% paraformaldehyde for 10 min. Tf receptors were localized by incubating samples first with the blocking buffer (BB) (0.5% BSA in PBS) and after with the anti-Transferrin polyclonal primary receptor (1 µg/mL) overnight at 4°C. Then, the Alexa-488 anti-Rabbit secondary antibody (Invitrogen) diluted in BB was incubated 1 h at room temperature (RT). To detect actin filaments, FITC-Phalloidin (Invitrogen) was used. After fixation and permeabilization, bEnd.3 cells were incubated for 30 minutes at RT. For nuclei staining DAPI (Sigma) was used.

2.4.3 Expression analysis of Transferrin Receptor

After cell staining for TfR and DAPI, in order to verify the expression of Transferrin Receptor, bEnd.3 and HUVECs were observed by confocal microscope (MP Leica TCS

SP5). 30 images of cells by type were acquired and analyzed. Transferrin expression analysis was performed by using imageJ software 1.44p, calculating the mean gray value of TfR signal. Mean gray value is the sum of the gray values of all the pixels in the selection divided by the number of pixels. To evaluate the area of each cell, the ROI manager tool allowed to pick out the shape cell region. Hence the mean gray value was calculated for each cell area.

2.4.4 Cell seeding on Cytodex

Pyrex glass vial was coated with Sigmacote (Sigma) for 5 min before use to prevent cell adhesion on the walls. Dextran microcarrier beads (Cytodex® 3 purchased from Sigma) were weighed in the vial and swelled with PBS for 3 h, at RT under gentle stirring. Afterwards the vial was autoclaved to prevent contamination. After sterilization, Cytodex suspension was decanted and PBS was removed to resuspend the beads at a concentration of 5 mg/ml in cell culture medium. 2 ml of Cytodex suspension were transferred into each well of a low attachment 6-well plate (Corning). 8×10^5 cells in 100 µl of cell culture medium were added to the Cytodex in the well. In order to allow cell adhesion to the surface of the microspheres, the 6-well plate was kept under stirring at 80 rpm overnight in incubator at 37 °C and 5 % CO_2. Stirring was stopped for 1 min every 15 min for the first 3 h from the seeding. After overnight incubation, 7 ml of Cytodex with adhered cells were collected and cells were fixed with 4 % paraformaldehyde for 10 min before ITC analysis. Cell adhesion on Cytodex was monitored by phase contrast microscopy. We assume that all the cells seeded were attached on the microbeads.

2.4.5 ITC experiments

Isothermal titration calorimetry (ITC) ITC experiments were performed using a Nano ITC Low Volume from TA Instruments (Lindon, UT, USA) with a cell volume of 170 µL. All solutions were accurately degassed before the ITC experiments to avoid the formation of air bubbles in the calorimeter cell. The sample cell was loaded with bEnd.3 or HUVEC cells cultured on Cytodex microbeads in PBS buffer solution, Tf instead was loaded into the computer-controlled microsyringe in the same buffer conditions. Injections were started after baseline stability had been achieved. Titration experiments were carried out at 298 K,

10 injections of 5 μL of Tf 1- 0.1 μM were added to the bEnd.3 or HUVEC cells cultured on Cytodex microbeads (1800000 - 5600000 cells/mL) every 250 seconds. Control experiments were carried out to calculate the heat of dilution for Tf in PBS solution. All the measurements were conducted at a continuous stirring rate of 250 rpm. Raw data were obtained as a plot of heat released against time and featured as a series of peaks for each injection. The calorimetric enthalpy for each injection was calculated after correction for the heat of Tf dilution, the area under raw data peaks was integrated by the analysis software of the instrument (NanoAnalyze software, version 2.4.1 (TA Instruments)) to obtain a plot of enthalpy change per mole of injectant (Tf) against the number of TfRs per cell. From the number of cells/mL was calculated the number of cells for each experiment. The number of TfRs was calculated taking into account the moles of added Tf, until the saturation occurs, this value correspond to half of the TfRs present in the sample cell. Holo -transferrin was previously shown to bind to the receptor with a stoichiometry of one Tf molecule per TfR monomer (stoichiometry Tf-TfR 2:1) . Each experiment was repeated up to three-five times in order to ensure reproducibility. Integrated heat data obtained for the titrations were fitted using a nonlinear least-squares minimization algorithm to a theoretical titration curve, using NanoAnalyze software, version 2.4.1 (TA Instruments). (reaction enthalpy change in kJ mol-1), (binding constant in M-1), and n (number of binding sites) were the fitting parameters obtained by the equivalent and independent binding sites model (Supporting Information, Equations S1-S13). The remaining thermodynamic parameters of the interaction were calculated using the Eq. 1

$$\Delta_b G^\circ = -RT \ln K_b \; (R = 8.314 \; J \; mol^{-1} \; K^{-1}, T = 298 \; K) \quad (1)$$

and Eq. 2:

$$T \, \Delta_b S^\circ = \Delta_b H^\circ - \Delta_b G^\circ \quad (2)$$

2.4.6 Peptide synthesis and characterization

CRT peptide was synthesized using standard solid-phase-9-fluorenyl methoxy carbonyl (Fmoc) method, by means of an automatic peptide synthesizer. Peptide was cleaved from the resin by means of standard TFA/TIS/Water (95/2.5/2.5) solution and then precipitated in cold ethyl ether. Purified CRT and was obtain by RP-HPLC starting from 5/95 (v/v) acetonitrile (ACN)/water solution containing 0.1% v/v TFA.

2.4.7 Rhodamine coupling procedure

Rhodamine-peptide conjugation was performed on solid-phase by a standard coupling procedure: peptides (1 eq), HBTU (5 eq), DIPEA (10 eq), and Rhodamine-B (5 eq) in anhydrous DMF. The reacting mixture was continuously stirred for 30 minutes at room temperature. After a second coupling procedure, Rhod-peptide was cleaved from resin and precipitated in cold ethyl ether. The reaction products were verified by analytical LC-MS and then purified by RP-HPLC using a 20/80 (v/v) acetonitrile (ACN)/water solution containing 0.1% v/v TFA.

2.4.8 Peptide cyclization

Purified CRT peptide was cyclized by air-oxidation method to allow the formation of the intra-chain disulfide bond between the two cysteine residues. Briefly, cysteinyl peptides (0.1 mg/mL) were dissolved in 0.1 M sodium carbonate (pH 8) and left to stand open to atmosphere under vigorous magnetic stirring until the reaction is complete (48 h). The products were monitored by LC-MS analysis. Cyclic peptide was lyophilized and purified as described above.

2.4.9 PLGA-CRT conjugate

The PLGA-Peptide conjugates were synthesized by a standard HBTU coupling procedure. Briefly, for CRT and Ctrl peptides, PLGA (1 eq), HBTU (5 eq), OximaPure® (5 eq), DIPEA (10 eq), and Peptide (1.5 eq) were dissolved in anhydrous DMSO for 48h at room

temperature. For gH625 peptide PLGA-NH_2 (1 eq), HBTU (10 eq), OximaPure® (10 eq), DIPEA (20 eq), and Peptide (2 eq) were used. The adducts were purified from unreacted reagents using dialysis bags (MWCO 6-8 kDa) against pure water and lyophilized. The reaction products were verified by ^{1}H-NMR spectroscopy.

2.4.10 PELGA

PLGA-PEG copolymer (namely PELGA) was synthesized via a coupling reaction between PLGA and PEG. Briefly, the carboxyl group of PLGA has been reacted with the terminal hydroxyl group of PEG: 1 eq of PLGA, 4 eq of PEG, 0.4 eq DMAP and 2 eq of DCC were dissolved in 10 mL of anhydrous DCM. After the reaction (2 days, RT, inert atmosphere), the residual DCC was changed into dicyclohexylcarbodiurea (DCU) by adding 10 □L of bidistilled water. Then DCM was evaporated and the mixture was dissolved in 10 mL of DMSO, filtrated and dialyzed (MWCO 6-8 kDa) for 1 day against ACN and for 2 days against water. Pure product was recovered after lyophilization and checked by 1H-NMR spectroscopy.

2.4.11 Amino-PLGA

PLGA was functionalized with ethylenediamine which act as a bridge between PLGA and Rhodamine (or peptide C-terminus) carboxylic groups. Briefly, 30 mg of PLGA 502h, 10.3 mg of DCC, 8.7 µl of DIPEA , 10.0 µl of ethylenediamine were dissolved in 2.5 mL of anhydrous DCM. After the reaction (1 day, RT, inert atmosphere), the residual DCC was changed into dicyclohexylcarbodiurea (DCU) by adding 10 µL of bidistilled water. Then the solution was filtered and precipitated dropwise into cold methanol, centrifuged and then placed under vacuum overnight. Pure product was checked by 1H-NMR spectroscopy.

2.4.12 Rhodamine-PLGA

PLGA-Rhodamine conjugation were performed by a standard coupling procedure: PLGA-NH2 (1 eq), HBTU (5 eq), DIEA (10 eq), and Rhodamine-B (5 eq) in anhydrous DMSO for 24 h at RT and then purified by dialysis bags (MWCO 6-8 kDa) against water for 3 days.

2.4.13 **NP preparation**

Rhodaminated PELGA-Peptide nanoparticles were prepared by nanoprecipitation method. Briefly, the proper amounts of copolymers and conjugates (Table 2) were dissolved in acetone and the obtained solutions mixed; final volume was adjusted to 1.3 mL. Afterwards, the solution was added dropwise (6 mL/h) with a syringe pump into 12.5 mL of distilled water under magnetic stirring (400 rpm). The solution was kept under magnetic stirring until all the organic solvent was evaporated (3-5 h) and the obtained NP suspension was sterilized with 0.22 µm membrane filter. Finally, the volume of the solution was reduced to 1 mL using Amicon® Ultra-4 centrifugal filter.

The final NP concentration (mg/mL of polymeric species) was estimated by fluorescence intensity measurements of Rhodamine-PLGA using a spectrofluorometer (Perkin Elmer) compared to fluorescence intensity of the initial NP concentration before filtration.

	Pelga (mg)	Plga-Rho (mg)	Plga-CRT (mg)	Plga (mg)	mg tot
Blank NP	1	0.4	-	0.8	2.2
CRT NP	1	0.4	0.4	0.4	2.2

Table 2: Amount of copolymers used for blank and CRT-NPs preparation.

2.4.14 **NP characterization**

Measurements of size and ζ-potential of NPs after filtration were made with a Zetasizer Nano-ZS (Malvern Instruments, Worcestershire, UK).

2.4.15 **Cytotoxicity assay**

Cell viability was quantified by the Alamar Blue Assay (Invitrogen) and compared to non-treated cells, which were used as a control. Briefly, 1×10^4 bEnd.3 and HUVECs cells were seeded in a 96-well and incubated for 1 and 4 h with Rhod-CRT at different concentration 1-5-10-20 µM. Cytotoxicity of the negative control peptide was also investigated. For NP cytotoxicity assay, bEnd.3 cells were incubated for 24h with blank NPs and CRT-NPs at several concentrations: 0.050, 0.025, 0.012, 0.006, 0.003 mg/mL. Alamar Blue Assay was performed according to the manufacturer's procedure. Absorbance of Alamar Blue reagent

solution was read at 570 nm and 600 nm by using a spectrofluorometer (Wallac 1420 Victor2, Perkin–Elmer, USA). All experiment were performed in triplicate.

2.4.16 Cellular uptake experiments

To perform peptide and NP uptake experiments about 5 x 10^4 bEnd.3 and HUVECs cells were seeded on round glass coverslips placed in 24 well plates. Cells were incubated for 1 and 4 h with CRT-Rhod 10 µM and for 24 h with NPs at 37°C and 5% CO_2. After incubation, samples were washed two times with PBS to remove non internalized peptide or NPs and fixed with 4% paraformaldehyde for 20 min. Finally, cell nuclei were stained with DAPI. Samples were observed by confocal MP microscope.

2.4.17 Glycotech assay

To perform NP adhesion assays, 4 × 10^5 bEnd.3 were seeded on round glasses (dia 60 mm) placed in Petri dishes (100 mm dia). The experiments were performed after 3 days from the seeding. Adhesion assay to an *in vitro* model of BBB grown on the glass coverslip were performed by using Glycotech system. The system consists of a PMMA flow deck with inlet and outlet bores, a silicon gasket and a glass coverslip (Fig. 8). The silicon gasket separates the acrylic flow deck and the glass and defines the flow area. The gasket used in the present experiments had a thickness *h* of 0.01 in and a width *w* of 1 cm. The inlet bore is connected to a syringe-pump through a silastic tube and the outlet bore to a reservoir. The volumetric flow rate *Q* (10 µl/min) was fixed to be equal for all the experiments. Based on these data, the mean velocity has been calculated with the following equation $U = \frac{Q}{wh}$ within the chamber and the shear rate $S = \frac{6Q}{h^2 w}$ and the shear stress at the wall $\tau_w = \mu S$ being 1.2 × 10^{-2} dyn s/cm^2 the viscosity of the medium. NP solutions at the final concentration of 0.2 mg/mL in cell culture medium supplemented with 40 mM HEPES buffer were flushed by using a 5 mL syringe allocated on a syringe pump. Flow is driven through the parallel plate flow chamber for 1h at 37°C in a plexiglass incubator. At the end of the experiment, cells were fixed after 2 washes with PBS to remove non adherent NPs. The percentage of mean gray value was analyzed by using imageJ software 1.44p.

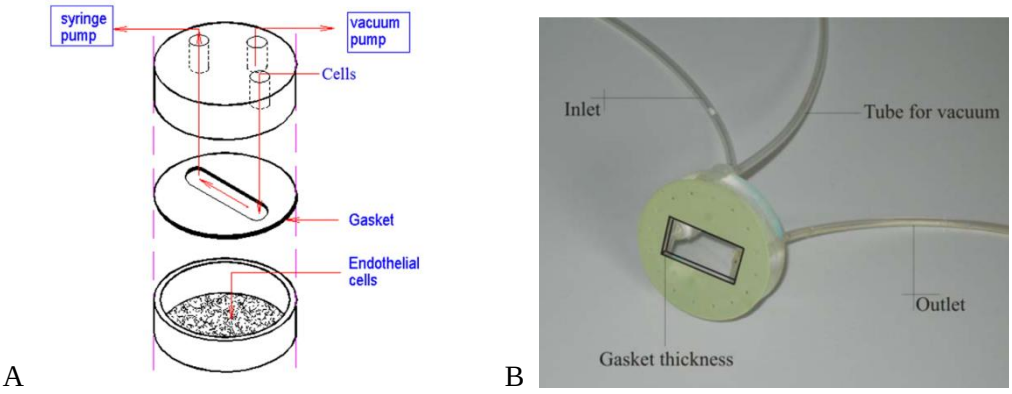

Figure 8: A) Schematic of the Glycotech flow chamber for studying cellular interaction. B) Picture of Glycotech system.

2.4.18 Permeability assay by Transwell system

bEnd.3 were seeded at a density of 3×10^4 cells/cm^2 on Transwell permeable inserts (6.5mm diameter, 3 µm pores size; Corning Incorporated, Corning, NY). Permeability experiments were performed on the monolayer 7 days after cell seeding, allowing sufficient time for the cells to develop the junctions between cells. On the day of experiment, Transwell insert filter was washed with PBS, and then the media of the donor chamber was filled with 150 µL cell culture medium w/o phenol red containing 0.1 mg/mL of blank NPs or CRT-NPs while the acceptor chamber was filled with 400 µL cell culture medium without phenol red. The samples of 400 µL were drawn every 30 min for 2h from the acceptor chamber and were then replaced with the same amount of fresh medium. The fluorescence tracer concentration in the samples was determined by a spectrofluorometer (Victor, Wallac, PerkinElmer) and the excitation and emission wavelengths were set to 557 and 578 nm, respectively, for NPs. The permeability to NPs of the bEnd.3 monolayer was calculated according to the following equation,

$$P = \frac{\frac{\Delta C_A}{\Delta t} \times V_A}{C_D \times S}$$

Where is the increase in fluorescence concentration in the acceptor chamber during the time interval, is fluorescence concentration in the donor chamber (assumed to be constant during the experiment), is the volume of the acceptor chamber, and S is the surface area of the filter. The experiments were performed in triplicate.

2.4.19 Statistical analysis

Results were expressed as mean ± standard deviation (SD). Statistical analyses were performed using a one-way analysis of variance (ANOVA). Results repeats were compared by analysis of variance (ANOVA), and a p value < 0.05 were considered statistically significant.

2.5 CONCLUSIONS

The nanoparticle ability to recognize the brain endothelium is an important requisite for successful brain therapy. The design of targeted delivery carriers has garnered significant attention in recent years because of the potential to achieve highly localized delivery to brain endothelium [5,8,23]. In order for a targeted delivery system to be effective, the functionalization with ligands which are able to bind specifically receptors overexpressed on the BBB is important in determining the drug delivery. In light of the wide variety of ligands proposed, in this work, CRT peptide has been chosen to selectively target the brain endothelium. Staquicini et al. previously demonstrated that phage clones displaying the iron mimicking CRT peptide, were able to target the complex Tf/TfR mediating the transport of the corresponding viral particles into the normal mouse brain. In this work, firstly, the overexpression of Tf receptor in brain endothelium has been demonstrated. After rhodaminated-peptide synthesis and characterization, viability of cells incubated with the CRT-Rhod at several concentration has been evaluated until 4h. Therefore, 10 µM of peptide has been chosen for bEnd.3 and HUVECs uptake assay. As demonstrated by confocal images, the uptake of CRT peptide in bEnd.3 is higher than HUVEC cells, according to the expression of cell Tf receptors. In order to investigate the ability of CRT to target nanoparticle to the cerebral endothelium selectively, NPs exposing CRT peptide have been synthesized and characterized. Confocal images show that bEnd.3 uptake of CRT-NP is higher than blank NP, on the contrary, no significant NP uptake was noticed in HUVECs both for blank and CRT-NPs. Therefore the ability of CRT peptide to carry the NP to the brain endothelium, selectively was also demonstrated *in vitro*. To verify the CRT-NP adhesion ability to murine cerebral endothelium under dynamic condition, Glycotech assay was also performed. In order to mimic physiological blood microcirculation velocity, 10 µl/min was setted as flow rate. For peptide functionalized NPs the percentage of mean gray value was found 1.8 times higher than blank NPs, thus CRT peptide is able to target the BBB also under flow condition. Afterwards the ability of CRT-NP to cross the cerebral endothelium, was also demonstrated. The rate of CRT-NP transported across the BBB is 1.5-fold higher than blank NPs.

Taken all together, our results are promising in the light of improving the BBB targeting of potential therapeutic nanosystems, holding advantageous alternative for the treatment of CNS diseases.

2.6 REFERENCES

1. de Boer, A. G. & Gaillard, P. J. Drug Targeting to the Brain. *Annu. Rev. Pharmacol. Toxicol.* **47,** 323–355 (2007).

2. Gaillard, P. J., Visser, C. C., Appeldoorn, C. C. M. & Rip, J. Enhanced brain drug delivery: Safely crossing the blood-brain barrier. *Drug Discov. Today Technol.* **9,** e155–e160 (2012).

3. Mc Carthy, D. J., Malhotra, M., O'Mahony, A. M., Cryan, J. F. & O'Driscoll, C. M. Nanoparticles and the blood-brain barrier: Advancing from in-vitro models towards therapeutic significance. *Pharm. Res.* **32,** 1161–1185 (2015).

4. Jones, A. R. & Shusta, E. V. Blood-brain barrier transport of therapeutics via receptor-mediation. *Pharm. Res.* **24,** 1759–1771 (2007).

5. Van Rooy, I., Mastrobattista, E., Storm, G., Hennink, W. E. & Schiffelers, R. M. Comparison of five different targeting ligands to enhance accumulation of liposomes into the brain. *J. Control. Release* **150,** 30–36 (2011).

6. Wong, H. L., Wu, X. Y. & Bendayan, R. Nanotechnological advances for the delivery of CNS therapeutics. *Adv. Drug Deliv. Rev.* **64,** 686–700 (2012).

7. Huile, G. *et al.* A cascade targeting strategy for brain neuroglial cells employing nanoparticles modified with angiopep-2 peptide and EGFP-EGF1 protein. *Biomaterials* **32,** 8669–8675 (2011).

8. Lajoie, J. M. & Shusta, E. V. Targeting Receptor-Mediated Transport for Delivery of Biologics Across the Blood-Brain Barrier. *Annu. Rev. Pharmacol. Toxicol.* **55,** 613–631 (2015).

9. Staquicini, F. I. *et al.* Systemic combinatorial peptide selection yields a non-canonical iron-mimicry mechanism for targeting tumors in a mouse model of human glioblastoma. *J. Clin. Invest.* **121,** 161–173 (2011).

10. Ponka, P. & Lok, C. N. The transferrin receptor: role in health and disease. *Int. J. Biochem. Cell Biol.* **31,** 1111–1137 (1999).

11. Moos, T. & Morgan, E. H. Transferrin and transferrin receptor function in brain

barrier systems. *Cell. Mol. Neurobiol.* **20,** 77–95 (2000).

12. Sade, H. *et al.* A human blood-brain barrier transcytosis assay reveals antibody transcytosis influenced by pH-dependent receptor binding. *PLoS One* **9,** e96340 (2014).

13. Bao, G., Mitragotri, S. & Tong, S. Multifunctional Nanoparticles for Drug Delivery and Molecular Imaging. *Annu. Rev. Biomed. Eng.* **15,** 253–282 (2013).

14. Biondi, M., Guarnieri, D., Yu, H., Belli, V. & Netti, P. A. Sub-100 nm biodegradable nanoparticles: in vitro release features and toxicity testing in 2D and 3D cell cultures. *Nanotechnology* **24,** 045101 (2013).

15. Graf, N. *et al.* $\alpha_V \beta_3$ Integrin-Targeted PLGA-PEG Nanoparticles for Enhanced Anti-tumor Efficacy of a Pt(IV) Prodrug. *ACS Nano* **6,** 4530–4539 (2012).

16. Nance, E. *et al.* Brain-Penetrating Nanoparticles Improve Paclitaxel Efficacy in Malignant Glioma Following Local Administration. *ACS Nano* **8,** 10655–10664 (2014).

17. Cantisani, M. *et al.* Biocompatible nanoparticles sensing the matrix metallo-proteinase 2 for the on-demand release of anticancer drugs in 3D tumor spheroids. *Colloids Surfaces B Biointerfaces* **135,** 707–716 (2015).

18. Aisen, P. Entry of iron into cells: A new role for the transferrin receptor in modulating iron release from transferrin. *Ann Neurol* **32,** S62–S68 (1992).

19. Gomme, P. T., McCann, K. B. & Bertolini, J. Transferrin: structure, function and potential therapeutic actions. *Drug Discov. Today* **10,** 267–273 (2005).

20. Iolanda Fotticchia, Daniela Guarnieri, Teresa Fotticchia, **Andrea P. Falanga**, Raffaele Vecchione, Concetta Giancola, Paolo A. Netti. *Colloids and surfaces b biointerfaces (under review).*

21. Decuzzi, P. & Ferrari, M. The role of specific and non-specific interactions in receptor-mediated endocytosis of nanoparticles. *Biomaterials* **28,** 2915–2922 (2007).

22. Zhang, W. & Smith, S. O. Mechanism of Penetration of Antp (43-58) into

Membrane Bilayers †. *Peptides* 10110–10118 (2005).

23. van Rooy, I. *et al.* Identification of Peptide Ligands for Targeting to the Blood-Brain Barrier. *Pharm. Res.* **27,** 673–682 (2010).

3 CHAPTER 3

Synergic effect of double functionalization with peptides in promoting NP transport across the cerebral endothelium.

3.1 ABSTRACT

The main obstacle in the treatment of Central-Nervous-System (CNS) diseases is the blood-brain barrier (BBB). In order to overcome this barrier, a new potential brain delivery system has been developed for specific targeting and transport through the BBB, based on dual-functionalized polymeric nanoparticle (NP). The ability of nanoparticle functionalized with CRTIGPSVC (CRT) peptide able to promote the specific transport across the BBB has been demonstrated in the previous chapter. In this work, in order to avoid nanoparticle accumulation inside lysosomal compartments, enhancing efficiency in crossing the BBB, the nanoparticle functionalization with CRT was coupled with the cell-penetrating Peptide (CPP) gH625 (gH). The aim is to investigate the efficacy of NP functionalized with CRT peptide and gH625 in promoting the translocation across the cerebral endothelium. Co-localization studies, adhesion and permeation assays across *in vitro* brain endothelial model, under dynamic conditions have been investigated. Results establish that the cooperative effect of CRT and gH on NPs may change the distribution of NP in the cell and strengthen the BBB crossing of NPs [1].

3.2 INTRODUCTION

In order to overcome the BBB, reaching the Central-Nervous-System (CNS), the modulation of physic-chemical properties of NPs such as surface charge, size and functionalization, play an important role in mediating their interactions with cell membrane and their intra-cellular fate. Several strategies have been developed to deliver drugs across BBB and increase the survival rate of patients in the CNS treatments. To combine targeting and crossing strategies, some researchers developed dual-functionalized carrier systems for targeted drug delivery across the BBB. For example functionalization with Transferrin (Tf) which is able to target selectively the BBB and reach the brain by Receptor-mediated-transcytosis (RMT) and with a cell penetrating peptide (CPP) due to translocate across the BBB [2,3]. However, the main limitation of RMT is associated with the low efficiency of BBB crossing and the achievement into the CNS. The aim of this work is to develop a new

nanoparticle able to enhance the crossing efficiency through a double peptide functionalization with gH625 (gH) and CRT peptides and to characterize the NP by using an *in vitro* BBB. In a previous work, it has been demonstrated that gH625-functionalized polystyrene NPs facilitate the delivery of nanoparticles across the murine BBB, leading to significant higher cell uptake and crossing [4,5]. gH625 is a membranotropic peptide, derived from the glycoprotein H (gH) of the Herpes simplex virus type 1. gH625 interacts with model membranes, merging with them and is able to traverse the membrane bilayer and to transport a cargo, like quantum dots, liposomes, NPs, and dendrimers into the cytosol and across the BBB [6,7]. Surface modification of NPs with gH625 may change the classical intracellular fate of endocytic pathway, mediating the lysosomal escaping of NPs and enhancing the translocation across the BBB. In this work, we synthesized gH625-functionalized PLGA-PEG-NPs (PELGA-NPs), never reported before in a BBB *in vitro* analysis. Because of their non-specific affinity to different cells, gH625-mediated brain delivery systems could show a non-specific distribution in the human body, after systemic administration. Receptor mediated transcytosis (RMT) is the most common strategies used by researchers to target the cerebral endothelium, since brain endothelial cells express different receptors. In the previous chapter, the ability of CRT peptide to specifically transport PELGA NPs across the *in vitro* BBB was demonstrated. CRT is a cyclic iron-mimicking peptide which may be used as the Receptor Mediated Transport (RMT)-targeting ligand [8]. Receptor transport caveolae-mediated pathway allows the specific transport of NPs to the CNS [9]. CRT binds to apo-Tf, causing it to adopt its iron-bound holo-Tf conformation, which recognizes TfR and gain access to the brain side. Therefore, in this work, to overcome the CPP lack of targeting specificity, we hypothesized that the coupling of gH625 to CRT on the surface of NPs may enhance NP transport across the murine cerebral endothelium (Fig. 1).

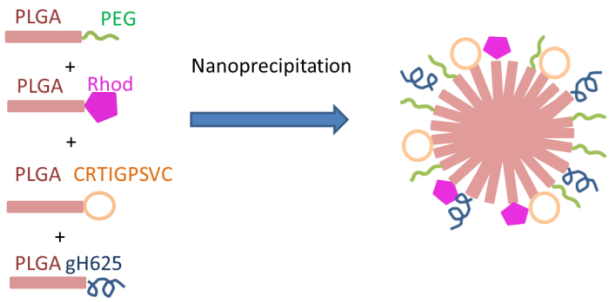

Figure 1: Schematic synthesis of dual-functionalized NPs with CRT and gH625 peptides for the active targeting and crossing of the cerebral endothelium.

Dual-functionalized NPs, with 3 different ratios of peptides gH/CRT: (i) 50% - 50% (i) 33% - 66% (iii) 66% - 33% have been synthesized and the effects of the functionalization on the penetration of PELGA NP through an *in vitro* BBB model based on bEnd.3, have been investigated. In order to study the contribution of both CRT and gH peptides in the trans-endothelial ability to cross the *in vitro* BBB, dual-functionalized NP formulations were compared to blank and mono-functionalized nanoparticles: CRT-NPs and gH-NPs. Reported here is that gH/CRT_33/66 NP promotes the targeting and crossing through an *in vitro* BBB under dynamic condition.

3.3 RESULTS AND DISCUSSION

3.3.1 NP characterization

To investigate the size and z-potential of NPs, dynamic light scattering (DLS) measurements, in aqueous medium were performed. The hydrodynamic size of NPs, after filtration, was found to be 88.24 ± 1.62 nm, 92.06 ± 1.53 nm, 84.53 ± 0.60 nm for blank, CRT-NP and gH-NP and 80 ± 1 nm, 78 ± 2 nm, 76 ± 1nm for gH/CRT_66/33, gH/CRT_50/50, gH/CRT_33/66 respectively, with polydispersity values of ca. 0.15, indicating a narrow distribution of the particle size used for all the experiments. Z-potential of 3 types NPs were almost the same: -27.40 ± 0.66 mV for blank NPs, -26.10 ± 1.17 mV for CRT-NPs, -13.83 ± 0.11 mV gH-NPs, -22.4 ± 0.5 mV for gH/CRT_66/33 , -23.8 ± 0.9 mV for gH/CRT_50/50 , -20.0 ± 0.5 mV for gH/CRT_33/66 (Table 1). A more positive charge was shown for gH-NPs and this is probably due to the positive charge of the amino-acid chain.

NP	Size [nm] ± SD	PDI	ζ Potential [mV] ± SD
Blank	88.24 ± 1.62	0.15	-27.40 ± 0.66
CRT	92.06 ± 1.53	0.15	-26.10 ± 1.17
gH625	84.53 ± 0.60	0.14	-13.83 ± 0.11
gH/CRT_66/33	84.09 ± 0.70	0.14	-21.97 ± 0.64
gH/CRT_50/50	77.76 ± 0.64	0.14	-20.53 ± 0.60
gH/CRT_33/66	76.72 ± 0.76	0.13	-20.00 ± 0.50

Table 1: Size and Zeta potential measurements of blank NPs and different NP functionalizations.

3.3.2 Co-localization studies

To further investigate the fate of NPs, the intracellular distribution of them by co-localization experiments within endocytic compartments, namely lysosomes, was followed. After 24h of incubation, samples were fixed with PF 4% for 10 min and observed by confocal microscope after lysosomes staining with LAMP-2. As shown, Fig. 2 blank, CRT-NPs, gH-NPs, gH/CRT_66/33, gH/CRT_50/50 and gH/CRT_33/66 NPs are internalized by the cells and they have different intracellular localizations. Blank NPs and CRT-NPs are distributed as spots mainly localized in the perinuclear region of the cell. Both blank and CRT-NPs partially co-localize with LAMP-2. Conversely, gH-NPs have a cytoplasmic distribution. No significant co-localization with lysosomes has been noticed for gH-NPs. On the other hand, localization of dual-functionalized NPs changes as a function of the formulation. Lysosomal distribution is linearly increasing with the CRT amount in the formulation, likewise, cytoplasmic distribution is linearly increasing with the gH amount, according with NP distribution of CRT and gH-NPs.

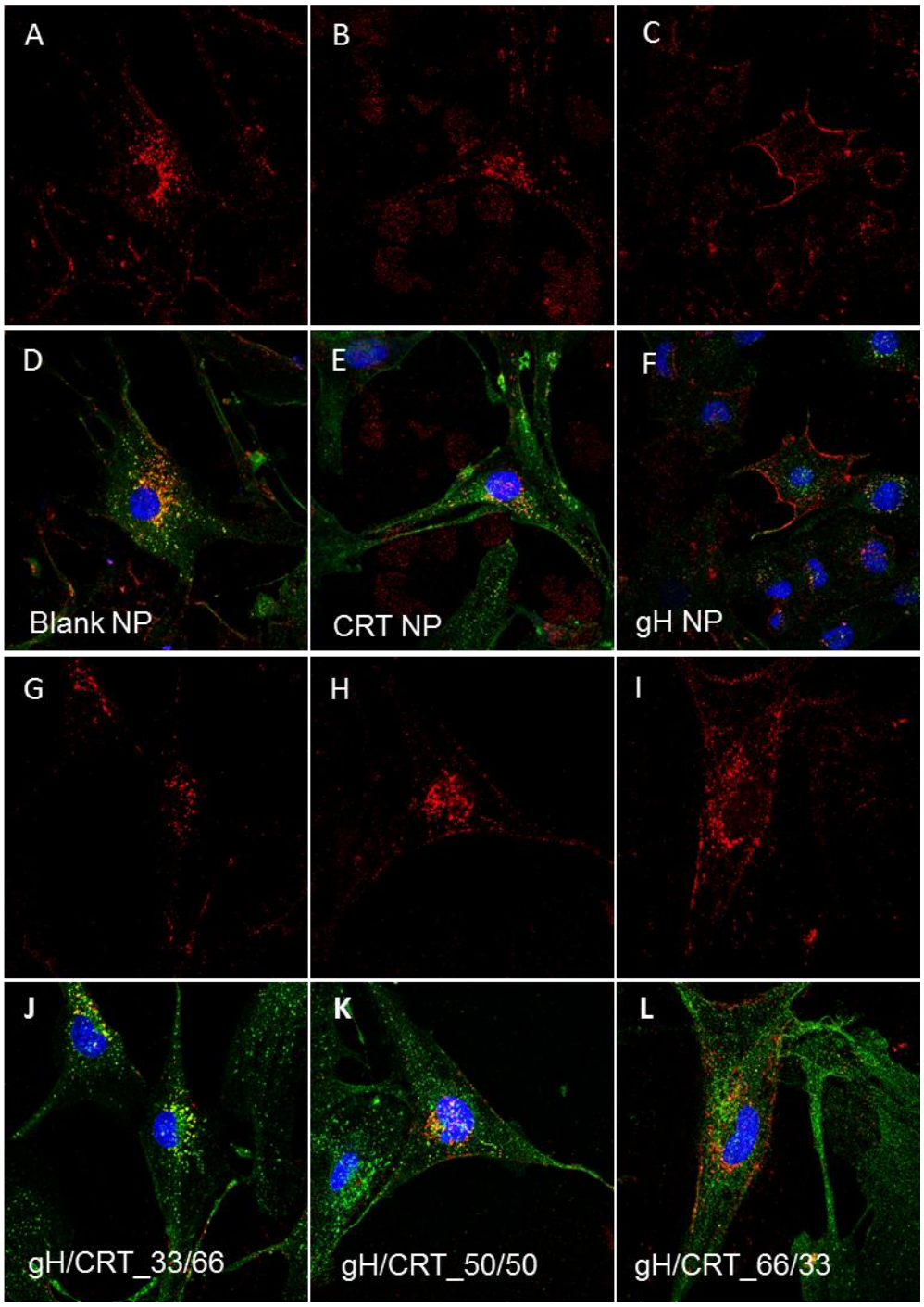

Figure 2: Colocalization of blank NPs (A,D); CRT-NPs (B,E); gH-NPs (C,F); gH/CRT_33/66 NPs (G,J); gH/CRT_50/50 NPs; (H,K); gH/CRT_66/33 NPs (I,L) with lysosomes after 24h incubation in bEnd.3 cells. Red: NPs; green: LAMP-2. Bar 50 µm.

3.3.3 NP transport across the BBB in static system

In order to study the contribution of both CRT and gH peptides in the trans-endothelial ability to cross the BBB, dual-functionalized NP formulations were compared to mono-functionalized NPs: CRT-NPs and gH-NPs. After 7 days of culture bEnd.3 cells were able to form a confluent cell layer, as described previously. Data reported in Fig. 3 show that CRT-NPs and gH/CRT_33/66 NPs cross more efficiently the endothelial layer compared to blank NP. In particular, among mono-functionalized NPs, CRT have the highest ability in NP transport across the *in vitro* BBB with a permeability of 4.64×10^{-6}cm/s. No significant permeability of NP was found for gH functionalization (3.60×10^{-6} cm/s) compared to blank NPs (3.17×10^{-6} cm/s); among bi-functionalized NPs gH/CRT_33/66 permeability was 7.48×10^{-6} cm/s; gH/CRT_50/50 NPs was 4.50×10^{-6} cm/s and for gH/CRT_66/33 was 3.50×10^{-6} cm/s. Data demonstrated that the increasing of CRT amount in dual functionalized NP formulation increases NP transport. Thus, gH/CRT_33/66 NPs have the highest of trans-endothelial crossing ability.

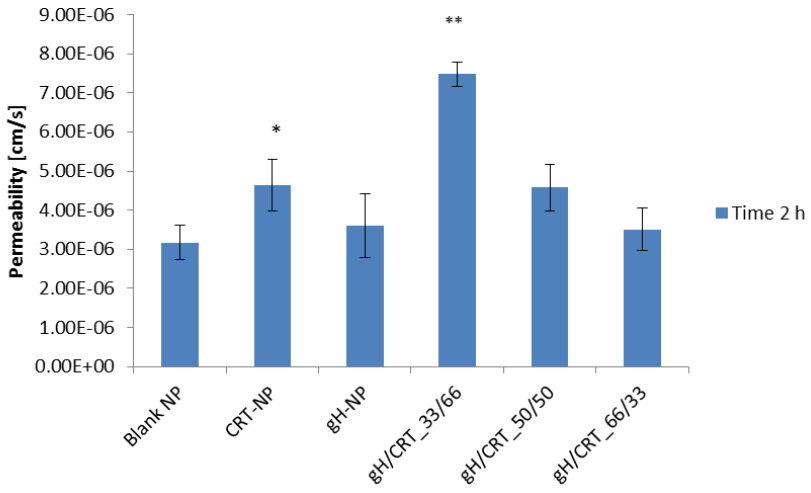

Figure 3: Permeability of bEnd.3 cell monolayer to blank, CRT, gH, gH/CRT_33/66, gH/CRT_50/50, gH/CRT_66/33 functionalized NPs.

3.3.4 Adhesion assay by using Glycotech system

In order to predict the *in vitro* targeting ability of the NPs to a cerebral endothelium under flow conditions, parallel plate flow chamber Glycotech assays were performed, as

described in the previous chapter. Among dual functionalized NP formulations, gH/CRT_33/66 NPs have the highest of trans-endothelial crossing ability and was chosen to assess whether these NPs could adhere to the BBB also under dynamic conditions. Confocal images for each NP type were acquired and analyzed by imageJ software. Fig. 4 compares the adhesion ability (Fig. 4A) and localization (Fig. 4 B) of blank NPs, CRT-NPs, gH-NPs and gH/CRT_33/66. Data are reported as the percentage of mean gray value. As shown, CRT-NPs and gH/CRT_33/66 NPs display the higher targeting ability at 10 µl/min flow rate (0.79 and 0.97 %, respectively) compared to blank NPs (0.44%). Percentage of mean gray value for gH-NP was found equal to 0.60%.

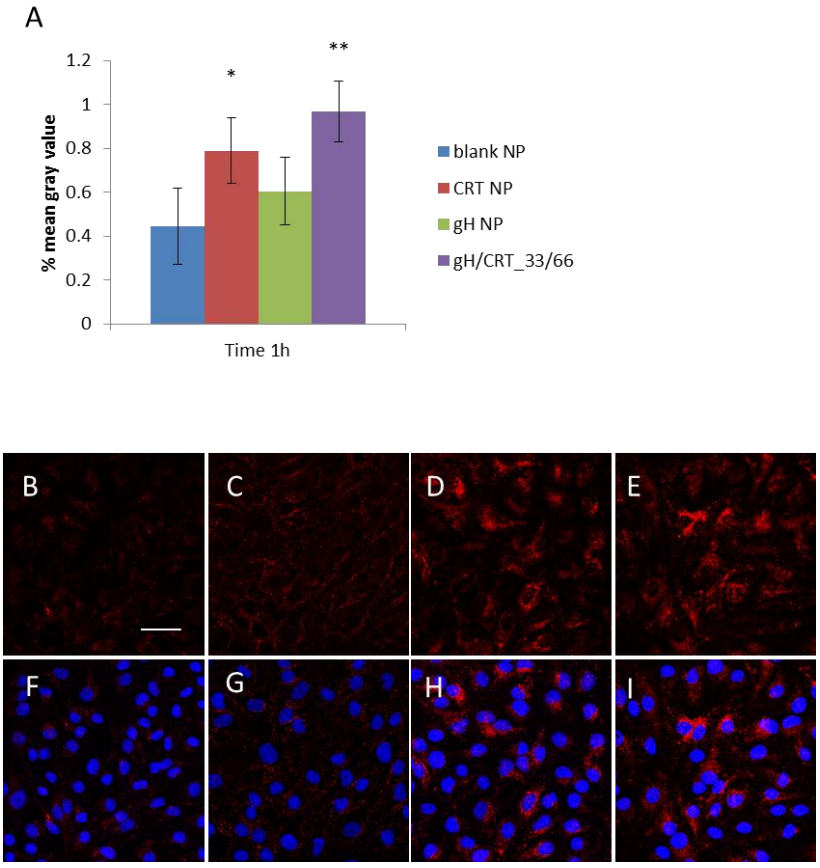

Figure 4: (A) NP adhesion ability to bEnd.3 under flow condition 10 ul/min. P *= <0.05; P **= <0.0005. (B-I) confocal images of NPs in bEnd.3 after the experiments. B,F blank NPs; C,G gH-NPs; D,H CRT-NPS; E,I gH/CRT_33/66. Red: NPs; blue: nuclei. Bar 50 µm.

3.4 MATERIALS AND METHODS

3.4.1 Synthesis of peptides

All the peptides were synthesized using standard solid-phase-9-fluorenyl methoxy carbonyl (Fmoc) method. The sequences are shown in Table X. gH 625 and CRT peptides were cleaved from resin by means of standard TFA/TIS/Water (95/2.5/2.5) solution and then precipitated in cold ethyl ether. Purified CRT and Ctrl peptides were obtain by RP-HPLC starting from 5/95 (v/v) acetonitrile (ACN)/water solution containing 0.1% v/v TFA. For gH625 peptide purification a 20/80 ACN/water solution 0.1% v/v TFA was used.

3.4.2 Synthesis of co-polymers

PLGA-peptides conjugate: The PLGA-Peptide conjugates were synthesized by a standard HBTU coupling procedure. Briefly, for CRT, PLGA (1 eq), HBTU (5 eq), OximaPure® (5 eq), DIPEA (10 eq) and Peptide (1.5 eq) were dissolved in anhydrous DMSO for 48h at room temperature. For gH625 peptide PLGA-NH2 (1 eq), HBTU (10 eq), OximaPure® (10 eq), DIPEA (20 eq), and Peptide (2 eq) were used. The adducts were purified from unreacted reagents using dialysis bags (MWCO 6-8 kDa) against pure water and lyophilized. The reaction products were verified by 1H-NMR spectroscopy.
Amino-PLGA, PELGA and Rhodamine-PLGA synthesis were described in the previous chapter.

3.4.3 NP synthesis and characterization

Functionalized-NPs were synthesized by nanoprecipitation method, according with the manufacturer's procedure described in the previous chapter. All copolymers of each type of NP were dissolved in 1.2 mL of acetone (Table 2**)** [10].

	Pelga (mg)	Plga-Rho (mg)	Plga-gH (mg)	Plga-CRT (mg)	Plga (mg)	mg tot
Blank NP	1	0.4	-	-	0.8	2.2
gH NP	1	0.4	0.4	-	0.4	2.2
CRT NP	1	0.4	-	0.4	0.4	2.2
gH/CRT_66/33	1	0.4	0.4	0.2	0.2	2.2
gH/CRT_50/50	1	0.4	0.4	0.4	-	2.2
gH/CRT_33/66	1	0.4	0.2	0.4	0.2	2.2

Table 2: Mass of copolymers of blank NP, gH-NP, CRT-NP, gH/CRT_66/33 NP, gH/CRT_50/50 NP, gH/CRT_33/66 NP

Mean size, size distribution and ζ-potential of NPs were determined by laser light scattering measurements (Zetasizer Nano ZS, Malvern Instruments, UK) on a 0.1 mg/mL suspension of NPs in water (Table 2).

3.4.4 Cell culture

Mouse cerebral endothelial cells, bEnd.3 cells (American Type Culture Collection, Manassas, VA) were grown in DMEM with 4.5 g/L glucose, 10% Foetal Bovine Serum (FBS), 3.7 g/L sodium bicarbonate, and 4 mM glutamine, 1% non-essential amminoacids, 100 U/mL penicillin and 0.1 mg/mL streptomycin in 100 mm diameter cell culture dish, in a humidified atmosphere at 37 °C and 5% CO_2. Cells used in all experiments were at passage 22–30.

3.4.5 Co-localization studies

Indirect immunofluorescence against endocytic markers may give information about the endocytic mechanisms underlying nanoparticle cellular uptake. The co-localization experiments are carried out on 70% confluent cells seeded on glass coverslips. All the reagents and solutions are prepared as described following. For co-localization experiments, with lysosomes, about 1×10^4 bEnd.3 were seeded on the round 12 mm-diameter glass coverslips placed in 24 well plates. Cells were incubated for 24 h with gH/CRT_33/66 NPs, gH/CRT_50/50 NPs; gH/CRT_66/33 NPs, bEnd.3 were firstly rinsed twice with PBS to remove non-internalized NPs and fixed with 400 µl of 4% paraformaldehyde at room for 10 min. For lysosomes staining, cells fixed were permeabilized with 0.05% saponin-PBS for 10 min and incubated with FBS-PBS 10% for 20 min at room temperature to block unspecific sites. Lysosomes were localized with rabbit 1:150 anti-LAMP-2 polyclonal (Abcam, 1mg/mL) primary antibody for 1 hour at room temperature in a humidified chamber and with 1:200 AlexaFluor 488 anti-rabbit secondary (1 µg/mL) antibody for 30 min. After mounted the coverslips on glass slides with PBS/glycerol (1:1) solution, immunofluorescence analyses were performed by means of confocal laser scanning microscope

3.4.6 Permeability assay to NPs in Transwell system

bEnd.3 were seeded at a density of 3×10^4 cells/cm^2 on Transwell permeable inserts (6.5mm diameter, 3 µm pores size; Corning Incorporated, Corning, NY). Permeability experiments were performed 7 days from the seeding, allowing sufficient time for the cells to develop the junctions between cells. On the day of experiment, Transwell insert filter

was washed with PBS, and then the media of the donor chamber was filled with 150 µL cell culture medium w/o phenol red containing 0.1 mg/mL of gH/CRT_33/66 NPs, gH/CRT_50/50 NPs; gH/CRT_66/33 NPs while the acceptor chamber was filled with 400 µL cell culture medium without phenol red. The samples of 400 µL were drawn every 30 min for 2 h from the acceptor chamber and were then replaced with the same amount of fresh medium. The fluorescence tracer concentration in the samples was determined by a spectrofluorometer (Victor, Wallac, PerkinElmer).

3.4.7 NP adhesion assay to BBB by using Glycotech system.

Glycotech assay was performed according to the manufacturer's procedure described in the previous chapter. The volumetric flow rate *Q* (10 µl/min) was fixed to be equal for all the experiments.

3.5 CONCLUSIONS

The aim of this work was to characterize the effect of functionalization of biodegradable nanoparticles with 2 synthetic peptides in enhancing targeting and transport across the cerebral endothelium. Sub-100nm PELGA NPs were successfully synthesized with 3 different ratios of CRT and gH peptides by using nanoprecipitation method. Results clearly indicate that NPs are internalized by the cells. NPs show different intracellular localization. Blank and CRT NPs have a lysosomal localization on the other hand, gH-NPs have a mainly cytoplasmic distribution. For bi-functionalized NPs, increasing the amount of gH in NP formulations decreases the lysosomal distribution, on the contrary, increasing the amount of CRT decreases the cytoplasmic signal. NP transport results demonstrated that CRT-NPs and gH/CRT_33/66 NPs have the higher transport ability compared to blank NPs. In particular, the permeability of the cerebral endothelium to gH/CRT_33/66 and CRT-NPs is about 2.5 and 1.5 times higher than blank NPs, respectively. Burdo et al. [11] demonstrated that iron is transported across endothelial cells both bound to Tf (holo-transferrin) and not bound to Tf (apo-transferrin). Several works reported that after endocytosis in brain endothelium, the complex Tf-TfR-iron is transported in coated vesicles to lysosomes, in which the presence of the iron chelating component desferrioxamine removes the iron from the complex. Then, the iron is transported across the membrane of the vesicle into the cytoplasm and is transcytosed, by still unclear mechanism. Fisher et al. [7] identified iron transport proteins such as ferritin for iron transcytosis, Mc Carthy et al. identified ferroportin [8]. On the other hand, apoTf-receptor complex is sorted into recycling endosomes to the blood on the luminal membrane [14,15]. Then, co-localization

studies according with NP transport results, suggest that after the internalization, the complex CRT iron mimicking peptide-Tf-TfR is transported to lysosomes at pH 5-5.5 and CRT-NP from Tf/TfR is removed. Then, CRT-NP is transported into the basal compartment separately. On the contrary, the cytoplasmic distribution of gH-NPs is probably due to the working mechanism of gH peptide that promotes lipid membrane-reorganizing processes, through fusion involving temporary destabilization and subsequent reorganization of the membrane [6]. However, no significant crossing ability was observed when gH625 is exposed on PELGA NP. Probably when gH-NPs are synthesized, peptide does not assume the correct conformation, then gH625 is able to recognize lipid membrane of cells but does not exert its activity. To further investigate the NP targeting ability under flow condition, Glycotech system assays were performed. In order to obtain a mean velocity comparable with the blood velocity in human capillaries, the experiments were carried out using a flow rate of 10 µl/min. Data reported as the percentage of mean gray value indicates that gH/CRT_33/66 formulation has the highest targeting ability to the BBB under flow conditions. More precisely the percentage of gH/CRT_33/66 and CRT-NPs is about 2.2 and 1.8 times higher than blank NPs, respectively, according to previous results of NP transport. No significant adhesion ability was found for gH-NPs and this can be ascribed to the lacks of specificity to the BBB of gH.

Taken all together these findings indicates that for dual functionalized NPs, a cooperative effect of gH and CRT peptides when exposed on NP in percentage 33%/66%, respectively was demonstrated. Probably peptides in gH/CRT_33/66 NP formulation are able to assume the correct conformation and to exert their activity, promoting NP transport across the BBB in a synergic manner. The new nanocarrier, made up of FDA-approved materials, could be regarded as a promising strategy for administration of therapeutical compounds to the brain.

3.6 REFERENCES

1. **Falanga A. P.** et al. Synergic effect of double functionalization with peptides in promoting NP transport across the cerebral endothelium *(to be submitted).*

2. Zheng, C., Ma, C., Bai, E., Yang, K. & Xu, R. Liposome for Targeted Drug Delivery To Glioma. **8,** 1658–1668 (2015).

3. Salvati, E. *et al.* Liposomes functionalized to overcome the blood-brain barrier and to target amyloid-β peptide: The chemical design affects the permeability across an in vitro model. *Int. J. Nanomedicine* **8,** 1749–1758 (2013).

4. Guarnieri, D. *et al.* Shuttle-Mediated Nanoparticle Delivery to the Blood-Brain Barrier. *Small* **9,** 853–862 (2013).

5. Guarnieri, D. *et al.* Surface decoration with gH625-membranotropic peptides as a method to escape the endo-lysosomal compartment and reduce nanoparticle toxicity. *Nanotechnology* **26,** 415101 (2015).

6. Galdiero, S. *et al.* Peptides containing membrane-interacting motifs inhibit herpes simplex virus type 1 infectivity. *Peptides* **29,** 1461–1471 (2008).

7. Galdiero, S. *et al.* Intracellular delivery: exploiting viral membranotropic peptides. *Curr. Drug Metab.* **13,** 93–104 (2012).

8. Staquicini, F. I. *et al.* Systemic combinatorial peptide selection yields a non-canonical iron-mimicry mechanism for targeting tumors in a mouse model of human glioblastoma. *J. Clin. Invest.* **121,** 161–173 (2011).

9. Pardridge, W. M. Drug transport across the blood-brain barrier. *J. Cereb. Blood Flow Metab.* **32,** 1959–72 (2012).

10. Cantisani, M. *et al.* Biocompatible nanoparticles sensing the matrix metallo-proteinase 2 for the on-demand release of anticancer drugs in 3D tumor spheroids. *Colloids Surfaces B Biointerfaces* **135,** 707–716 (2015).

11. Burdo, J. R., Antonetti, D. A., Wolpert, E. B. & Connor, J. R. Mechanisms and regulation of transferrin and iron transport in a model blood-brain barrier system. *Neuroscience* **121,** 883–890 (2003).

12. Fisher, J. *et al.* Ferritin: a novel mechanism for delivery of iron to the brain and

other organs. *Am J Physiol Cell Physiol* **293,** C641–9 (2007).

13. McCarthy, R. C. & Kosman, D. J. Ferroportin and exocytoplasmic ferroxidase activity are required for brain microvascular endothelial cell iron efflux. *J. Biol. Chem.* **288,** 17932–17940 (2013).

14. Dautry-Varsat, A., Ciechanover, A. & Lodish, H. F. pH and the recycling of transferrin during receptor-mediated endocytosis. *Proc. Natl. Acad. Sci.* **80,** 2258–2262 (1983).

15. Roberts, R. L., Fine, R. E. & Sandra, a. Receptor-mediated endocytosis of transferrin at the blood-brain barrier. *J. Cell Sci.* **104 (Pt 2,** 521–532 (1993).

4 CHAPTER 5

Microchannel mimicking microvascular capillary: a low cost platform for endothelial cell culture.

4.1 ABSTRACT

In order to mimic closely *in vivo* microvasculature we developed circular microchannels for endothelial cell growth. However, nowadays, a simple, low cost, and versatile method to fabricate circular microchannels is still missing. Here, we report on a fast, inexpensive, flexible and reproducible method to fabricate circular microchannels by coupling spin coating with micromilled square microchannels. The proposed method is based on the balance between the displacement of liquid PDMS induced by centrifugal forces and the surface tension that tends to keep the liquid accumulated especially in the corners, which become therefore rounded. To show the versatility of the described experimental study we prepared a variety of rounded microchannels, including branched and PMMA-PDMS hybrid configuration microchannels. Finally, an endothelial cell layer was formed by culturing brain endothelial bEnd.3 cells inside the proposed circular microchannels. Results demonstrated a more successful adhesion, growth, and homogeneous distribution of the cells along the circular microchannel than those observed in the square microchannel used as a control (Vecchione et al., 2016).

4.2 INTRODUCTION

Microfluidics is a micro-technological field that deals with the handling of fluids and dispersions of nano and micro-objects (Andersson and van den Berg, 2003; Valencia et al., 2012; Whitesides, 2006). Interestingly, microfluidics provides important advantages over classical systems for cell and tissue cultures by displaying microchannels and structures that can mimic the physiological parameters of *in vivo* models (Haeberle and Zengerle, 2007; Ziolkowska et al., 2011). Many researchers use circular microchannels with endothelial cells to replicate cardiovascular flow conditions in *in vitro* models (Borenstein

et al., 2010; Choi et al., 2013; Hochmuth, 2000; Lee, 2000). The advantage of circular microchannels over square microchannels in mimicking blood vessels for endothelial cell culture has also been recently demonstrated by an MIT research group that developed a rapid casting of patterned vascular networks for perfusable engineered three-dimensional tissues (Miller et al., 2012). The use of circular microchannels reduces the flow stagnation phenomenon present at the edges of square microchannels due to the symmetrical duct velocity profiles (Huang et al., 2012). Conversely, endothelial cells grown on the bottom of a square microchannel are subjected to a varying shear stress that influences their elongation, differentiation, and growth. (Seo et al., 2004). Together with the strong use in microvascular capillary field, the use of circular microchannels is convenient in the preparation of cylindrical or round microparticles, as well as circular fibers and cell-laden hydrogels (Chung et al., 2012; Dendukuri et al., 2007; Dendukuri et al., 2006) and to control microparticle migration (D'Avino et al., 2012; Romeo et al., 2013). Recently, open microchannels have also been used for cell growth or to flux fluids by capillary effect without using pump systems (Faid et al., 2005; Sia and Whitesides, 2003). Both applications may benefit from a circular microchannel shape as in the case of closed microchannels.

Various methods to fabricate polymeric microchannels have been reported depending on the end goal of industrial mass production or rapid prototyping at the research laboratory level, including photolithography coupled with wet etching, reactive ion etching, stamp based techniques, such as soft lithography, hot embossing and injection molding, as well as ablating technologies like conventional machining, laser ablation and finally direct 3D printing (Fiorini and Chiu, 2005; Kim et al., 2008; Whitesides et al., 2001; Wu and Gu, 2011; Zhao et al., 1997). Direct 3D printing can easily produce rounded microchannels, but with some limitations in the resolution, while more complex techniques -such as wet etching or reactive ion etching- can be tuned to produce rounded and smaller microchannels (Camp et al., 2008). During the last decade several research groups have developed new techniques for the fabrication of circular microchannels. For example, recently Abdelgawad et al. presented an innovative approach to fabricate circular microchannels from square geometry using a pressurized air stream inside PDMS-filled microchannels. This technique lacks the ability to create branches, while curved structures and long circular channels may be not uniform (Abdelgawad et al., 2011). Alternatively, mechanical micromachining techniques, such as micromilling, proved to be an effective approach to fabricate complex 3D micro-scale features on metals and polymers (Chen et al., 2014; Dornfeld et al., 2006). However, microchannels obtained by micromilling technology exhibit a high roughness

profile (Ogilvie et al., 2010), while in many applications a very smooth surface is required (Hetsroni et al., 2005; Zhang et al., 2013). Recently, by exploiting the surface tension phenomenon, it has been demonstrated that microlenses can be obtained by spinning liquid PDMS on square microstructures, fabricated by photolithography (Lee et al., 2007; Shih et al., 2006). In 2012, De Ville and co-workers used the surface tension of alginic acid sodium salt solution inside square microchannels, so that such liquid creates rounded protrusions (De Ville et al., 2012); it is a simple and low-cost method for the fabrication of round PDMS microfluidic channels but it lacks the capability to easily tune curvature; no circular microchannels could in fact be obtained. To the best of our knowledge, an easy, low cost and versatile method to fabricate circular microchannels is therefore still missing. In this paper, we present an innovative fabrication method that combines spin coating and micromilled square microchannels to fabricate circular microchannels ensuring easy and low cost manufacturing that can be applied without the need for clean room facilities. In this process centrifugal forces and surface tension cause together the localization of the liquid PDMS in the corners of the channel providing the desired curvature. We demonstrate that -by tuning parameters such as viscosity, geometry of the starting square channel, spin coating speed- it is possible to obtain circular and, more in general, round-shape and closed microchannels. The geometry and quality of the semi-circular PDMS channels created by spin coating technology was characterized using optical microscopy, scanning electron microscopy (SEM) and a surface profilometer, while AFM was used to characterize channel roughness. The versatility of this method was further demonstrated by proving the possibility to produce hybrid solutions and rounded microchannels different from circular ones. Finally, preliminary experiments on brain endothelial bEnd.3 cells indicate the capability of the circular microchannels to allow a good adhesion, an improved growth and a more homogeneous distribution of the cells over the surface of the channel than those obtained with the square microchannel of comparable size used as a control.

4.3 RESULTS AND DISCUSSION

Motivated by the strong need in the microfluidic fields for circular microchannels, we propose an innovative hybrid technique that combines mechanical micromachining and spin coating process which is easy, reproducible and cost-effective. The process used to fabricate semi-circular microchannels is schematically outlined in Fig. 1.

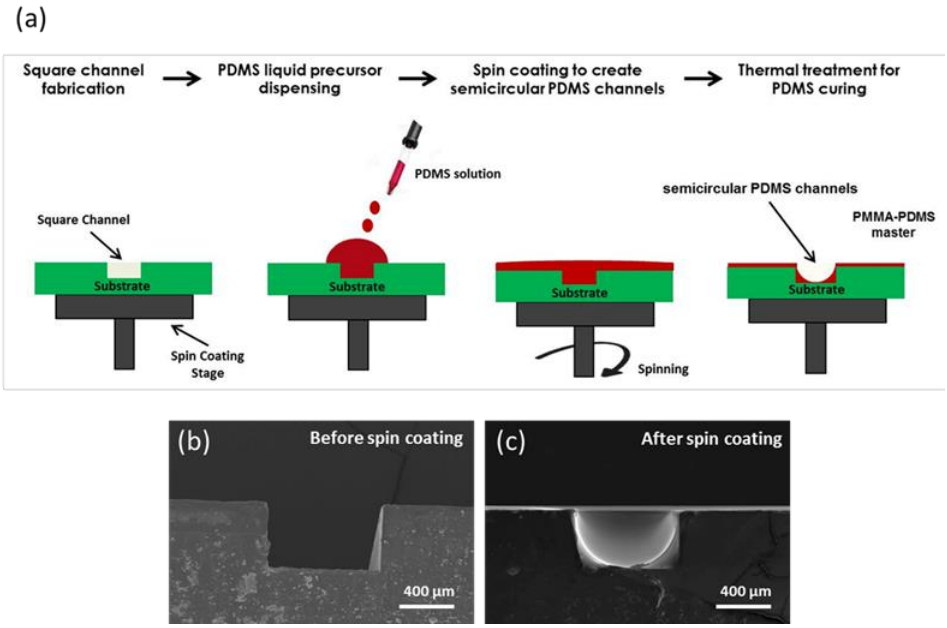

Figure 1: Scheme of the spin coating process (a). Picture of a 800 x 400 µm PMMA microchannel before and after spin coating, respectively (b and c). The PDMS adhering to the microchannel wall after spin coating and consolidation by thermal curing.

In particular, a mixture of PDMS precursor and curing agent is dispensed on the square microchannel obtained by micromilling followed by the spin coating process. The deposited liquid layer under spin coating is able to form a stable rounded PDMS layer on the walls of the square microchannel. Such rounded microchannel can be consolidated by curing the PDMS. Using undiluted PDMS solution, a PDMS circular shape in the square microchannel 800 x 400 µm was observed at around 2000 rpm and 20 s. In particular, Fig. 1c displays the PDMS adhering to the microchannel wall after spin coating and thermal curing. Undiluted PDMS proved too viscous to obtain a circular section in the case of narrower microchannels, independently of the spinning conditions; we used a mixture of PDMS and hexane at a ratio optimized according to each microchannel size in order to lower viscosity. Table 1 reports the degrees of dilutions capable to provide circular shapes at 2000 rpm and 20 s of spin coating in the differently sized microchannels and the corresponding viscosities.

Solution	Viscosity Pa s	Channel diameter µm
Undiluted PDMS	5.86	800
3:1 PDMS : Hexane	0.225	400
1:1 PDMS : Hexane	0.043	200
1:3 PDMS : Hexane	0.0057	50-100

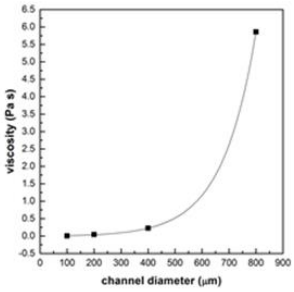

Table 1: Viscosity of the different PDMS solutions and corresponding circular microchannel diameters, measured using a Modular Compact Rheometer (Anton Paar).

In particular, the smaller the microchannels, the lower the viscosity used. From this table and related graph, it is possible to appreciate that reducing the size of the microchannels, dilution is less and less influent such that a semi-circular microchannel of 50 µm could be obtained with the same degree of dilution as the 100 µm microchannel. All the semi-circular shapes observed by SEM are summarized in Fig. 2.

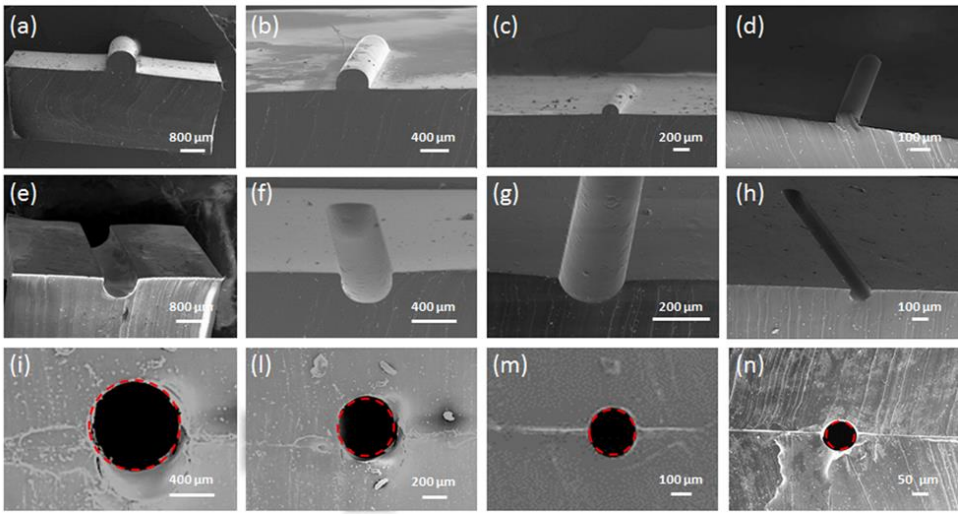

Figure 2: SEM images of semi-circular PDMS positive relief replicas (a-d), the corresponding semi-circular PDMS microchannels (e-h) and cross-section of bonded circular microchannels (i-n). The microchannels have diameters of 800, 400, 200 and 100 µm, respectively.

From the SEM micrographs it is possible to note the possibility to scale down the method in terms of microchannel size to around 50 µm. Circular shapes are evident from the SEM cross-section of closed microchannels (Fig. 2 i-n). In order to better characterize the uniformity of the microchannels along their extension and the reproducibility of the process, PDMS replicas made directly from the PMMA-PDMS masters (800/400 µm width/depth) were measured by using a profilometer (figure S1 and S2 in Supplementary Data). For the profilometer characterization we used a map scan type on hills profile, a stylus type radius of 2.5 µm and a measurement range of 525 µm. Other studies have investigated the use of spin coating technology to fabricate ultrathin and hyperelastic PDMS nano-membranes with various thicknesses and sizes by using PDMS diluted with hexane (Thangawng et al., 2007). Herein, for the first time we have applied the thinning property of the PDMS-hexane mixture for scaling down, below 800 µm, the manufacturing of circular microchannels starting from cost-effective square PMMA microchannels. Circular microchannels can also be fabricated by micromachining a substrate with tapered angle ball tips. We made a comparison between surfaces obtained with our method and with direct channel fabrication by micromilling. From the optical microscope images (Fig.

3a,b) it was possible to observe the absence of the engraving line in the case of the mold prepared with our method with an increase of the transparency. Moreover, roughness profiles were characterized by AFM showing an enhancement of the smoothness since it was ~228 nm compared to ~6 nm (Fig. S3).

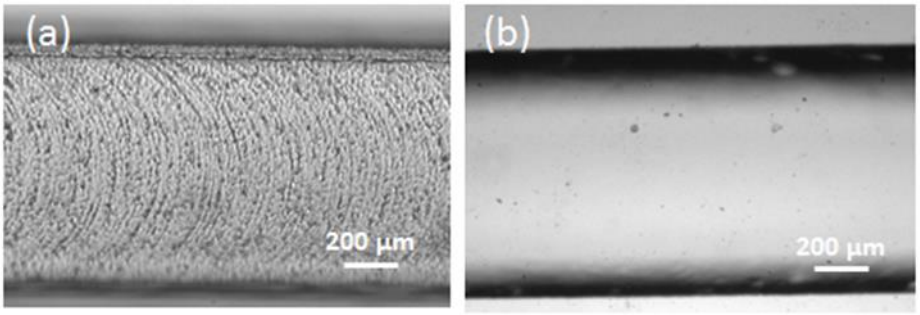

Figure 3: A bright field microscopy image of semi-circular PDMS microchannels, replicated directly from a micromilled round microchannel (a) and from a semi-circular microchannel obtained using the proposed method (b).

This huge reduction in terms of roughness is highly desirable in microfluidics as previously mentioned and it is also advantageous from an optical standpoint since the final microchannel results much more transparent and internally inspectable.

To produce closed microchannels, after fabricating the two symmetric semi-circular microchannels we treated their surface by oxygen plasma so that they could irreversibly be bonded after alignment (Fig. 2i-2n). They are examples of closed microchannels of very different sizes ranging from 800 to 100 µm. For the small microchannels the alignment was carried out by using motorized stages coupled with an optical camera (Fig. S3). As anticipated in the introduction, our method can also allow the fabrication of a hybrid PMMA-PDMS device where two symmetric PMMA-PDMS semi-circular microchannels obtained after PDMS spin coating on square microchannels in PMMA can be directly

bonded, instead of acting as masters. In this case, by using small magnets embedded into the PMMA substrates it is possible to easily align even the smallest microchannels (down to 50 µm) -as shown in Fig. 4a- avoiding motorized stages.

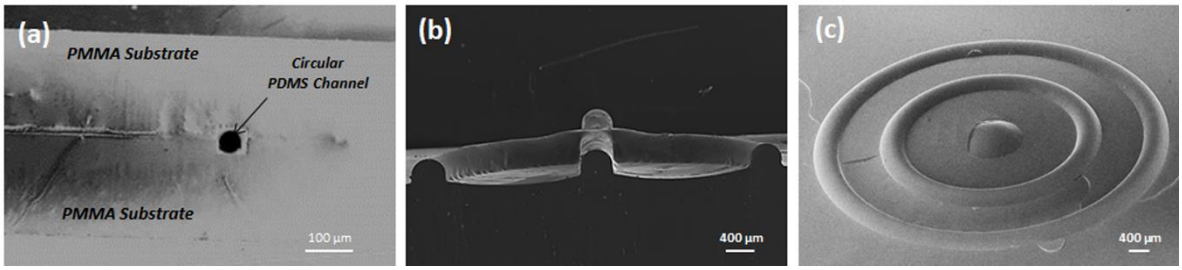

Figure 4: A hybrid modular device made of PMMA and PDMS with neodymium magnets, a microchannel section SEM image (a). Branched and curved semi-circular PDMS microchannels, emulating arterioles and venules (b). A ring-shape microchannel obtained from a square geometry (c).

With a hybrid device it is possible to combine the rigidity of the PMMA useful in the handling of the device -for example during the alignment step- with the softness and the low roughness of the spin coated PDMS. In addition, the PDMS layer in the case of magnetic bonding provides a strong sealing making temporary bonding with no leakage (Supplementary data in Fig. S5 a)

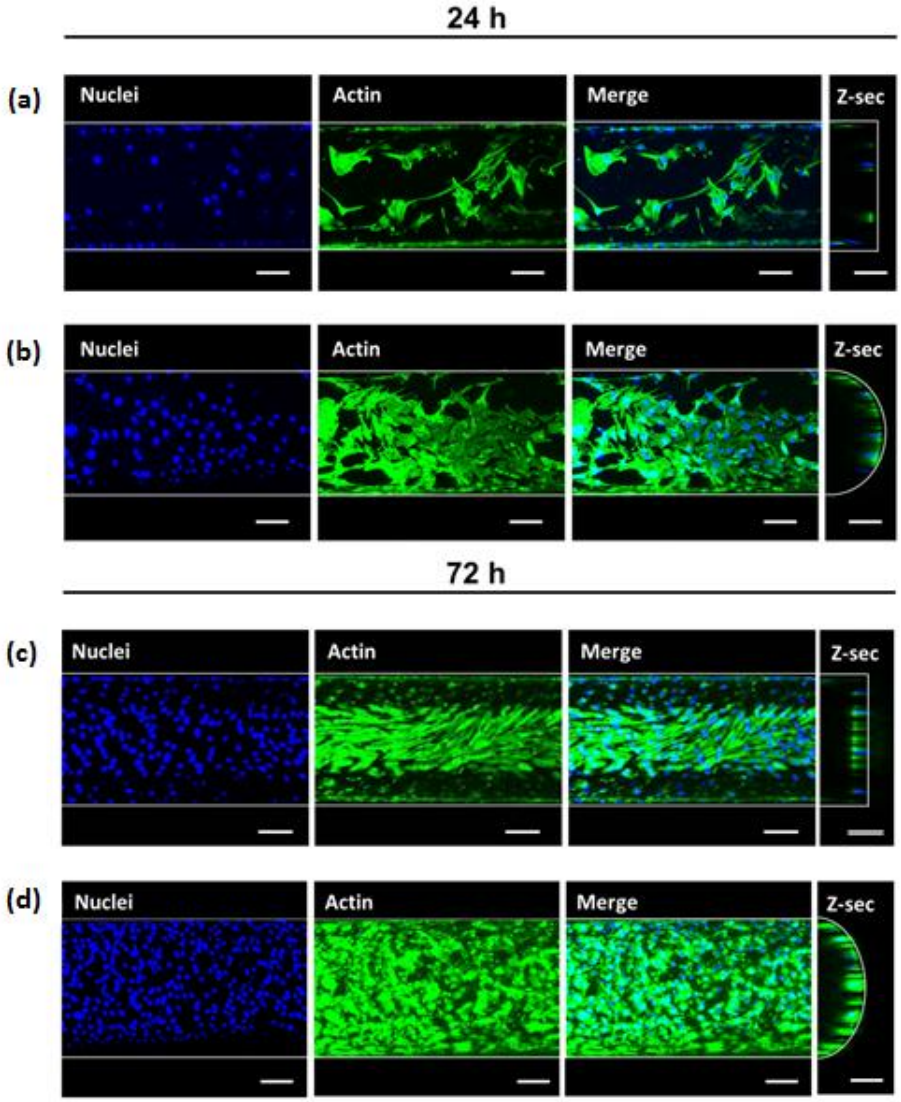

Figure 5: bEnd.3 cell growth in square (a and c) and circular (b and d) microchannels (width: 400 µm) after 24 (a and b) and 72 (c and d) hours. Blue represents cell nuclei stained with DAPI. Green represents actin microfilaments stained with 488Alexa-phalloidin. Merge is the overlapping of the blue and green channels. Z-sec is the projection along z-axis of confocal z-sectioning images (z-slice thickness = 1.28 µm, number of slices = 162). Scale bar 100 µm.

PDMS is also useful as an optimal interface for cell cultures. A recently proposed method to fabricate circular microchannels is based on the use of compressed air injected in a square microchannel filled with PDMS precursor. Despite the advantage to avoid any alignment, air pressurized technology cannot be applied to branched microchannels. Moreover, the gradient pressure inside the microchannel may prevent a uniform thickness of the PDMS around the wall, especially in the case of microchannels curved in plane. Our technique, instead, allows preparing branched microchannels as shown in Fig. 4b, useful to emulate arterioles and venules with the same principle of single microchannels and microchannels curved in plane as shown with ring-shape microchannels in Fig. 4c and S5 b. In addition, with the proposed method all the structures can be inspected before bonding thanks to the starting open microchannels and the vertical curvature of the final microchannel can be tuned. In particular, as described in the experimental section, to obtain semi-circular shapes we used in all cases a width twice long as the depth of the square microchannel, while to tune the curvature of the final microchannel we were able to vary the depth of the square microchannel (Fig. S6). Another recent work is based on the filling of square microchannels exploiting surface tension, which creates protruding round liquid to be replicated after consolidation. Although it does not involve expensive equipment for the fabrication, it is limited in the tuning of the curvature and in the production of discrete microchannels because of filling issues; therefore, circular microchannels were not obtained. In terms of flexibility other parameters that can be exploited with our method for the tuning of the curvature are viscosity (especially in the case of large widths) and spin coating speed.

Moreover, we preliminarily tested the potential applicability of the as-prepared circular microchannels to sustain growth and formation of a confluent endothelium *in vitro*. To this aim, brain endothelial bEnd.3 cells were seeded inside a 400 µm-diameter circular microchannel and cultured for 24 and 72 h. We chose to work with brain endothelial cells as a model of endothelial tissue and, in particular, of the blood brain barrier that currently represents one of the main goals of many therapeutic strategies and biomedical applications (Guarnieri et al., 2013; Kreuter, 2001). As shown in Fig. 5, bEnd.3 cells were able to adhere and grow into the circular microchannels. In particular, after 72 h of culture, cells formed a confluent and very homogeneous monolayer that resembled the endothelial tissue. Conversely, when cultured into a 400 µm wide square microchannel, cell adhesion, spreading and proliferation were less efficient. More interestingly, the distribution of the cells along the square microchannel was not homogeneous. In particular, we observed a high cell adhesion in the middle of the channel and a poor adhesion in the corners. These

observations were more evident at a longer culture time (72 h) and were in agreement with previously reported results (Farcas et al., 2009; Jang et al., 2015). We quantified the cell density over time in both microchannel shapes. As shown in Fig 6, this analysis shows a higher cell number per mm^2 in the circular microchannel compared to the square microchannel.

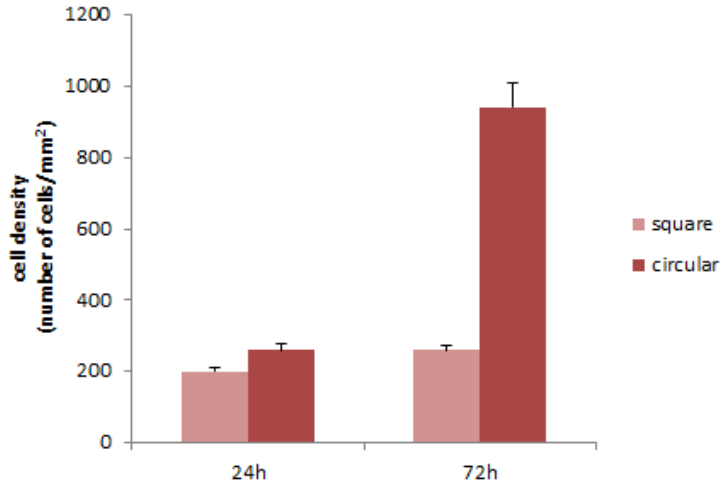

Figure 6: Analysis of cell density in the square and circular microchannels at 24 and 72 h of culture by Image J software.

Taken altogether, these data demonstrate the advantage of our circular microchannels in culturing endothelial cells compared to channels with squared geometry and their potential use as scaffolds able to promote the formation of brain capillary-like structures.

4.4 MATERIALS AND METHODS

The poly(methyl methacrylate) PMMA substrates used in this study, thickness 1.2 mm, were purchased from Goodfellow Cambridge Ltd, (UK) and belong to the same batch of supplied PMMA substrates. PMMA offers several material properties including optical transparency, low cost, inexpensive manufacturability, possibility of chemical treatment and biocompatibility. A PDMS prepolymer and a curing agent (Sylgard 184 elastomer kit) were purchased from Dow Corning Corporation (USA). Hexane puriss. p.a. was obtained from Sigma-Aldrich, (USA). The microtools used in the microfabrication process were 5 tr series 2 flute micro square end mills with different diameters: 800, 400, 200, 100 and 50 µm and 1 tr series 2 flute micro ball end mill with a diameter of 800 µm;

they were purchased from Performance Micro tool (USA). Micromilling machine was purchased from Minitech Machinery Corporation (USA). Syringe pump 11 Helite Series was purchased from Harvard apparatus (USA). Fabricated microchannels were inspected by electron scanning microscopy (SEM) (Ultraplus Zeiss) and profilometer (Veeco Dektat 150). For the spin coating process, a spin coater from Laurell (WS-650 Series) was used. Mouse cerebral endothelial cells, bEnd.3 cells, were purchased from American Type Culture Collection, Manassas, VA. Dulbecco's Modified Eagle's Medium (DMEM) with high glucose, trypsin, Dulbecco's phosphate-buffered saline (DPBS), fetal bovine serum (FBS), penicillin and streptomycin were purchased from Gibco Invitrogen, USA. Sodium pyruvate and DAPI were purchased from Sigma-Aldrich, (USA). Glutamine was purchased from Lonza Group Ltd,Basel, Switzerland. Non-essential amino acids were purchased from EuroClone S.p.A., Milano, Italia. Red fluorescent WGA and Alexa488-phalloidin were from Gibco Invitrogen, USA.

4.4.1 Square microchannels fabrication

The square microchannels were typically fabricated by sequentially micromachining PMMA layers by using the above mentioned micromilling machine. Milling is a subtractive microfabricating process that uses rotating cutting tools to remove material from a substrate (Chen et al., 2014; Dornfeld et al., 2006; Guckenberger et al., 2015). To standardize the fabrication process of semi-circular microchannels from square geometry, we micromilled microchannels with different width-depth: 800-400, 400-200, 200-100, 100-50 and 50-25 µm. Different ratios of width-depth, such as 800-300 and 400-100 µm, were also used to show capability of tuning the curvature of the final rounded microchannels. Moreover, to show the versatility of this method -by using a 400 µm end mill- we micromilled microchannels with branches that emulate arterioles and venules, as well as ring-shape microchannels. To design a draft of the microstructures we created a layout by Draftsight (Cad Software). During micromilling, spindle speed, feed speed and plunge rate per pass were set to 10 000 rpm, 15 mm s^{-1}, and 20, respectively.

4.4.2 Spin coating and fabrication of circular PDMS microchannels

Spin coating is a common technology for the production of polymer films of controlled and uniform thickness (Koschwanez et al., 2009; Mata et al., 2005). To create semi-circular microchannels of different diameters from square microchannels we used the above mentioned spin coater. A typical process involved depositing a small PDMS droplet, mixed in ratio 10:1 with curing agent, (around 1 ml) at different degrees of dilution with hexane onto the center of a substrate and then spinning at high speed (2000 rpm for 20 s). PDMS precursor was previously exposed to vacuum to eliminate air bubbles for at least 30 min. The PMMA-PDMS with round open microchannels was baked in the oven (1 h, 75 °C), to finalize the PDMS curing process. PDMS solution was poured on the hybrid PMMA-PDMS master and cured at 80 °C for 2 h. Particularly, in order to prevent adhesion of the PDMS replicas on the master, this was treated with oxygen plasma to activate the surface using a plasma chamber (Plasma prep II, SPI) for 1 min at a pressure of 0.3 mbar and power of 37 W, immersed for about 2 min into a silane solution (i.e., a mixture of 94% v/v isopropanol (Sigma Aldrich), 1% acetic acid (Sigma Aldrich), 1% Fluorolink S10 (Solvay), and 4% deionized water and then placed in an oven at 75 °C for 1 h, thus allowing a complete reaction of the master surface with the fluorinated polymer (Occhipinti, 2010). After curing, the PDMS was peeled off from the PMMA-PDMS master. The entire procedure was repeated to prepare final PDMS open microchannels (Brittain et al., 1998; Xia and Whitesides, 1998). In the case of closed microchannels, two symmetric semi-circular microchannels were optically aligned and bonded through oxygen plasma activation of the surface. For the very small microchannels the alignment was aided by the use of two parallel motorized stages coupled with an optical camera. Temporary bonding was also carried out by using magnets with the advantage of obtaining high precision alignment avoiding motorized stages and the possibility to reopen closed microchannels after use.

4.4.3 Brain endothelial cell seeding and growth within square and circular microchannels

The fabricated open microchannels (400/200 μm width-depth), were bonded to a glass slide through oxygen plasma activation; closed microchannels were sterilized with 10 % penicillin-streptomycin solution in PBS before cell seeding for 24 h at 4 °C to prevent contamination. Both square and circular microchannels were coated with 10 μg/ml fibronectin (Sigma-Aldrich) for 1 h at 37 °C. Afterwards, the microchannels were washed with PBS to remove fibronectin excess. bEnd.3 cell suspension, at a density of 6×10^5 cells/ml, were injected into the channels. After incubation for 20 min in a 5 % humidified CO_2 incubator at 37 °C for cell attachment, bEnd.3 were reseeded within microchannels and incubated again, rotating the devices by 90° as previously described. (Farcas et al., 2009; Jang et al., 2015) This step was repeated three more times to cover the entire surface of the circular and square microchannels. Then, cells were allowed to grow for 24 and 72 h within the channels. At these time points, cells were fixed with paraformaldehyde 4% for 10 min and actin microfilaments and nuclei were stained with Alexa488-phalloidin (Molecular Probes) and DAPI (Sigma). Samples were observed and images were acquired by multiphoton confocal microscope (Leica TCS SP5 MP) equipped with a 20 × dry objective. Z-sectioning images were acquired with 1.28 μm z-slice thickness. Cell density was calculated normalizing the number of nuclei for the area of the channels by Image J analysis software.

4.5 CONCLUSIONS

We developed a fast and reproducible method to fabricate polymeric circular microchannels from micromilled square microchannels coupling a spin coating technology. In particular, a PMDS precursor was deposited by spin coating on the square microchannels and formed a circular shape thanks to surface tension, which smoothed the corners. This PMMA-PDMS master was then used to prepare final semi-circular microchannels by double replica of PDMS, which can be aligned and bonded when closed microchannels are required. This process was useful in making small circular microchannels (down to 50 μm) and it also showed to be effective in creating microchannels with a branched and a ring-shape

geometry. Therefore, we propose a reproducible, versatile, and low cost method to produce open or closed circular microchannels for *in vitro* vascular microcapillaries that is also useful for other applications such as plug production and microparticle alignment. As a proof of the advantage of producing circular rather than square microchannels, we cultured cells in both devices and verified how the presence of corners negatively affects the growth and uniformity of an endothelial cell layer. Results support the conclusion that cylindrical microchannels are more appropriate for cell growth, particularly when an *in vivo* system needs to be mimiched *in vitro*.

4.6 REFERENCES

1. R. Vecchione, G. Pitingolo, D. Guarnieri, **A. P. Falanga** and P. A.Netti, *Biofabrication*, 2016. *Under review.*

2. Abdelgawad, M., C. Wu, W. Y. Chien, W. R. Geddie, M. A. S. Jewett, and Y. Sun, 2011, A fast and simple method to fabricate circular microchannels in polydimethylsiloxane (PDMS): Lab on a Chip, v. 11, p. 545-551.

3. Andersson, H., and A. van den Berg, 2003, Microfluidic devices for cellomics: a review: Sensors and Actuators B-Chemical, v. 92, p. 315-325.

4. Borenstein, J. T., M. M. Tupper, P. J. Mack, E. J. Weinberg, A. S. Khalil, J. Hsiao, and G. Garcia-Cardena, 2010, Functional endothelialized microvascular networks with circular cross-sections in a tissue culture substrate: Biomedical Microdevices, v. 12, p. 71-79.

5. Brittain, S., K. Paul, X. M. Zhao, and G. Whitesides, 1998, Soft lithography and microfabrication: Physics World, v. 11, p. 31-36.

6. Camp, J. P., T. Stokol, and M. L. Shuler, 2008, Fabrication of a multiple-diameter branched network of microvascular channels with semi-circular cross-sections using xenon difluoride etching: Biomedical Microdevices, v. 10, p. 179-186.

7. Chen, P. C., C. W. Pan, W. C. Lee, and K. M. Li, 2014, An experimental study of micromilling parameters to manufacture microchannels on a PMMA substrate: International Journal of Advanced Manufacturing Technology, v. 71, p. 1623-1630.

8. Choi, J. S., Y. Piao, and T. S. Seo, 2013, Fabrication of a circular PDMS microchannel for constructing a three-dimensional endothelial cell layer: Bioprocess and Biosystems Engineering, v. 36, p. 1871-1878.

9. Chung, B. G., K.-H. Lee, A. Khademhosseini, and S.-H. Lee, 2012, Microfluidic fabrication of microengineered hydrogels and their application in tissue engineering: Lab on a Chip, v. 12, p. 45-59.

10. D'Avino, G., G. Romeo, M. M. Villone, F. Greco, P. A. Netti, and P. L. Maffettone, 2012, Single line particle focusing induced by viscoelasticity of the suspending liquid: theory, experiments and simulations to design a micropipe flow-focuser: Lab on a Chip, v. 12, p. 1638-1645.

11. De Ville, M., P. Coquet, P. Brunet, and R. Boukherroub, 2012, Simple and low-cost fabrication of PDMS microfluidic round channels by surface-wetting parameters optimization: Microfluidics and Nanofluidics, v. 12, p. 953-961.

12. Dendukuri, D., S. S. Gu, D. C. Pregibon, T. A. Hatton, and P. S. Doyle, 2007, Stop-flow lithography in a microfluidic device: Lab on a Chip, v. 7, p. 818-828.

13. Dendukuri, D., D. C. Pregibon, J. Collins, T. A. Hatton, and P. S. Doyle, 2006, Continuous-flow lithography for high-throughput microparticle synthesis: Nature Materials, v. 5, p. 365-369.

14. Dornfeld, D., S. Min, and Y. Takeuchi, 2006, Recent advances in mechanical micromachining: Cirp Annals-Manufacturing Technology, v. 55, p. 745-768.

15. Faid, K., R. Voicu, M. Bani-Yaghoub, R. Tremblay, G. Mealing, C. Py, and R. Barjovanu, 2005, Rapid fabrication and chemical patterning of polymer microstructures and their applications as a platform for cell cultures: Biomedical Microdevices, v. 7, p. 179-184.

16. Farcas, M. A., L. Rouleau, R. Fraser, and R. L. Leask, 2009, The development of 3-D, in vitro, endothelial culture models for the study of coronary artery disease: Biomedical Engineering Online, v. 8.

17. Fiorini, G. S., and D. T. Chiu, 2005, Disposable microfluidic devices: fabrication, function, and application: Biotechniques, v. 38, p. 429-446.

18. Guarnieri, D., A. Falanga, O. Muscetti, R. Tarallo, S. Fusco, M. Galdiero, S. Galdiero, and P. A. Netti, 2013, Shuttle-Mediated Nanoparticle Delivery to the Blood-Brain Barrier: Small, v. 9, p. 853-862.

19. Guckenberger, D. J., T. E. de Groot, A. M. D. Wan, D. J. Beebe, and E. W. K. Young, 2015, Micromilling: a method for ultra-rapid prototyping of plastic microfluidic devices: Lab on a Chip, v. 15, p. 2364-2378.

20. Haeberle, S., and R. Zengerle, 2007, Microfluidic platforms for lab-on-a-chip applications: Lab on a Chip, v. 7, p. 1094-1110.

21. Hetsroni, G., A. Mosyak, E. Pogrebnyak, and L. P. Yarin, 2005, Fluid flow in micro-channels: International Journal of Heat and Mass Transfer, v. 48, p. 1982-1998.

22. Hochmuth, R. M., 2000, Micropipette aspiration of living cells: Journal of Biomechanics, v. 33, p. 15-22.

23. Huang, Z., X. Li, M. Martins-Green, and Y. Liu, 2012, Microfabrication of cylindrical microfluidic channel networks for microvascular research: Biomedical Microdevices, v. 14, p. 873-883.

24. Jang, M., Y. J. Kwon, and N. Y. Lee, 2015, Non-photolithographic plastic-mold-based fabrication of cylindrical and multi-tiered poly(dimethylsiloxane) microchannels for biomimetic lab-on-a-chip applications: Rsc Advances, v. 5, p. 100905-100911.

25. Kim, P., K. W. Kwon, M. C. Park, S. H. Lee, S. M. Kim, and K. Y. Suh, 2008, Soft lithography for microfluidics: a review: Biochip Journal, v. 2, p. 1-11.

26. Koschwanez, J. H., R. H. Carlson, and D. R. Meldrum, 2009, Thin PDMS Films Using Long Spin Times or Tert-Butyl Alcohol as a Solvent: Plos One, v. 4, p. 5.

27. Kreuter, J., 2001, Nanoparticulate systems for brain delivery of drugs: Advanced Drug Delivery Reviews, v. 47, p. 65-81.

28. Lee, J. S., 2000, 1998 distinguished lecture: Biomechanics of the microcirculation, an integrative and therapeutic perspective: Annals of Biomedical Engineering, v. 28, p. 1-13.

29. Lee, K., C. Kim, K. S. Shin, J. Lee, B.-K. Ju, T. S. Kim, S.-K. Lee, and J. Y. Kang, 2007, Fabrication of round channels using the surface tension of PDMS and its application to a 3D serpentine mixer: Journal of Micromechanics and Microengineering, v. 17, p. 1533-1541.

30. Mata, A., A. J. Fleischman, and S. Roy, 2005, Characterization of polydimethylsiloxane (PDMS) properties for biomedical micro/nanosystems: Biomedical Microdevices, v. 7, p. 281-293.

31. Miller, J. S., K. R. Stevens, M. T. Yang, B. M. Baker, D.-H. T. Nguyen, D. M. Cohen, E. Toro, A. A. Chen, P. A. Galie, X. Yu, R. Chaturvedi, S. N. Bhatia, and C. S. Chen, 2012, Rapid casting of patterned vascular networks for perfusable engineered three-dimensional tissues: Nature Materials, v. 11, p. 768-774.

32. Occhipinti, L. G., 2010, Surface treatment of an organic or inorganic substrate for enhancing stability of a lithographically defined deposited metal layer *in* F. Porro, ed., US Pat. App. 12/835,011

33. Ogilvie, I. R. G., V. J. Sieben, C. F. A. Floquet, R. Zmijan, M. C. Mowlem, and H. Morgan, 2010, Reduction of surface roughness for optical quality microfluidic devices in PMMA and COC: Journal of Micromechanics and Microengineering, v. 20.

34. Romeo, G., G. D'Avino, F. Greco, P. A. Netti, and P. L. Maffettone, 2013, Viscoelastic flow-focusing in microchannels: scaling properties of the particle radial distributions: Lab on a Chip, v. 13, p. 2802-2807.

35. Seo, J., C. Ionescu-Zanetti, J. Diamond, R. Lal, and L. P. Lee, 2004, Integrated multiple patch-clamp array chip via lateral cell trapping junctions: Applied Physics Letters, v. 84, p. 1973-1975.

36. Shih, T.-K., C.-F. Chen, J.-R. Ho, and F.-T. Chuang, 2006, Fabrication of PDMS (polydimethylsiloxane) microlens and diffuser using replica molding: Microelectronic Engineering, v. 83, p. 2499-2503.

37. Sia, S. K., and G. M. Whitesides, 2003, Microfluidic devices fabricated in poly(dimethylsiloxane) for biological studies: Electrophoresis, v. 24, p. 3563-3576.

38. Thangawng, A. L., R. S. Ruoff, M. A. Swartz, and M. R. Glucksberg, 2007, An ultra-thin PDMS membrane as a bio/micro-nano interface: fabrication and characterization: Biomedical Microdevices, v. 9, p. 587-595.

39. Valencia, P. M., O. C. Farokhzad, R. Karnik, and R. Langer, 2012, Microfluidic technologies for accelerating the clinical translation of nanoparticles: Nature Nanotechnology, v. 7, p. 623-629.

40. Whitesides, G. M., 2006, The origins and the future of microfluidics: Nature, v. 442, p. 368-373.

41. Whitesides, G. M., E. Ostuni, S. Takayama, X. Y. Jiang, and D. E. Ingber, 2001, Soft lithography in biology and biochemistry: Annual Review of Biomedical Engineering, v. 3, p. 335-373.

42. Wu, J., and M. Gu, 2011, Microfluidic sensing: state of the art fabrication and detection techniques: Journal of Biomedical Optics, v. 16.

43. Xia, Y. N., and G. M. Whitesides, 1998, Soft lithography: Angewandte Chemie-International Edition, v. 37, p. 550-575.

44. Zhang, W., D. S. Choi, Y. H. Nguyen, J. Chang, and L. Qin, 2013, Studying Cancer Stem Cell Dynamics on PDMS Surfaces for Microfluidics Device Design: Scientific Reports, v. 3.

45. Zhao, X. M., Y. N. Xia, and G. M. Whitesides, 1997, Soft lithographic methods for nano-fabrication: Journal of Materials Chemistry, v. 7, p. 1069-1074.

46. Ziolkowska, K., R. Kwapiszewski, and Z. Brzozka, 2011, Microfluidic devices as tools for mimicking the in vivo environment: New Journal of Chemistry, v. 35, p. 979-990.

5 CHAPTER 4

Effect of flow conditions on shuttle-mediated nanoparticle transport across the brain endothelium

5.1 ABSTRACT

In the last few years, several *in vitro* studies have been developed in order to address some of the fundamental mechanisms involved in BBB crossing by solutes, drugs and nanoparticles [1]. Indeed, except their comparatively high permeability and the loss of expression of some BBB efflux protein systems, in vitro models have several advantages over in vivo models, including low cost, high throughput screening and easiness to assess compounds and to investigate the transport mechanism at the molecular levels. Development of a rapid and reliable *in vitro* BBB model system is a challenge to reveal the drug delivery to the central nervous system (CNS). It is fundamental to test the efficacy on targeting and crossing of nanocarriers inside *in vitro* models which are able to mimic *in vivo* characteristics of the BBB. To this aim, a BBB microfluidic device was designed based on a transparent polyester porous membrane sandwiched between a top and a bottom overlying channel made of PMMA. Our data clearly indicate that this microfluidic system allows the growth of brain endothelial bEnd.3 cells and the formation of a confluent layer. Expression of the barrier properties was tested with trans-endothelial electrical resistance (TEER). By day 3 of cell culture TEER levels exceeded 100 Ω cm^2 reaching a plateau at day 7. Confocal images confirmed the expression of tight junctions. BBB monolayer regulates the selective transport of albumin and nanoparticles compared to blank porous filter. More interestingly, the decoration with gH625 peptide enhances the adhesion of nanoparticles at the endothelial layer and the BBB crossing at 5 µl/min flow rate, thus suggesting the efficacy of gH625 as a delivery platform to the brain. Here, we demonstrate for the first time the ability of a membranotropic peptide, namely gH625, to transport a cargo across the BBB layer under flow conditions [2].

5.2 INTRODUCTION

The blood-brain barrier (BBB), with its distinctive tissue structure, acts to separate the peripheral blood from the central nervous system (CNS), thereby maintaining brain homeostasis [3]. Among other things, the permeability of the BBB is controlled by the brain endothelial cells, that regulate the selective transport from the blood to the brain and vice versa [4]. The endothelial layer is also essential in preventing the entrance of toxic substances to the brain. Indeed, due to this tight barrier, the majority of drugs fail to cross the BBB. The BBB represents the main challenge for the development of new drug delivery systems, and many strategies are currently under development to improve the uptake of therapeutic compounds into brain parenchyma. Among other things, it has been recently demonstrated that the conjugation with the membranotropic peptide gH625 facilitates the delivery of nanoparticles across the BBB, leading to a significantly higher cell uptake and crossing, and, most importantly, to a reduction of NP intracellular accumulation as large aggregates in a static BBB model [5]. gH625 belongs to a class of hydrophobic peptides that efficiently traverse biological membranes promoting lipid membrane-reorganizing processes, such as fusion or pore formation, thus involving temporary membrane destabilization and subsequent reorganization [6]. These molecules are currently obtaining great attention since those may be exploited for drug delivery purposes [7,8]. In particular, the nineteen-residue peptide gH625 is a membrane-perturbing domain derived from the glycoprotein H (gH) of Herpes simplex virus 1; it interacts with model membranes, contributing to their merging and is able to traverse the membrane bilayer and transport a cargo into the cytoplasm and across the BBB *in vitro* [9,10]. Nowadays, most of BBB experiments are performed in static Transwell assays [11–13]. However, *in vivo* brain endothelial cells are subjected to the blood flow that lacks in the commonly used *in vitro* models. In this context, *in vivo* models are the best candidates to study the transport across the BBB. However, these resources are scarce, expensive and difficult to study both in detail and real-time. *Ex vivo* and *in vitro* models are good alternatives, as they are credited for their simplicity and controlled environment [4]. Moreover, shear stress derived from blood flow positively affects endothelial cell physiology and tight junction formation [14]. Till now, there are only few papers published of a dynamic BBB model [15–18]. Recently, the use of micro-technologies to study organ physiology has received rapidly growing attention (Huh et al. 2011). These organs-on-chips have the potential to be used as human-relevant disease models, and additionally provide detailed insight into drug effects [14,19]. Two microfluidic models of the BBB have recently been reported, demonstrating the feasibility of an organ-on-chip approach [15,16]. The aim of this work has been to test the ability of gH625 peptide to transport nanoparticles across the

brain endothelium under flow conditions. To mimic the blood flow in brain capillaries, we designed an *in vitro* µ-fluidic BBB model. The system was realized in such a way as to permit the growth of the cells on a porous filter up to reaching the confluence and to separate two compartments delimited by endothelial layer, namely the blood side and the brain side. The microfluidic chip (Fig. 1) contains a transparent polyester microporous membrane (Corning Costar, Cambridge, MA,USA) sandwiched between a top and a bottom overlying channel. The endothelial layer is obtained on the porous membrane directly into the device after culturing mouse brain endothelial cells. A collecting chamber is also integrated on the top channel in order to collect traversed NPs. To verify our issue, we first characterize the growth and the formation of a confluent brain endothelial layer of bEnd.3 cells within the *in vitro* µ-fluidic system through bright-field and confocal microscopy observations. Then, the permeability of this system was tested by using fluorescent albumin (BSA) as a standard molecule and amine-modified fluorescent polystyrene nanoparticles as a control indicating the functionality of our model. Finally, the capability of gH625-conjugated nanoparticles to adhere to and cross the brain endothelial layer under flow conditions were investigated.

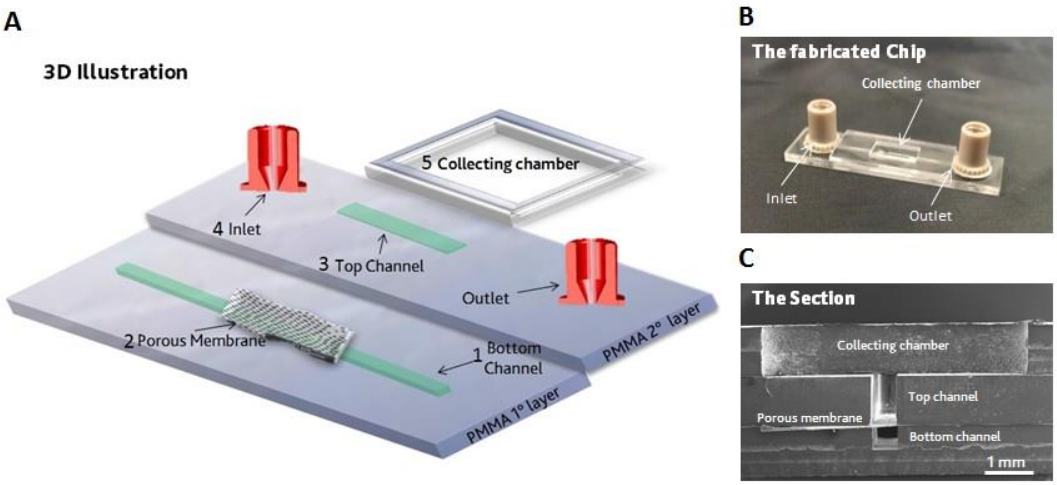

Figure 1. Scheme of the developed BBB microfluidic system (A), including (1) the bottom channel, (2) polyester membrane, (3) the top channel, (4) the Nanoport UPCHURCH® connectors and (5) collecting chamber. Picture of the fabricated chip (B) and SEM image of a section of the device (C).

5.3 RESULTS AND DISCUSSION

5.3.1 *In vitro* BBB model characterization

The microfluidic device was tested before cell seeding in terms of sealing. It was also morphologically characterized by SEM in order to confirm the right alignment and dimensions of the channels (Fig. 1 C).

bEnd.3 cells were seeded in the channel and allowed to adhere to the membrane for 24 h at 37 °C. Afterward, the system has been turned upside down, the channel was rinsed with fresh medium to remove non-adhered cells and incubated at 37 °C for 1, 3 and 7 days of culture. Fig. 2 shows phase contrast images of bEnd.3 cell layer after different days of growth in the microfluidic device.

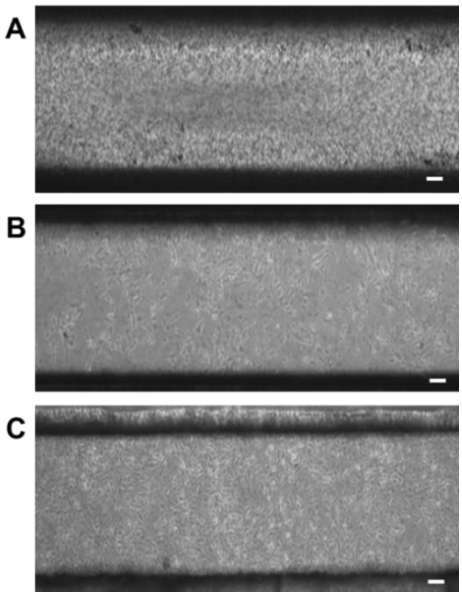

Figure 2. Phase contrast microscopy pictures of endothelial cell layer in the microfluidic system channel after 1 (A), 3 (B) and 7 (C) days from cell seeding. Bar 100 µm.

As reported, cell confluency increased over time. After 7 days post cell seeding, the cells formed a confluent monolayer as demonstrated by the nuclei and microfilament fluorescent staining (Figs. 3 A-C). Image analyses confirmed that the cell density per area increased over time (Fig. 3 G). To verify the formation of tight junctions, indirect immunofluorescence against Claudin 5 protein was performed at the 7^{th} day of culture. Confocal microscopy images show that bEnd.3 cells were able to express Claudin 5 protein, prevalently localized around the cell boundaries thus indicating the formation of tight junctions (Fig. 3 H). These data demonstrate the capability of the microfluidic device to allow the growth and the correct formation of the confluent brain endothelial layer.

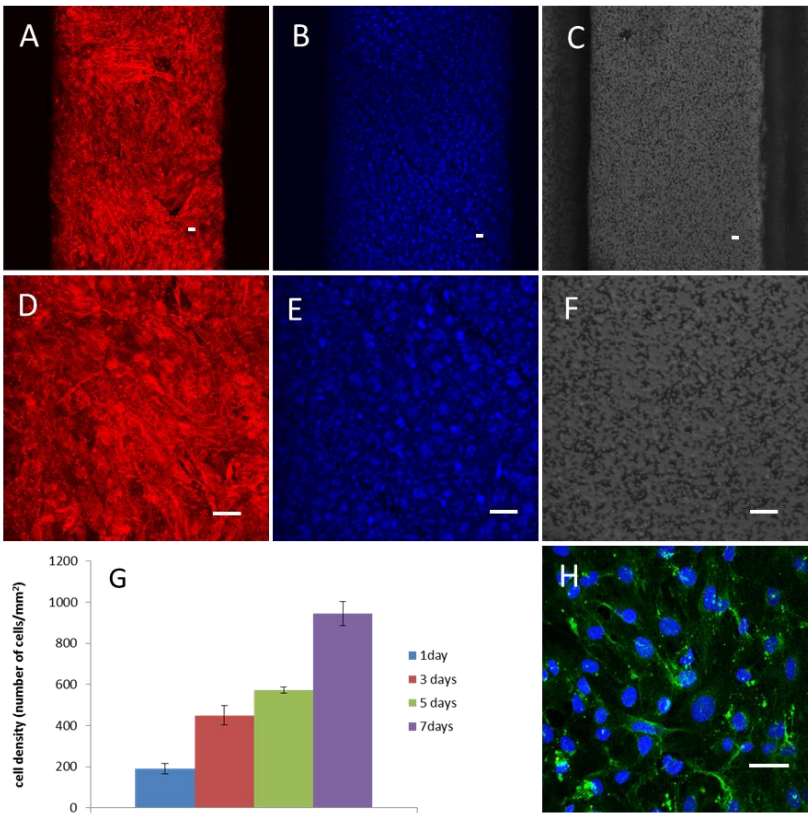

Figure 3. 7-day growth confluent bEnd.3 cell layer. (A, D) Phalloidin (red) staining of cytoskeleton; (B, E) DAPI (blue) staining of nuclei; (C, F) bright-field images of the polyester filter. (A-C) Images acquisition performed with a 10 × dry objective. (D-F) Zoomed images shown in panels (A-C). (G) Cell density over culture time. (H) Claudin 5 (green) and DAPI (blue) staining of tight junctions and nuclei, respectively, acquired with a 25 × water-immersion objective. Bar 50 µm.

5.3.2 TEER measurement

TEER was measured every day after seeding in order to monitor cell confluence and the development of tight junctions. TEER results indicated high [16] resistance value for BBB microfluidic model (Fig. 4). Our cultures reached the steady-state by day 5-7. TEER level remains of 110 Ω cm^2 at day 7 of culture, according with the Claudin-5 imaging data. Therefore day 7 was chosen as endpoint threshold for transport assays.

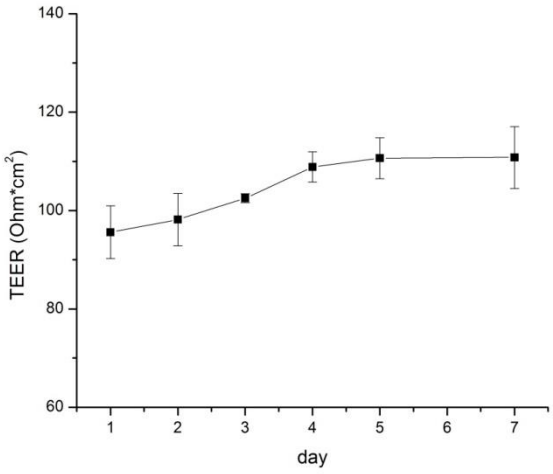

Figure 4: TEER measurements over culture time.

5.3.3 BSA transport across the BBB

In order to assess the integrity of the cellular monolayer, we performed transcytosis experiments to test the capability of BSA to cross the endothelial layer. BSA is known to cross the BBB through adsorptive transcytosis, therefore it can be used as a valid standard to measure the system functionality under flow conditions [20,21]. BSA transport experiments were performed after 7 days of cell culture under static conditions. The device was connected to a syringe pump and the cells were subjected to a flow rate of 5 µl/min which follows in the typical range of flow rates reported in literature [22,23]. Fig. 4 shows the mass of

the transported BSA across the microfluidic system at regular time points. In absence of the cells, almost 100 % of BSA was transported after 3h. Conversely, in the presence of the confluent cell layer, there was a significant decrease in the BSA permeation, with about 16 % of transported BSA after 3 h under flow conditions.

.

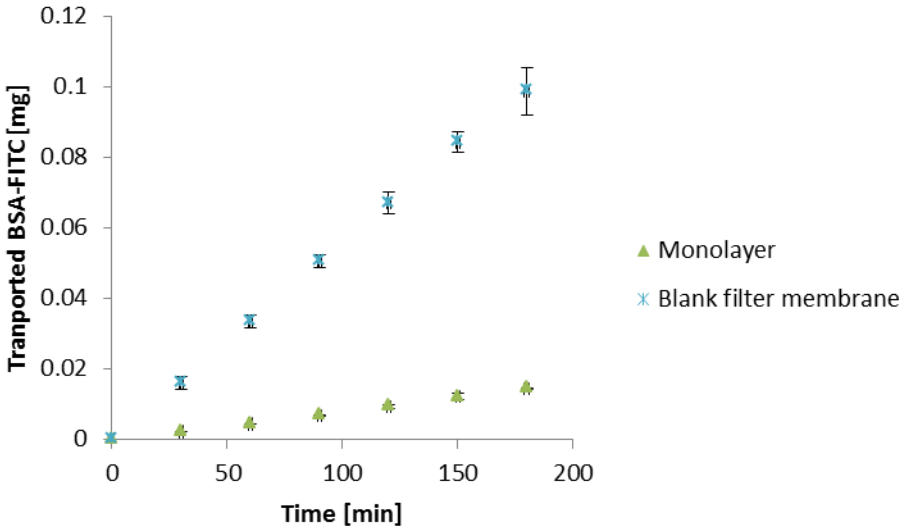

Figure 4. Mass of transported BSA under flow conditions, flow rate: 5 µl/min in absence and in presence of the confluent cell layer

5.3.4 Nanoparticle transport across the BBB in the microfluidic system

In order to validate the BBB microfluidic device for nanoparticle transport studies, NP transcytosis experiments have been performed, both in presence and in absence of the confluent cell layer at two different flow rates (5 and 25 µl/min) for 3h. Experiments were carried out by diluting NPs at a concentration of 9.20×10^{10} NP/ml in buffered cell culture medium. As shown in Fig. 6, in presence of the blank filter membrane the percentage of the transported NPs through the BBB monolayer at 5 µl/min was about 7 times higher than the transported NPs at 25 µl/min. More precisely, it was 13.45 % at 5 µl/min and 1.96 % at 25 µl/min. In presence of the confluent cell layer, the trend was inverted and the percentage of transported NPs decreased. In particular, the percentage of transported NPs at 5 µl/min was 2.72 % against 7.33 % found at 25 µl/min.

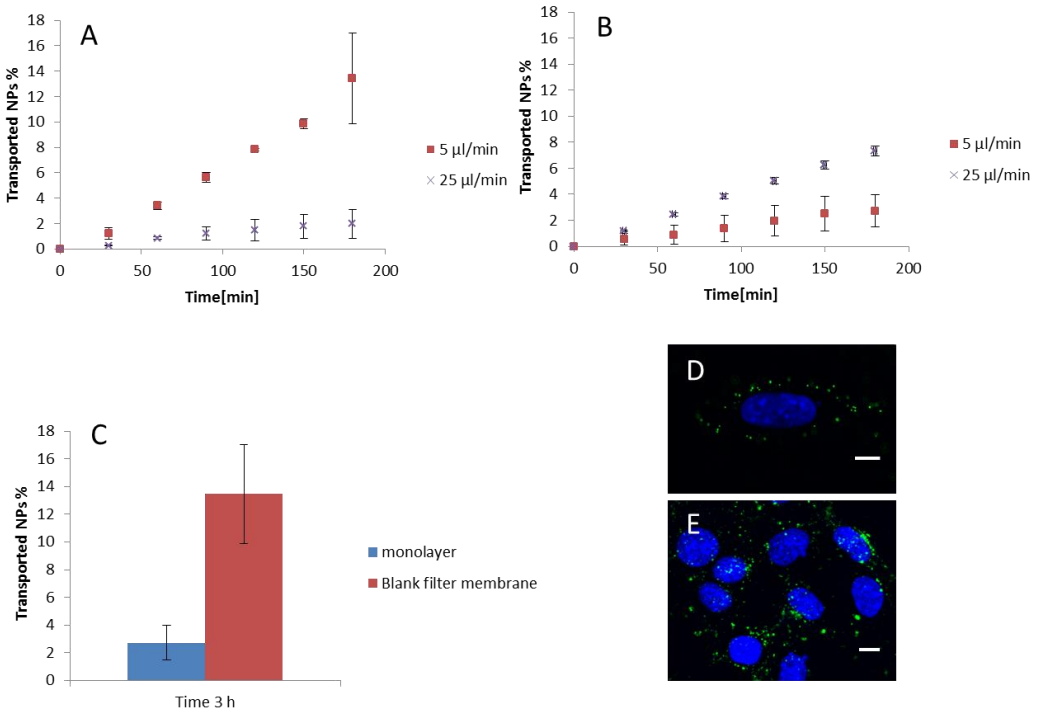

Figure 6. Percentages of transported blank NPs under flow conditions in absence (A) and in presence (B) of the confluent cell layer. Data are reported at two different flow rates, 5 and 25 µl/min. Percentages of transported blank NPs under flow conditions (Flow rate: 5 µl/min), in absence and in presence of the confluent cell layer (C). D and E represent confocal images of blank NPs in bEnd.3 cells after 3 hours of experiment in flow condition. Green: blank NPs; blue: nuclei. Bar: 10 µm.

We hypothesized that these results could depend on a breakage of the endothelial layer as a result of the combination of high flow rate and high NP concentration. Therefore, in order to understand the effect of the NP concentration on the integrity of the cell monolayer, we performed the transcytosis experiment at the higher flow rate (25 µl/min), by using a NP suspension at a concentration - 1.84 x 10^{10} NP/ml - 5 times lower than the previous experiments. Results shown in Fig. 7A indicate that after 3h under flow conditions, the percentage of transported NPs was 9.90 % with the filter alone, decreasing to 3.44 % in presence of the layer. In these conditions, we obtained results quite similar to those obtained at a fivefold lower flow rate (5 µl/min) with a fivefold higher NP concentration (9.20 × 10^{10} NP/ml). In fact we obtained 4.84 % of transported NPs at 25 µl/min by using NP concentration of 1.84 x 10^{10} NP/ml and 2.72 % at 5 µl/min by using 9.20 × 10^{10} NP/ml, in presence of the monolayer (Fig. 7B).

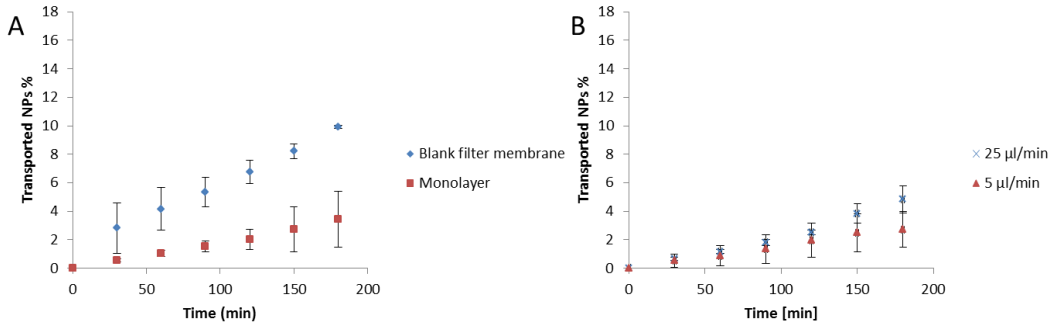

Figure 7. Percentages of transported blank NPs under flow rate of 25 µl/min at a final concentration of 1.84×10^{10} NP/ml (A). Data are reported in absence and in presence of the confluent cell layer. Blank NPs under flow rates of 5 and 25 µl/min, at final concentrations of 9.20×10^{10} and 1.84×10^{10} NP/ml, respectively, in presence of the monolayer (B).

Taken altogether these findings indicate that: i) the presence of the layer hinders the passage of solutes and nanoparticles across the filter; ii) the integrity of the cell layer depends on a right combination between the concentration of the nanoparticles and the flow rate.

5.3.5 Effect of the functionalization with gH625 peptide on nanoparticle transport across the BBB in the microfluidic system

Several works reported that NPs enter the cells using a cell-mediated mechanism, called endocytosis. After endocytosis, endosomes can deliver their cargo across the cell by transcytosis processes. Alternatively, these vesicles can also be sent to the lysosomes for degradation. It was previously demonstrated that gH625 is able to transport different cargos such as liposomes and quantum dots across cells [10,24,25]**.** In a previous work, the surface of fluorescent aminated polystyrene NPs has been functionalized with gH625 and transport across static *in vitro* BBB models has been investigated. Results demonstrated that gH625 NPs translocate efficiently across cell membranes and cell internalization does not seem to exclusively involve classical endocytosis mechanisms. In fact, conjugation with gH625 facilitates the delivery of nanoparticles across the BBB, leading to significant higher cell uptake and crossing, decreasing lysosomal accumulation [5]. Based on the previous observations, we tested the capability of gH625 to enhance NP transport across the BBB layer in flow conditions, using 5 µl/min flow rate and a NP concentration of 9.20×10^{10}

NP/ml. Fig. 8 A shows the comparison of the transported blank and gH625-NPs. As reported, gH625 increases about two fold the transport of NPs through the BBB, becoming 6.13 % compared to 2.72 % of non-functionalized NPs. Looking at the cell layer, we observed the adhesion of blank and gH625-nanoparticles after the flow experiments (Figs. 8 B-E). Data of image fluorescent analysis show an increment of about two fold of adhered gH625-NPs compared to blank NPs (Fig. 8 F) thus indicating an affinity of functionalized nanoparticles to the cell membrane higher than the blank ones in dynamic conditions. Actually, gH625 peptide shows a particular tropism for cell membrane cholesterol [26]. It is likely that this property may promote the interaction of gH625 functionalized nanoparticles with the cells and, as a consequence, their adhesion on the cell membrane also in flow conditions.

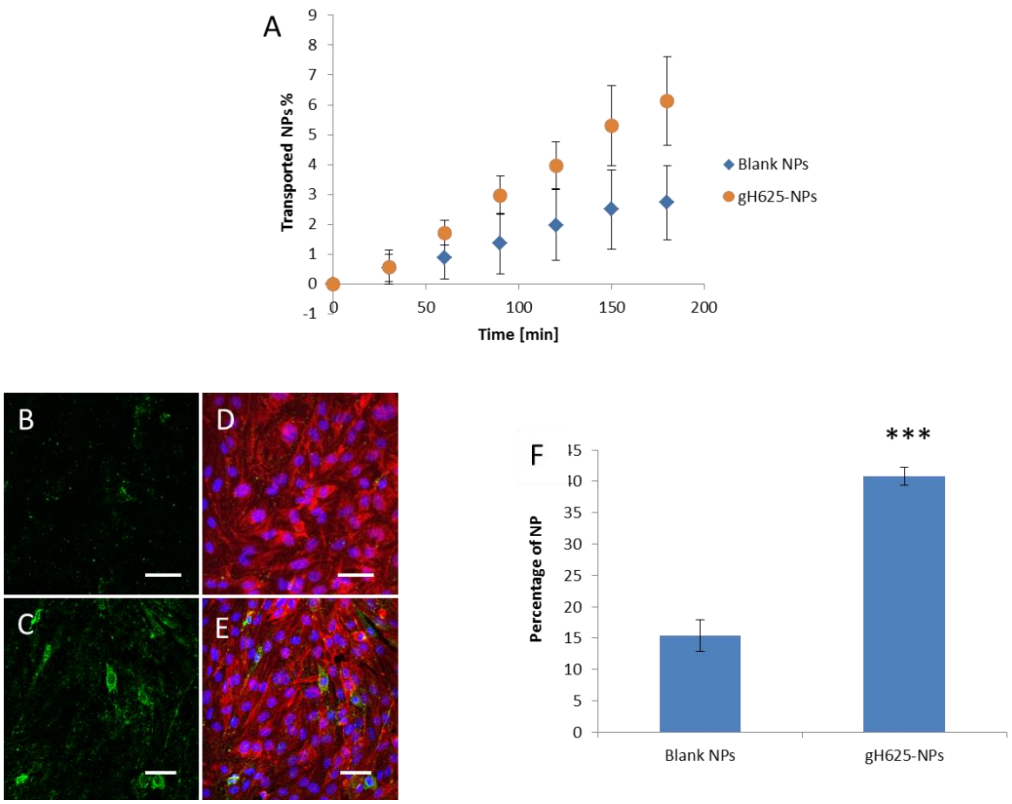

Figure 8. Blank and gH625-NPs (A) transported under dynamic conditions (Flow rate: 5 µl/min). Confocal images of the confluent cell layer in the µ-fluidic system after the experiment: green fluorescent represents blank NPs (B) and gH625-NPs (C). D and E are merge images of red Phalloidin and blue nuclei with blank NPs and gH625-NPs, respectively. Percentages of blank and gH625-NPs per image area (F). The data are reported as the mean ± SD (n = 5), *** $P < 0.0001$. Bar 50 µm.

5.4 MATERIALS AND METHODS

5.4.1 Microfluidic system design and fabrication

In this section, we detail the design and fabrication of the microfluidic chip. It is based on different PMMA layers bonded via solvent evaporation. Specifically, the assembly of the PMMA layers was performed by simply immersing PMMA substrates in ethanol for 10 min. The immersed substrates were immediately removed, aligned and clamped for an overlap of the top and bottom channel, after the heat treatment was initiated at 58 °C for 45 minutes. Before proceeding with the assembly of the chip the manufacturing substrates were cleaned using a common soap (RBS Ditalclean, Brussels). The bonding between the top and the bottom channel substrates allows to enclose the polyester membrane on which cells are grown afterwards. PMMA is a transparent thermoplastic polymer that can be easily micro-machined by micromilling (Minitech Machinery Corporation) which is a fast prototype technique. (P. C. Chen, C. W. Pan, W. C. Lee and K. M. Li, *International Journal of Advanced Manufacturing Technology*, 2014, 71, 1623-1630). In addition to bond NanoPorts Upchurch® to PMMA microdevices, we developed a hybrid system, which glues commercial nano-ports with an alternative biocompatible epoxy adhesive. The microfluidic chip shown in Fig. 1 is composed of two PMMA channel substrates (12 x 50 x 1 mm) and a PMMA collecting chamber (12 x 30 x 1 mm). The depth and width of the channel is different onto the two PMMA substrates, 889 µm width and depth for the bottom channel and 1.2 mm of depth and 889 µm of width for the top channel. The microtool used to micromachine the PMMA was in all the cases a flute endmill with a 889 µm in diameter. In the second PMMA layer we microfabricated inlet and outlet holes to connect microfluidics chip with classic fluidic equipment such as syringe pump and tubing. The fabrication process consists of 4 steps: (1) preparation of the chip draft using Draftsight (Cad Software), (2) micromachining of PMMA layers; (3) ethanol-assisted bonding process and (4) bonding Nanoport Upchurch to PMMA substrate. The certified positioning accuracy of the three-axis are 12”/300 mm in x-axis, 9”/228 mm in y-axis, and 9”/228 mm in z-axis. To standardize the fabrication process, the PMMA substrates used in this study were purchased from the same batch of the polymer supplier (GoodFellow Cambridge Limited, England).

5.4.2 Cell culture

Mouse cerebral endothelial bEnd.3 cells (American Type Culture Collection, Manassas, VA) were grown in DMEM with 4.5 g/L glucose, 10% Foetal Bovine Serum (FBS), 3.7 g/L sodium bicarbonate, and 4 mM glutamine, 1% non-essential amino acids, 100 U/ml penicillin and 0.1 mg/ml streptomycin in 100 mm diameter cell culture dish, in a humidified atmosphere at 37 °C and 5% CO_2. Cells used in all experiments were at passage 11–18.

5.4.3 Fluorescent solutes and nanoparticles

Fluorescein isothiocyanate conjugated bovine serum albumin (FITC-BSA, MW 66 kDa) and orange fluorescent amine-modified polystyrene, 100 nm, nanoparticles (NPs) were purchased by Sigma-Aldrich.

5.4.4 gH625 peptide synthesis and conjugation to polystyrene nanoparticles

gH625 peptide (Ac-HGLASTLTRWAHYNALIRAFGGG-COOH) was synthesized using the standard solid-phase-9-fluorenylmethoxycarbonyl (Fmoc) method as previously reported [17] and obtained with good yields (30 - 40 %). The conjugation of gH625 to amine-modified fluorescent polystyrene nanoparticles was performed as described previously [21]. Briefly, the peptide was preactivated with EDC (1-Ethyl-3(3-dimethylamino-propyl)-carbodiimide, hydrochloride) and NHS (N-Hydroxysuccinimide) in molar ratio of 4:4:1 in PBS buffer at pH 7.4, at room temperature (RT) under stirring for 30 min. NPs were conjugated with the preactivated-peptide, in MES 0.1 M buffer at pH 5.5 for 3 h at RT in presence of Tween 20 and the yield of the reaction was higher than 90 %. The peptide-NPs were purified from the unconjugated-NPs by exclusion chromatography on a 1 × 18 cm Sephadex G-50 (Amersham Biosciences) column. The fluorescence spectra of peptide-NPs and unconjugated NPs were measured in a Cary Eclipse Varian fluorescence spectrophotometer.

5.4.5 Cell seeding and culture in the microfluidic system

The fabricated chip was previously sterilized with 10 % Penicillin-Streptomycin solution for 24 h at 4 °C to prevent contamination. bEnd.3 cells were seeded at a density of 25×10^3 cells/cm^2 into microfluidic channel and the system was turned upside down, in order to allow cell adhesion to the polyester filter located on the top of the channel. Non-adhered cells were removed 24 h after seeding by twice washing with fresh cell culture medium. Afterward, cells were allowed to grow until 7 days within the device. Medium was refreshed every 3 days. Cell growth was monitored over time by phase contrast and confocal microscopy at 1, 3, 5 and 7 days of culture. In order to further verify cell growth in the microfluidic system, bEnd.3 were fixed within system with 4 % paraformaldehyde for 10 min at RT and stained with 4, 6-diamidino-2-phenylindole (DAPI, Sigma), hence, the number of nuclei was counted by imageJ software 1.44p.

5.4.6 Cell staining

The presence of tight junctions was determined by immune-staining with anti-Claudin 5 antibody (Life Technologies). Briefly, bEnd.3 cells were fixed with 4% paraformaldehyde for 10 minutes. After permeabilization with 0.1 % Triton-X100, cells were incubated with the blocking buffer (BB) (0.5% BSA in PBS) and were stained with the anti-Claudin 5 primary antibody for 1h at RT. Then, the Alexa-488 anti-Mouse secondary antibody diluted in BB was incubated 1h at RT. In order to detect actin filaments, TRITC-Phalloidin (Sigma) was used. After fixation and permeabilization, bEnd.3 cells were incubated for 30 minutes at RT. For nuclei staining DAPI was used. All samples were then observed at confocal microscope (Leica TCS SP5 MP) with a 25 × water-immersion objective.

5.4.7 TEER measurements

TEER measurements were carried out by connecting the BBB chip to an AUTOLAB PGSTAT302N (potentiostat/galvanostat) equipped with a FRA32M module (frequency response analysis module). Impedance spectra were recorded in potentiostatic mode with an amplitude of 0.01V and frequencies ranging from 100kHz to 0.1Hz between two Pt electrodes. Pt electrodes were realized by sputtering deposition of 20 nm of platinum on the surface of metallic microfluidic tips with a final diameter of 1.3 mm. For each

measurement 3 readings and 50 data points (logarithmic frequency step) per reading were collected. The least-square optimization method was used to fit the measured impedance data to an electrical equivalent circuit model, reported in Fig. 9.

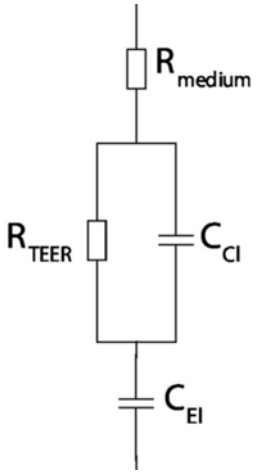

In the adopted model the constant phase element represents the dual layer capacitance of Pt electrodes (CPEdl), which is in series with the resistance of the medium (Rmedium) and the cell monolayer, which is denoted as the resistance of cell (Rteer) and the capacitance of the cell membrane (Ccl) in parallel. Porous polymeric membrane was used as supporting material for cells adhesion and growing. This membrane represents an additional resistive term (Rmem) which is in parallel with Rteer. Thus, for each impedance spectra an apparent Rteer (Req) was collected and then corrected (eq. 1) for the membrane resistance to obtain the effective Rteer.

Rteer=(Req*Rmem)/(Req+Rmem)

Rteer was normalized for the cross sectional surface area of the chip (0.054 cm2) to calculate TEER value in Ohm*cm2.

5.4.8 Transport assay

Transport experiments across the BBB microfluidic system were performed at the 7th day after seeding. Briefly, a 5 ml syringe was loaded with a FITC-BSA solution at the final concentration of 0.1 mg/ml in cell culture medium supplemented with 40 mM HEPES buffer. For nanoparticle transport experiments, the syringe was loaded with blank and gH625-NP suspensions in buffered cell culture medium at the final concentration of 9.20×10^{10} and 1.84×10^{10} NP/ml. The syringe was then allocated on a syringe pump (Harvard Apparatus Pump 11 Elite) connected to the inlet of the microfluidic system by a tube (Radel Tubing 1/16x020xsoft). The outlet of the system was connected to an Eppendorf tube through the same kind of tube in order to collect the output flow media. The collection chamber was filled with 90 µl of cell culture medium. The experiments were carried out in a plexiglass incubator at 37 °C and solutions are flowed at 5 or 25 µl/min flow rates. Compounds and NPs that cross the endothelial monolayer are collected in the apical chamber. Experiments were carried out for 3 h, drawing the medium in the collection chamber every 30 minutes and replacing it with fresh medium. The transport of BSA and nanoparticles across the BBB layer was estimated by fluorescence measurements through a spectrofluorometer (Perkin-Elmer, USA). Data were reported as the percentage of transported BSA and NPs compared to the initial concentrations of the fluorescent compounds.

5.4.9 Image analysis

In order to quantify the amount of NPs in the cells, after NP transport experiment under flow conditions, bEnd.3 cells were fixed in the microfluidic system and stained with DAPI. Five images for each sample were acquired by confocal microscope and analyzed. The quantification of fluorescent NPs was performed by using area calculator plugins of ImageJ software. Data were reported as fluorescent areas normalized to the number of the cell nuclei.

5.4.10 Statistical analysis

Results were expressed as mean ± standard deviation (SD). Results repeats were compared by a one-way analysis of variance (ANOVA), and a p value < 0.05 was considered statistically significant.

5.5 CONCLUSIONS

The goal of this work has been to set up a BBB microfluidic system which is able to investigate the effects of the flow on bioconjugated nanoparticles surface. The microfluidic system made of PMMA, has an high degree of biocompatibility with biological tissue. Furthermore, transparency of the PMMA allows to monitor the growth of cerebral endothelial layer. A protocol of cell seeding and culture in the system has been developed and cells are able to grow, reach the confluency and express the tight junctions up to 7 days from the seeding. These data were confirmed by phase contrast and confocal images of endothelial cell layer in the system channel and TEER results suggest that the *in vitro* BBB reproduces the key physiological and biological characteristics of a BBB model. Nanoparticles are able to cross the porous filter in the microfluidic system and the presence of cell monolayer reduce NP transport which depends on flow rate and NP concentration. In order to evaluate the effects of flow conditions on crossing of the CPP gH625 in transporting NP across the BBB, firstly, 5 µl/min has been selected as working flow rate because it does not affect the cell monolayer integrity. The interactions between gH-NPs and *in vitro* brain endothelium, to predict the rate of NP delivery across the BBB, has been evaluated to understand mechanisms of barrier transport, under dynamic condition. Reported here is that the conjugation of gH625 on the surface of polystyrene NPs facilitated the delivery of nanoparticles across the BBB, leading to significant higher cell uptake and crossing under flow condition, by using a microfluidic system. Taken all together these data suggest that *in vitro* BBB microfluidic system could represent a promising platform for NP transport assays. The home-made device is able to investigate the effects of dynamic conditions on specific targeting and transport across the brain endothelium of active peptides conjugated to nanocarriers. The system allows reproducibility of experiments and allows the quantification of transport of molecules and nanoparticles across the BBB *in vitro*. More interestingly, gH-NPs could be regarded as a promising strategy to design delivery systems for administration of therapeutical compounds to the brain, deserving further investigations to more precisely characterize the mechanism by which gH625 crosses the BBB and to address the cell specificity issue by linking to the nanosystem also molecules specifically recognized by the brain endothelium.

5.6 REFERENCES

1. Ragnaill, M. N. *et al.* Internal benchmarking of a human blood-brain barrier cell model for screening of nanoparticle uptake and transcytosis. *Eur. J. Pharm. Biopharm.* **77,** 360–367 (2011).

2. Guarnieri D., **Falanga A.P**. et al. *(to be submitted)*

3. Paolinelli, R., Corada, M., Orsenigo, F. & Dejana, E. The molecular basis of the blood brain barrier differentiation and maintenance. Is it still a mystery? *Pharmacol. Res.* **63,** 165–171 (2011).

4. Cardoso, F. L., Brites, D. & Brito, M. A. Looking at the blood–brain barrier: Molecular anatomy and possible investigation approaches. *Brain Res. Rev.* **64,** 328–363 (2010).

5. Guarnieri, D. *et al.* Shuttle-Mediated Nanoparticle Delivery to the Blood-Brain Barrier. *Small* **9,** 853–862 (2013).

6. Galdiero, S. *et al.* Intracellular delivery: exploiting viral membranotropic peptides. *Curr. Drug Metab.* **13,** 93–104 (2012).

7. Vitiello, G. *et al.* Lipid composition modulates the interaction of peptides deriving from herpes simplex virus type I glycoproteins B and H with biomembranes. *Biochim. Biophys. Acta-Biomembranes* **1808,** 2517–2526 (2011).

8. Galdiero, S. *et al.* Peptides containing membrane-interacting motifs inhibit herpes simplex virus type 1 infectivity. *Peptides* **29,** 1461–1471 (2008).

9. Falanga, A. *et al.* A peptide derived from herpes simplex virus type 1 glycoprotein H: membrane translocation and applications to the delivery of quantum dots. *Nanomedicine* **7,** 925–34 (2011).

10. Carberry, T. P. *et al.* Dendrimer functionalization with a membrane-interacting domain of herpes simplex virus type 1: Towards intracellular delivery. *Chem. - A Eur. J.* **18,** 13678–13685 (2012).

11. Avdeef, A. How well can in vitro brain microcapillary endothelial cell models predict rodent in vivo blood–brain barrier permeability? *Eur. J. Pharm. Sci.* **43,**

109–124 (2011).

12. Hatherell, K., Couraud, P. O., Romero, I. a., Weksler, B. & Pilkington, G. J. Development of a three-dimensional, all-human in vitro model of the blood-brain barrier using mono-, co-, and tri-cultivation Transwell models. *J. Neurosci. Methods* **199,** 223–229 (2011).

13. Patabendige, A., Skinner, R. a. & Abbott, N. J. Establishment of a simplified in vitro porcine blood-brain barrier model with high transendothelial electrical resistance. *Brain Res.* **1521,** 1–15 (2013).

14. van der Meer, A. D., Poot, A. A., Feijen, J. & Vermes, I. Analyzing shear stress-induced alignment of actin filaments in endothelial cells with a microfluidic assay. *Biomicrofluidics* **4,** 011103 (2010).

15. Yeon, J. H. *et al.* Reliable permeability assay system in a microfluidic device mimicking cerebral vasculatures. *Biomed. Microdevices* **14,** 1141–1148 (2012).

16. Booth, R. & Kim, H. Characterization of a microfluidic in vitro model of the blood-brain barrier (μBBB). *Lab Chip* **12,** 1784 (2012).

17. Cucullo, L. *et al.* Immortalized human brain endothelial cells and flow-based vascular modeling: a marriage of convenience for rational neurovascular studies. *J. Cereb. Blood Flow & Metab.* **28,** 312–328 (2008).

18. Neuhaus, W. *et al.* A novel flow based hollow-fiber blood-brain barrier in vitro model with immortalised cell line PBMEC/C1-2. *J. Biotechnol.* **125,** 127–141 (2006).

19. Huh, D., Hamilton, G. A., Ingber, D. E. & Program, B. HHS Public Access. **21,** 745–754 (2015).

20. Shao, J. *et al.* A microfluidic chip for permeability assays of endothelial monolayer. *Biomed. Microdevices* **12,** 81–88 (2010).

21. Walter, F. R. *et al.* A versatile lab-on-a-chip tool for modeling biological barriers. *Sensors Actuators B Chem.* **222,** 1209–1219 (2016).

22. Prabhakarpandian, B. *et al.* SyM-BBB: a microfluidic blood brain barrier model. *Lab Chip* **13,** 1093 (2013).

23. Booth, R. & Kim, H. Permeability Analysis of Neuroactive Drugs Through a Dynamic Microfluidic In Vitro Blood–Brain Barrier Model. *Ann. Biomed. Eng.* **42,** 2379–2391 (2014).

24. Falanga, A., Galdiero, M. & Galdiero, S. Membranotropic Cell Penetrating Peptides: The Outstanding Journey. *Int. J. Mol. Sci.* **16,** 25323–25337 (2015).

25. Tarallo, R. *et al.* Clickable functionalization of liposomes with the gH625 peptide from Herpes simplex virus type I for intracellular drug delivery. *Chemistry* **17,** 12659–68 (2011).

26. Guarnieri, D. *et al.* Surface decoration with gH625-membranotropic peptides as a method to escape the endo-lysosomal compartment and reduce nanoparticle toxicity. *Nanotechnology* **26,** 415101 (2015).

6 CONCLUSIONS

The applications of nanoparticles for drug delivery demonstrated to have a significant impact in particular on area of medicine for brain treatments. Nevertheless, drugs delivered inappropriately can produce side effects to healthy tissues and can hamper reaching the threshold dose to be effective in the target sites. In order to overcome these limits, a precise control of nanoparticles on BBB targeting and crossing is needful. In this context, this thesis deals with the importance of defining the optimal physico-chemical properties for a rational design in order to obtain a more specific BBB targeting and transport of nanoparticles. Biodegradable nanoparticles made up of PELGA polymers functionalized with CRT and gH625 peptides able to recognize the TfRs over-expressed on cerebral endothelium and to transport nanoparticles across the BBB have been developed and characterized. Results confirmed the effectiveness of both CRT and gH625 peptides in transporting nanoparticle across the BBB, specifically, in a synergistic manner. For a better understanding of NP behavior, a microfluidic BBB model system that mimics blood flow has been developed. Through permeability assays the system can be used to predict the rate of delivery of new NPs across the BBB. Experiments demonstrated the versatile potential of this microfluidic platform. Thus, the use of the fabricated microfluidic BBB model could be a valid option for pre-clinical studies.

Collectively, the data obtained also indicate that further investigation of the dual-functionalized NP permeability across the microfluidic BBB model is necessary in order to predict the rate of NP delivery through the cerebral endothelium under dynamic conditions. The produced NPs hold promise as a useful tool to improve therapeutic efficacy for treatment of brain diseases.